

SILVER ENDOTAXIAL NANOSTRUCTURES IN Si AND THEIR *SERS* APPLICATIONS

By

Raghavendra Rao Juluri

INSTITUTE OF PHYSICS

BHUBANESWAR, INDIA

A THESIS SUBMITTED TO THE
BOARD OF STUDIES IN PHYSICAL SCIENCE DISCIPLINE

IN PARTIAL FULLFILLMENT OF REQUIREMENTS

FOR THE DEGREE OF

DOCTOR OF PHILOSOPHY

OF

HOMI BHABA NATIONAL INSTITUTE



October, 2014

Statement By Author

This dissertation has been submitted in partial fulfillment of requirements for an advanced degree at Homi Bhabha Nation Institute (HBNI) and is deposited in the Library to be made available to borrowers under rules of the HBNI. Brief quotations from this dissertation are allowable without special permission, provided that accurate acknowledgement of source is made. Requests for permission for extended quotation from or reproduction of this manuscript in whole or in part may be granted by the Competent Authority of HBNI when in his or her judgment the proposed use of the material is in the interests of scholarship. In all other instances, however, permission must be obtained from the author.

Raghavendra Rao Juluri

Institute of Physics

Bhubaneswar

Declaration

I, Raghavendra Rao Juluri, hereby declare that the investigations presented in the thesis have been carried out by me. The matter embodied in the thesis is original and has not been submitted earlier as a whole or in part for a degree/diploma at this or any other University/Institution.

Raghavendra Rao Juluri

Institute of Physics

Bhubaneswar

Certificate

This is to certify that the thesis entitled "**Silver Endotaxial Nanostructures in Silicon and Their SERS Applications**", which is being submitted by **Mr. Raghavendra Rao Juluri** in partial fulfillment of the degree of **Doctor of Philosophy in Physics** of **Homi Bhabha National Institute** is a record of his own research work carried out by him. He has carried out his investigations for the last five years on the subject matter of the thesis under my supervision at **Institute of Physics, Bhubaneswar**. To the best of our knowledge, the matter embodied in the thesis has not been submitted for the award of any other degree.

Signature of the candidate:

Raghavendra Rao Juluri

Institute of Physics

Bhubaneswar

Signature of the supervisor:

Dr. P. V. Satyam

Associate Professor

Institute of Physics

Bhubaneswar

Date:

Acknowledgments

Now, at the end of the research period for my PhD thesis, I want to express my thanks to several people who have contributed to the thesis development.

First, I would like to express my sincere gratitude to my advisor Prof. P. V. Satyam for giving me the unique opportunity to work in his group and his look after as a father and as a guide. In his group, I enjoyed the freedom to make decisions and tried every absurd idea. I owe a great depth of gratitude to him for his continuous encouragement and enthusiastic motivation throughout and beyond this work. I am indebted to him for his excellent guidance and for providing excellent facilities. I am eternally thankful to him for teaching me some very important skills and supporting me on my career goals in every imaginable way. It is my very pleasure to thank for his fruitful input as a reader of this thesis.

I am grateful to the Director, IOPB for all the help I received from him during my stay here.

I would like to thank Prof. Andreas Roesnauer and his group members at University of Bremen, Germany as a collaborator for the investigations with 300 KeV Titan Machine.

I would like to thank Dr. Srihari Velaga for his support during the Synchrotron measurements at Photon Factory, Japan.

I would like to thank Department of Science and Technology, India for the financial support to visit and perform experiments at DESY, Hamburg, Germany and Saha Institute of Nuclear Physics, India for facilitating the experiments at the Indian Beamline, Photon Factory, KEK, Japan.

I would like to thank Dr. R. Sathyavathi and Prof. D. N. Rao and his group at University of Hyderabad, Hyderabad and Ajit, Dr. B. K. Jena and his group at Institute of Minerals and Materials Technology, Bhubaneswar for their support and help to perform SERS experiments.

I would like to thank our group postdocs Dr. P. K. Tyagi, Dr. P. Santhana Raman and Dr. Rajib Biswal for their help in academics as well as in other aspects.

It was a great pleasure for me to spend the last 5 years working in the Electron microscopy group. I am gratefully acknowledge the individual help and support from our TEM group members. I express thanks to all my colleagues for creating the pleasant atmosphere, especially Dr Jay Ghatak, Dr Umananda M Bhatta, Dr. Jatis K. Dash, Dr. Ashutosh Rath, Arnab, Anjan and Puspendu. Everyone has helped me one way or another. It is my innermost urge to Jay bhai, Umananda bhai, Ashutosh bhai , Jatis bhai for being the strongest supporters of me, for their patience with an unexperienced graduate student, for their guidance during my learning period and for sharing their intellectual property(both in academics and social issues). Arnab needs a special word of appreciation for his help in sharing the responsibility of running the microscopy facility (doing the routine maintenance work of our microscopy lab) and giving me ample time to finish writing my thesis.

I enjoyed the company of all my colleagues and many more and I would like to thank them for all their help in making my stay a pleasant experience here at IOPB. Multiple cheers go to all scholars (starting from 2008 predoc batch to 2013 batch) in the IOP campus. I feel so blessed that I have been surrounded by this set of nice people. A special word of appreciation goes to my batch mates Pramita, Raj and Tanmoy for their constant support and encouragement during the entire tenure of my Ph. D.

No experimental work would be successful without skilled technical support. Thanks to Mr S.R. Mohanty (Soumya), Mr B .K.Dash and Mr A.K Dash for providing it and always being patient, even if I had many requests. Thanks to Soumya for his continuous, quick and reliable help. I wish my all juniors (arnab, anjan and puspendu) all the best and a lot of success for the remaining part of their PhD studies.

I acknowledge the excellent library and computer facilities provided by the IOP and the timely help of all the academic as well as non academic staff.

Finally, but not the least I wish to express my deep sense of gratitude to my parents and sister. Your love has always been the very reason that motivates me to go forward. It was their encouragement, support and affection that helped me immensely in completing this thesis work. Most of all I am thankful to my wife Sampanna for her help, support and understanding the situations. My son vikram needs a word of appreciation for his energetic laughters which gave me energy to work hard.

TO MY PARENTS

List of Publications

1. ¹⁴Coherently Embedded Ag Nanostructures in Si: 3D Imaging and their application to SERS.
R. R. Juluri, A. Rath, A. Ghosh, A. Bhukta, R. Sathyavathi, D. N. Rao, Knut Muller, Marco Schowalter, Tim Grieb, Christian Frank, Florian Krause, A. Rosenauer and P. V. Satyam,
Sci. Rep. **4**, 4633 (2014).
2. ¹⁴Study of the buried Interfaces during the Silver Endotaxy in Silicon under various ambient conditions.
R. R. Juluri, A. Rath, A. Ghosh, A. Bhukta and P. V. Satyam,
Thin solid films(Under Review)
3. ¹⁴ Substrate Symmetry Driven Endotaxial Silver Nanostructures by Chemical Vapor Deposition.
R. R. Juluri, A. Rath, A. Ghosh and P. V. Satyam,
J. Phys. Chem. C **117**, 13245 (2013).
4. Real time nanoscale structural evaluation of gold structures on Si(100) surface using in-situ TEM.
A. Rath, **R. R. Juluri** and P. V. Satyam,
J. Appl. Physics **115**, 184303 (2014): arXiv:1204.4618.
5. Morphological variations in Au_xSi_y nanostructures under variable pressure and annealing conditions
A. Rath, J. K Dash, **R. R. Juluri** and P. V. Satyam,
Appl. Phys. A(Under Review).
6. Study of initial stages of growth of Au-assisted epitaxial Ge nanowires on Ge (100) Surface

- A. Rath, J. K. dash, **R. R. Juluri**, A. Ghosh and P. V. Satyam,
Cryst. Engg. Comm. **16**, 2486 (2014) :arXiv:1208.0238
7. Bi-functional Properties of $\text{Fe}_3\text{O}_4@ \text{YPO}_4$: Eu Hybrid Nanoparticles: Hyperthermia Application.
A. K. Parchur, A. I. Prasad, **R. R. Juluri**, R. S. Ningthoujam, R. K. Vatsa, B. N. Pandey, N.V. Jadhav,
Dalton Trans. **42** 8845 (2013).
 8. Uniformity of epitaxial nanostructures of CoSi_2 via defect control of the Si (111) surface.
J.C.Mahatho, D.Das, A.Roy, R.Batabyal, **R.R.Juluri**, P.V.Satyam and B.N. Dev,
Thin Solid films **534**, 296 (2013).
 9. Graphene induced Pd nanodendrites: A highly performance hybrid nanoelectrocatalyst.
Subash Chandra Sahu, Aneeya K. Samantara, Ajit Dash, **R.R.Juluri**, Ranjan K. Sahu, B. K. Mishra and Bikash Kumar Jena,
Nano Research **6**, 635 (2013).
 10. Nano scale phase separation in Au-Ge system on ultra clean Si(100) surfaces.
A. Rath, J. K. Dash, **R. R. Juluri**, Marco Schoewalter, Knut Mueller, A. Rosenauer and P.V. Satyam,
J. Appl. Phys. **111**, 104319 (2012): arXiv:1202.0614
 11. Growth of Oriented Au Nanostructures: Role of Oxide at the Interface.
A. Rath, J. K. Dash, **R. R. Juluri**, A. Rosenauer, Marco Schoewalter and P.V. Satyam,
J. Appl. Phys. **111**, 064322 (2012):arXiv:1203.0819
 12. Shape Evolution of MBE grown $\text{Si}_{1-x}\text{Ge}_x$ Structures on High Index Si(5 5 12) surfaces : A temperature tempendent study
J. K. Dash, A. Rath, **R. R. Juluri** and P. V. Satyam,
J. Physics D: Applied Physics **45**, 455303 (2012): arXiv:1205.6039
 13. Universality in Shape Evolution of $\text{Si}_{1-x}\text{Ge}_x$ Structures on High Index Silicon Surfaces

- J. K. Dash, T. Bagarti, A. Rath, **R. R. Juluri** and P. V. Satyam,
Euro. Phys. Lett. **99**, 66004 (2012): arXiv:1204.0578
14. Nanodot to Nanowire: A strain-driven shape transition in self-organized endotaxial CoSi₂ on Si (100).
J.C.Mahatho, D.Das, **R. R. Juluri**, R.Batabyal, A.Roy, P.V.Satyam and B.N.Dev,
App. Phys. Lett. **100**, 263117(2012).
15. Temperature dependent electron microscopy study of Au thin films on Si(100) with and without native oxide layer as barrier at the interface.
A. Rath, J. K. Dash, **R. R. Juluri**, A. Rosenauer and P.V. Satyam,
J. Physics D: Applied Physics **44**, 115301 (2011).
16. Synthesis of re-dispersible Ce³⁺ co-doped LaPO₄:Tb³⁺ nanorods and effects of concentrations of Ce³⁺ or Tb³⁺ and reaction medium on luminescence properties: luminescence switching behavior through redox reaction and polymer films.
G. Phaomei, R. S. Ningthoujam, W.R.Singh, R. S. Loitongbam, N. S. Singh, Ashutosh Rath, **R. R. Juluri** and R. K. Vatsa,
Dalton Trans. **40**, 115301(2011).
17. Shape transformation of Si_{1-x} Ge_x structures on ultra clean Si (5 5 7) and Si (5 5 12) surfaces.
J. K. Dash, A.Rath, **R. R. Juluri**, P Santhana Raman, K. Muller, M. Schowalter, R.Imlau, A. Rosenauer and P.V. Satyam
J. Phys.: Conf. Ser. **326**, 012021(2011).
18. DC heating induced shape transformation of Ge structures on ultra clean Si (5 5 12) surfaces
J. K. Dash, A. Rath, **R. R. Juluri**, P Santhana Raman, K. Muller, A. Rosenauer and P.V. Satyam ,
J. Phys.: Condens. Matter **23**, 135002 (2011).

Conference Presentations

1. ^{1†} Study of Endotaxial Silver nanostructures
R.R.Juluri, A. Ghosh, A. Bhukta and P. V. Satyam
PSI-2014, Puri, India.

2. ^{1‡} Synthesis of Single Crystalline Silver Endotaxial nanostructures by CVD.
R. R. Juluri, A. Ghosh, A. Rath, A. Bhukta and P. V. Satyam
1st PF User Meeting -2013, SINP, Kolkata, India.
3. ^{1‡} Electron Microscopy Study of CVD prepared Ag Endotaxial structures
R. R. Juluri, A. Ghosh, A. Bhukta, A. Rath and P. V. Satyam
EMSI-2013, SINP, Kolkata, India.
4. A Simple Low Vacuum Annealing Method for Tuning the Shape of Oriented Au Nanostructures
A. Rath, J. K. Dash, **R. R. Juluri**, A. Rosenauer and P. V. Satyam,
EMSI-2012, IISc, Bangalore, India.
5. Shape transition in Au/Si(100) System : Role of surface oxide and vacuum Level.
A. Rath, J. K. Dash, **R. R. Juluri** and P. V. Satyam,
ICONSAT-2012, Hyderabad, India.
6. Shape transition in Au/Si(100) hetero epitaxial system: Role of vacuum level during annealing
A. Rath, J. K. Dash, **R. R. Juluri** and P. V. Satyam,
ICANN-2011, Guwahati, Assam, India.
7. Nano pattern formation in Ge/Au/Si(100) hetero epitaxial system
A. Rath, J. K. Dash, **R. R. Juluri** and P.V. Satyam,
IINM-2011, International conference on Ion beam induced nano patterning of materials Institute of Physics, Bhubaneswar, India.

^{1‡} Papers on which this thesis is based upon.

Synopsis

Epitaxial growth of nano-scale structures deals with coherent growth of structures on crystalline substrate surfaces [1]. Usually, the metal epitaxial films are grown under ultra high vacuum (UHV) conditions using conventional method like molecular beam epitaxy (MBE) [2]. Similarly, coherent structures can be grown inside single crystals, and this process of growing embedded crystalline structures (which is usually done under UHV conditions) is known as endotaxy [3,4]. The thesis work is focused on the growth of coherently *embedded* silver nanostructures in silicon substrate under various annealing conditions. A novel method to prepare silver endotaxial structures of specific shape depending upon the substrate orientations, at ambient conditions (where no vacuum is required) in silicon substrate is presented in this thesis work. A detailed characterization using *ex-situ* high resolution transmission electron microscopy, Rutherford back scattering spectrometry, and *in-situ* and real time x-ray scattering methods have been carried out so as to understand and optimize the growth process. These structures are utilized for detection of crystal violet (CV) molecules of 5×10^{-10} M concentrations. These are expected to be one of the highly robust, reusable and novel substrates for single molecule detection. Synthesis of embedded gold nanostructures in silicon substrate (Si(100)) would also be reported.

In the area of nanoscience and nanotechnology, metal nanoparticles are being studied for their potential applications as catalysts [5], sensors [6] and surface enhanced raman spectroscopy (SERS) substrates, etc. For example, gold nanoparticles are well known for their excellent catalytic properties to grow nanowires by vapor-liquid-solid (VLS) mechanism [7–9] and it is a building block for nano-bioelectronic devices [10, 11]. Silver is also a promising candidate at nanoscale to give wonderful results as SERS substrate to detect very low concentrations of molecules. Without utilizing the field enhancement in SERS method, it is not possible to detect the most challenging aspect, that of detection of single bio-molecule. Due to surface plasmons

of metal nanoparticles, intensity of Raman scattering is enhanced [12]. The success and the usefulness of the SERS method depends on the optimization of the interaction between adsorbed molecules and the surface plasmonic structures [13]. The plasmonic properties are greatly affected by size, shape, dielectric constant of the surrounding matrix. Besides plasmonic applications, silver nanostructures can also be used as photonic crystals, infrared polarizers [14, 15] and superlens and hyperlens applications due to its lowest on resonance loss of any natural noble metal at optical frequencies [16, 17]. Incorporation of Ag nanostructures on the semiconductor surface and at the interfaces, with various shapes of Ag nanostructures would help integrating the interesting optical properties of Ag nanostructures with those semiconductor properties (Opto-Nanoelectronics). Surface plasmon polaritons (SPPs) excited in noble metal structures adjacent to gain media, dramatically shrink the optical mode volume and provide the necessary feedback mechanism for a surface plasmon amplification by stimulated emission of radiation (SPASER) [18]. Epitaxial growth of silver at silicon interface is the key factor for reducing the modal volume and plasmonic losses. This thesis work is focused on the growth of silver endotaxial nanostructures at various ambient conditions using GeO_x layer as an etching layer at the Si interface to enhance the desorption of native oxide. It is known that the native oxide on silicon surface can be removed by flashing the substrate at 1200 °C under UHV conditions. The thesis works reports a novel method, where in the native oxide (SiO_2) desorption (on silicon) can be made possible at relatively low temperatures (800 °C) and under ambient conditions (i.e. such as air annealing) by using an interfacial layer, such as, GeO_x , which enhances the rate of desorption of native oxide of silicon. Also, by performing various combinations of these layers (SiO_x or GeO_x or Ag), the size and formation of dielectric layers surrounding the endotaxial structures can be tuned.

The thesis is organized as follows: Introduction and motivation to work in the area of surfaces and interface is discussed in Chapter one. It also discusses the importance of these nanostructures with respect to their optical and catalytic properties and different routes of synthesis of these nanostructures.

Chapter two describes the experimental characterization methods that have been used for the research work carried out related to the thesis. Transmission electron microscopy (TEM), high resolution TEM (HRTEM), scanning TEM (STEM) based

three dimensional (3D) tomography and energy dispersive x-ray analysis (EDX), scanning electron microscopy (SEM), Rutherford backscattering spectrometry (RBS) and synchrotron x-ray diffraction (XRD) measurement, and surface enhanced Raman spectroscopy (SERS) have been extensively used to illustrate the formation of nanostructures and their properties. Physical vapor deposition method (PVD) and chemical vapor deposition (CVD) method are used to deposit thin films. The physical principles of different techniques and their application to understand the various aspects of formation of the nano/micro structures have been presented. Remaining chapters of this thesis describe the study of formation of endotaxial Ag nanostructures and their SERS applications and dependence of ambience on these structures and their uses as SERS substrates.

Chapter 3 deals with the study of growth of endotaxial structures, a detailed analysis of three dimensional (3D) imaging using STEM base tomography and applications of these nanostructures as SERS substrates. A ≈ 2 nm silver film is deposited on top of 17 nm GeO_x coated silicon substrate of (100), (110), (111) orientations by thermal vapor deposition method. These samples were annealed in air up to 800 °C. Endotaxial nano square/rectangular structures are formed in the case of Si(100), endotaxial nanorods are formed on Si(110) and endotaxial nano triangles are formed for Si(111) substrate according to their respective substrate symmetries. Chemical analysis of these structures along with their 3 dimensional shape studies were discussed for the case of Si(100) substrate orientation. These samples are used as SERS substrate. Role of the GeO_x presence in the formation of silver endotaxial structures was explained and absence of GeO_x yields Ag_xSi_y endotaxial structure formation. Not only presence of GeO_x influences the formation of these endotaxial structures but also the position of GeO_x plays a key role [19].

In the chapter 4, the work reports on the role of ambience during annealing so as to optimize the process for the formation of endotaxial structures. Annealing of the 2 nm Ag/17 nm $\text{GeO}_x/\text{SiO}_x/\text{Si}(100)$ substrate annealed at 800 °C in different ambience *viz* oxygen, ultra high vacuum, air, low vacuum and argon and their resultant outcome is discussed in this chapter. Growth of endotaxial structures was not found either in very high oxygen availability (like under oxygen flow) or very negligible oxygen availability (like HV/UHV conditions). Silver endotaxial nanostructures with

different sizes and shapes were synthesized under air, low vacuum and argon ambient conditions whereas embedded silver nanostructures were obtained for the case oxygen ambience. The thesis work shows that oxygen partial pressure plays a crucial role in the formation of endotaxial structure formation. In the case of endotaxial structures, varying the annealing ambient resulted in the matrix around the Ag nanostructures: such as only SiO_x or GeO_x or combination of SiO_x and GeO_x and Si [20].

The surface and interface energies play a crucial role in the growth of nanostructures during self-assembly and real time and *in-situ* experimental methods help in understanding the growth kinetics. Chapter 5 deals with the *in-situ* XRD study of Ag endotaxial nanostructures growth. For this, temperature dependent synchrotron XRD study of 2 nm Ag/17 nm $\text{GeO}_x/\text{SiO}_x/\text{Si}$ with all three orientations was carried out using a heating stage(M/S Anton Paar). In the case of Si(100) orientation, Ag(111) peak was started evolving around 500 °C and the peak intensity is increased continuously upto 700 °C, afterwards the peak intensity is decreased. Meanwhile, Ag(200) peaks started appearing around 575 °C and its intensity increased continuously upto 800 °C. After 650 °C, the growth of Ag(200) peak was growing with expense of Ag(111) peak which helps in determination of understanding the phase transformations during the annealing process. Similar measurements have been made for remaining two orientations as well where the interface comes into play around 650 °C. In order to generalize this mechanism, we study the case of gold of GeO_x coated silicon substrate and found the endotaxial gold nanostructures by *ex-situ* annealing of 2 nm Au/5 nm $\text{GeO}_x/\text{SiO}_x/\text{Si}(100)$ at 800 °C in air [21].

For a better understanding of the role of GeO_x in the formation of these endotaxial structures and the effect of temperature for the formation of these endotaxial structures different thicknesses of GeO_x *i.e.* 5 nm, 17 nm and 60 nm was deposited on Si substrate and annealed upto 800 °C in air was discussed in chapter 6. For 5 nm GeO_x , no substrate symmetric silver nanostructures were observed whereas for the gold case substrate symmetric endotaxial structures were observed. For 17 nm GeO_x , in the case of silver endotaxial structures were observed whereas for gold case only spherical gold nanostructures were observed on top of GeO_x layer. For 60 nm GeO_x , only silver was deposited and endotaxial structures were observed. Role of temperature was studied for the case of 2 nm Ag/17 nm $\text{GeO}_x/\text{SiO}_x/\text{Si}(100)$. Samples were

annealed at different temperature ranging from 700 °C to 800 °C with an interval of 50 °C in ambience and found that 750 °C is the critical temperature for the endotaxial structures formation for the sample in the case of silver.

All the above cases, PVD deposited metal was present on the GeO_x coated silicon substrates. In the chapter 7, deposition of silver was done using chemical vapor deposition and study the formation of endotaxial structures. Substrate symmetry driven silver nanostructures are synthesized on silicon surface by CVD method using silver as a source with 17 nm $\text{GeO}_x/\text{SiO}_x/\text{Si}$ samples in atmosphere at 800 °C. Endotaxial nano squares/rectangles are formed in the case of Si (100), endotaxial nanorods are formed on Si (110) and endotaxial nano triangles are formed for Si(111) substrate according to their 4-fold, 2-fold and 3-fold symmetries respectively. Control over coverage can be obtained by varying the deposition time [22]. Deposition temperature also plays a crucial role in the formation of these structures in the CVD deposition [23]. To understand the role of deposition temperature in the CVD process on these silver endotaxial structures formation, shape and size of the nanostructures. Silver endotaxial structures were synthesized at different deposition temperatures using CVD technique on 17 nm $\text{GeO}_x/\text{SiO}_x/\text{Si}(100)$. From X-TEM images, the structures grown at 800 °C are the smallest among all other temperatures and structures grown at 900 °C are the biggest structures. At 850 °C the size of the silver endotaxial structures is in between 800 °C and 900 °C structures size.

To explore the applications of Ag nanostructures, we have tested these substrates with Ag nanostructures as substrates for SERS to detect organic molecules at very low concentration. Chapter 8 deals with the SERS applications of these endotaxial nanostructures grown by both PVD and CVD methods. For SERS applications PVD grown nano square/rectangular silver structures were studied with crystal violet molecules of 0.5 nM concentrations. The same concentration of CV was used to study the CVD grown endotaxial nanostructures also. SERS studies were done for different shaped nanostructures i.e. for nano squares/rectangles, nanorods and nano triangles. Not only the shape dependence but also the coverage dependence on SERS enhancement factors was also studied.

The last chapter i.e. chapter 9 summarizes the work presented in the thesis and emphasizes on the possible further research in this area.

Bibliography

- [1] M. A. Herman, W. Richter and H. Sitter, *Epitaxy: Physical Principles and Technical Implementations* (Springer, 2004).
- [2] A. Y. Cho and J. R. Arthur, *Prog. in Solid State Chem* **10**, 157 (1975).
- [3] I. Bonev, *Acta. Cryst. A* **28**, 508 (1972).
- [4] P. A. Bennet, Z. He, D. J. Smith and F. M. Ross, *Thin Solid films* **519**, 8434 (2011).
- [5] A. T. Bell, *Science* **299**, 1688 (2003).
- [6] S. O. Obare, R. E. Hollowell, and C. J. Murphy, *Langmuir* **18**, 10407 (2002).
- [7] H. Adhikari, A. F. Marshall, I. A. Goldthorpe, C. E. D. Chidsey and P. C. McIntyre, *ACS Nano* **1**, 415 (2007).
- [8] R. S. Wagner and W. C. Ellis, *Appl. Phys. Lett.* **4**, 89 (1964).
- [9] Y. Wu and P. Yang, *J. Am. Chem. Soc.* **123**, 3165 (2001).
- [10] M. G. Warner and J. E. Hutchison, *Nature Materials* **2**, 272 (2003).
- [11] Y. Xiao, F. Patolsky, E. Katz, J. F. Hainfeld and I. Willner, *Science* **299**, 1877 (2003).
- [12] K. Kneipp, M. Moskovits and H. Kneipp, *Surface Enhanced Raman Scattering : Physics and Applications* (Springer 2004).
- [13] B. Sharma, R. R. Frontiera, A. I. Henry, E. Ringe and R.P. Van Duyne, *Mat. Today* **15**, 16 (2012).
- [14] X. Hu and C. T. Chan, *Appl. Phys. Lett.* **85**, 1520 (2004).

- [15] Y. T. Pang, G. W., Meng, Q. Fang and L.D. Zhang, *Nanotechnology* **14**, 20 (2003).
- [16] P. B. Johnson and R. W. Christy, *Phys. Rev. B* **6**, 4370 (1972).
- [17] V. P. Darchev, U. K. Chettiyar, A. K. Kildishev, H. K. Yuan, W. Cai and V. M. Shalev, *Optics Express* **16**, 1186 (2007).
- [18] Y. J. Lu et.al., *Science* **337**,450 (2012).
- [19] R. R. Juluri, A. Rath, A. Ghosh, A. Bhukta, R. Sathyavathi, D. Narayana Rao, K. Muller, M. Schowalter, K. Frank, T. Grieb, F. Krause, A. Rosenauer and P. V. Satyam, *Sci. Rep.* **4**, 4633 (2014).
- [20] R. R. Juluri, A. Ghosh, A. Bhukta and P. V. Satyam, *J. Appl. Phys.* (Submitted, 2014).
- [21] R. R. Juluri, A. Ghosh, A. Bhukta and P. V. Satyam, (To be submitted, 2014).
- [22] R. R. Juluri, A. Ghosh, A. Bhukta and P. V. Satyam, *J. Phys. Chem. C* **117**, 13747 (2013).
- [23] A. C. Jones and M. L. Hitchman, *Chemical Vapor Deposition: Precursors, Processes and Applications* (RSC Publishing, Cambridge 2009).

Contents

Statement By Author	ii
Declaration	iii
Certificate	iv
Acknowledgments	v
List of Publications	ix
Synopsis	xiii
1 Introduction	1
2 Experimental Techniques	6
2.1 Introduction	6
2.2 Thin Film Growth	7
2.2.1 Physical Vapor Deposition Method	7
2.2.2 Chemical Vapor Deposition	8
2.2.3 Low Vacuum Annealing Setup	11
2.3 Characterization techniques	11
2.3.1 Transmission Electron Microscopy	11
2.3.2 FIB-SEM-Cross beam system	21
2.3.3 Scanning Transmission Electron Microscopy (STEM)	27
2.3.4 X-Ray Diffraction	30
2.3.5 Rutherford Backscattering Spectrometry	34
2.3.6 Raman Spectroscopy	37

3	Coherently Embedded Ag Nanostructures in Si : 3D Imaging	41
3.1	Introduction	41
3.2	Experimental Section	42
3.3	Results and discussion	43
3.3.1	Growth of Endotaxial Ag nanostructures in Si(100): A simple PVD method	43
3.3.2	Plausible Mechanism	46
3.3.3	Chemical Analysis and 3D Imaging	47
3.3.4	Other Substrate Orientations i.e. Si(110), Si(111)	50
3.3.5	Role of GeO _x Layer	51
3.4	Chapter Summary	54
4	Study of the Buried Interfaces during the Silver Endotaxy in Silicon under Various Ambient Conditions	55
4.1	Introduction	55
4.2	Experimental methods	56
4.3	Results and discussions	57
4.4	Chapter Summary	67
5	Real Time In-situ XRD Study of Endotaxial Growth of Ag Nanostructures in Silicon	68
5.1	Introduction	68
5.2	Experimental details	69
5.3	Results and discussion	72
5.4	Chapter Summary	75
6	Effect of GeO_x Thickness and Annealing Temperatures on Ag Endotaxial Nanostructures	79
6.1	Introduction	79
6.2	Experimental details	80
6.3	Results and discussion	81
6.3.1	Temperature Dependent Study	81
6.3.2	Thickness Dependent Study	85
6.4	Chapter Summary	90

7	Substrate Symmetry Driven Endotaxial Silver Nanostructures by Chemical Vapor Deposition	91
7.1	Introduction	91
7.2	Experimental Methods	93
7.3	Results and discussions	93
7.4	Chapter Summary	102
8	Applications of Endotaxial Silver Nanostructures as SERS Substrates	103
8.1	Introduction	103
8.2	Experimental details	104
8.3	Results and discussion	105
	8.3.1 PVD based Ag endotaxial structures	105
	8.3.2 CVD based Ag endotaxial structures	107
8.4	Chapter Summary	113
9	Summary	114
	Bibliography	117

List of Figures

2.1	A schematic diagram of precursor transport and reaction process in CVD [77]	9
2.2	A schematic diagram of Diffraction pattern (DP) formation and Image formation [78].	14
2.3	A schematic diagram of different processes taking place during electron-solid interaction.	15
2.4	200 keV JEOL HRTEM installed at Institute of Physics, Bhubaneswar.	18
2.5	A schematic diagram of procedure to prepare a typical planar TEM specimen.	19
2.6	A schematic diagram of procedure to prepare a typical cross-sectional TEM specimen.	19
2.7	FIB-SEM crossbeam system installed at Institute of Physics, Bhubaneswar.	23
2.8	A schematic diagram of different processes taking place during electron–solid interaction	25
2.9	Schematic diagram illustrates the various signals generated inside a scanning transmission electron microscope that can be used to form high-resolution images, nanodiffraction patterns or spectra of the region-of-interest. X-ray energy dispersive spectroscopy (XEDS); Auger electron spectroscopy (AES) and scanning Auger microscopy (SAM); secondary electron spectroscopy (SES) and secondary electron microscopy (SEM); annular dark-field (ADF) and high-angle annular dark-field (HAADF); coherent electron nano-diffraction (CEND); parallel electron energy-loss spectroscopy (PEELS); bright-field (BF) and dark-field (DF) [88].	28
2.10	Schematic diagram of Braggs Law	30
2.11	Experimental setup to perform X-ray diffraction installed at Indian beam line 18-B, Photon Factory, Japan	32

2.12	Heating stage used to perform the <i>in-situ</i> XRD measurements at Photon Factory, Japan (model DHS 1100, Anton Paar GmbH.)	33
2.13	A schematic diagram of the interaction of two particles [93].	34
2.14	A schematic diagram of the RBS spectrum for a thin film [93].	35
2.15	Schematic diagram of Raman scattering	37
3.1	Planar TEM Micrographs of 2 nm Ag/17 nm GeO _x /SiO _x on (a) Si(100), (b) Si(110) and (c) Si(111) annealed at 800 °C in air.	44
3.2	X-TEM Micrographs of 2 nm Ag/17 nm GeO _x /SiO _x /Si (100) (a) Low Mag of as-deposited (b) Low Mag of 800 °C annealed in air (c) HR-X-TEM depicts endotaxial structures (with Moire fringes) and (d) X-ray diffraction pattern showing the single crystalline nature of the Ag nano structures which also complimented by a selected area diffraction (SAD) pattern taken from a single structure.	45
3.3	STEM- EDX Elemental of mapping 2 nm Ag /17 nm GeO _x /SiO _x /Si (100) at 800 °C (a) STEM Micrograph, (b) Oxygen mapping, (c) Si mapping, (d), (e) Ge K, L mapping and (e) Ag mapping	48
3.4	(a) STEM HAADF micrograph of 2 nm Ag/17 nm GeO _x / SiO _x / Si(100) at 800 °C annealed in air, with selected directions indexed from this 2D projection. (b) Reconstructed 3D tomography view of one of the endotaxial islands, showing that the silver embedment is terminated by (111) facets and an (001) base. (c) Result of the Wulff construction, explaining this pyramidal shape and its orientation theoretically in terms of interface energy	49
3.5	X-TEM Micrographs of 2 nm Ag/17 nm GeO _x /SiO _x /Si(110) at 800 °C in air (a) Low Mag X-TEM (b) HR-X-TEM depicts endotaxial structures (with Moire fringes) and (c) Diffraction pattern on single structure	50
3.6	X-TEM Micrographs of 2 nm Ag/17 nm GeO _x /SiO _x /Si (111) at 800 °C in air (a) Low Mag X-TEM (b) HR-X-TEM depicts endotaxial structures (with Moire fringes) and (c) Diffraction pattern from a single structure	51

3.7	(a) SEM Micrograph of 2 nm Ag/SiO _x /Si (100) at 800 °C in air, X-TEM Micrographs of 2 nm Ag/SiO _x /Si (100)(b) as-deposited and annealed at 800 °C in air (c) Low Magnification (d) HRTEM of selected area depicts endotaxial structures.	52
3.8	X-TEM Micrographs of (a) low mag of as-deposited 17 nm GeO _x /2 nm Ag /SiO _x /Si (100) (b) Low Mag (c) HR-X-TEM of 17 nm GeO _x /2 nm Ag /SiO _x /Si (100) @ 800 °C in air respectively.. . . .	53
4.1	SEM Micrographs of 2 nm Ag /17 nm GeO _x /SiO _x / Si(100) (a) As-deposited (b) Annealed in oxygen (c) Annealed in UHV at 800 °C for 30 minutes.	58
4.2	X-TEM Micrographs of 2 nm Ag /17 nm GeO _x /SiO _x / Si(100) (a) As-deposited (b) Annealed in oxygen (c) Annealed in UHV at 800 °C for 30 minutes.	59
4.3	(a) SAED Pattern showing a polycrystalline rings of Ge, (b) HRX-TEM complementing the SAED result for 2 nm Ag /17 nm GeO _x /SiO _x / Si(100) annealed at 800 °C in UHV	60
4.4	SEM Micrographs of 2 nm Ag/17 nm GeO _x /2 nm SiO _x /Si(100) (a) Annealed in air (b) Annealed in low vacuum. (c) Annealed in argon at 800 °C for 30 minutes.	61
4.5	X-TEM Micrographs of 2 nm Ag/17 nm GeO _x /2 nm SiO _x /Si(100) (a) Annealed in air (b) Annealed in low vacuum. (c) Annealed in argon at 800 °C for 30 minutes.	61
4.6	Schematic diagram explaining the consideration of height, depth, length and breadth of the silver endotaxial nanostructures.	63
4.7	(a) RBS Spectra of experimental and simulated data of 2 nm Ag /17 nm GeO _x /SiO _x / Si(100) as-deposited case, (b) comparative RBS spectrums of 2 nm Ag /17 nm GeO _x /SiO _x / Si(100) as-deposited, Annealed in air, oxygen, low vacuum and argon at 800 °C for 30 minutes and (c) comparative peak positions of Ge and Ag of RBS spectrum.	66
4.8	XRD spectrum of 2 nm Ag /17 nm GeO _x /SiO _x / Si(100) annealed at 800 °C in low vacuum (b) SAED pattern taken on a single Ag nano structure for AGS-LV and (c) comparative HR-XRD spectrum of Ag(002), Ag(004) peaks for different ambiances.	67

5.1	Schematic diagram of the experimental geometry used to perform the <i>in-situ</i> annealing of the samples at Photon factory, KEK, Japan. . . .	70
5.2	Schematic diagram showing the relation between the axes of silver and silicon crystals along with the surface normal of the corresponding substrate.	70
5.3	Schematic diagram of the experimental procedure followed during in-situ annealing and cooling of (a) 4 nm Ag/ 17 nm GeO _x /SiO ₂ /Si(100) sample continuous ramping for heating and cooling (Numbers in the paranthesis denotes the time for which the specimen has been kept at that temperature)(b) 4 nm Ag/ 17 nm GeO _x /SiO ₂ /Si(100) sample's stepwise annealing and stepwise cooling, (c) 4 nm Ag/ 17 nm GeO _x /SiO ₂ /Si(110) sample's stepwise annealing and stepwise cooling and (d) 4 nm Ag/ 17 nm GeO _x /SiO ₂ /Si(111) sample's stepwise annealing and stepwise cooling. At each step sample was kept for 10 minutes for achieving equilibrium and then the XRD measurements were taken.	71
5.4	(a) Plot of peak areas of HR-XRD spectrum of Ag(002) peaks of 4 nm Ag/17 nm GeO _x /SiO _x / Si(100) annealed in-situ up to 800 °C in air with respect to temperature increment, (b) plot of Ag(002) peak area with respect to stabilization time at 800 °C. (c)Plot of Ag(002) peak position shift (d) calculated lattice constants corresponding to the Ag(002) peak shift and theoretical fitting using thermal expansion of silver during the cooling of 4 nm Ag/17 nm GeO _x /SiO _x / Si(100) annealed in-situ up to 800 °C in air.	74
5.5	(a) 3D plot of Ag(111) and Ag(002) peaks (b) plot of Ag(111) and Ag(002) peak areas with respect to temperature during the annealing of 4 nm Ag/17 nm GeO _x /SiO _x / Si(100) in-situ up to 800 °C in air (c) plot of intensity ratio of Ag(200) to Ag(111) with respect to temperature.	76
5.6	Peak evolution of (a) Ag(111) (b) Ag(002) peaks and (c) 3D plot of Ag(220) with respect to increasing temperature during the annealing of 4 nm Ag/17 nm GeO _x /SiO _x /Si(110) in-situ up to 800 °C in air. . .	77
5.7	(a) 3D plot of Ag(111) peak (b) Plot of Ag(111) peak areas with respect to temperature during the annealing of 4 nm Ag/17 nm GeO _x /SiO _x /Si(111) in-situ up to 800 °C in air.	77

6.1	SEM micrographs of 2 nm Ag/17 nm GeO _x /SiO _x / Si(100) annealed at different temperatures in air (a) 700 °C (b) 750 °C (c) 800 °C	81
6.2	X-TEM Micrographs of 2 nm Ag/17 nm GeO _x /SiO _x /Si(100) annealed up to 700 °C in air (a) Low Mag (b) HR-X-TEM depicts silver nanostructures and (c) Diffraction pattern from a single structure	82
6.3	X-TEM Micrographs of 2 nm Ag/17 nm GeO _x /SiO _x /Si(100) annealed up to 750 °C in air (a) Low Mag (b) HR-X-TEM depicts silver nanostructures and (c) Diffraction pattern from a single structure	83
6.4	X-TEM Micrographs of 2 nm Ag/17 nm GeO _x /SiO _x /Si(100) at 800 °C annealed in air (a) Low Mag (b) HR-X-TEM depicts endotaxial structures (with Moire fringes) and (c) Diffraction pattern from a single structure	83
6.5	(a) Comparative RBS spectrum (b) Ge and Ag edges and (c) comparative HRXRD Ag (002) reflection of 2 nm Ag/17 nm GeO _x /SiO _x /Si(100) annealed at 700 °C, 750 °C and 800 °C in air	85
6.6	SEM Micrographs of 2 nm Ag on (a) 5 nm GeO _x (b) 17 nm GeO _x (c) 60 nm GeO _x on SiO _x /Si(100) annealed at 800 °C in air for 30 minutes.	86
6.7	X-TEM Micrographs of 2 nm Ag /5 nm GeO _x /SiO _x /Si(100)@800 °C annealed in air(a) Low Mag (b) HR-X-TEM depicts endotaxial structures (with Moire fringes) and (c) Diffraction pattern from a single nanostructure.	87
6.8	X-TEM Micrographs of 2 nm Ag /60 nm GeO _x /SiO _x /Si(100) at 800 °C annealed in air (a) Low Magnification (b) Diffraction pattern from a single nanostructure revealing the endotaxial nature of the nanostructure.	88
6.9	X-TEM Micrographs of 2 nm Au /5 nm GeO _x /SiO _x /Si(100) (a) as deposited (b)Low Mag of sample annealed at 800 °C in air for 30 minutes and (c) Diffraction pattern on single nanostructure.	89
6.10	X-TEM Micrographs of 2 nm Au /17 nm GeO _x /SiO _x /Si(100) (a) as deposited (b)Low Mag of sample annealed at 800 °C in air for 30 minutes and (c) Diffraction pattern on nanostructures.	90
7.1	SEM Micrographs of Silver nanostructures deposited using Ag-wire as a source on (a) SiO _x / Si (100) (b) SiO _x / Si (110) at 800° C in air for 30 minutes.	94

7.2	X-TEM Micrographs of Silver nanostructures deposited using Ag-wire as a source on SiO _x / Si (100) at 800° C in air for 30 minutes (a) Low mag X-TEM (b) HR-X-TEM (c) SAED showing pure single crystalline silver.	95
7.3	TEM Micrographs of as deposited GeO _x on Si(100) using PVD method (a) Low mag (b) HRTEM (c) SAED showing amorphous GeO _x layer.	95
7.4	SEM Micrographs of Silver nanostructures deposited using Ag wire as a source on 17 nm GeO _x deposited (a) Si(100), (b) Si(110), (c) Si(111) substrates at 800° C in air for 30 minutes.	96
7.5	TEM Micrographs of Ag nanostructure on Ge/SiO ₂ /Si(100) at 800 °C for 30 minutes (a) Planar TEM image (b) Low magnification X-TEM image (c) HR-X-TEM image and (d) SAED on single structure.	98
7.6	SEM Micrographs of Silver nanostructures deposited using Ag wire as a source on 17 nm GeO _x deposited (a) Si(110) (b) Si(111) substrates at 800 °C in air for 60 minutes.	99
7.7	SEM Micrographs of Silver nanostructures deposited using Ag wire as a source on 17 nm GeO _x deposited Si(100) at (a) 800 °C (b) 850 °C and (c) 900 °C in air for 30 minutes.	99
7.8	X-TEM Micrographs of Silver nanostructures deposited using Ag wire as a source on 17 nm GeO _x deposited Si(100) at (a) 800 °C (b) 850 °C and (c) 900 ° C in air for 30 minutes.	100
7.9	(a)Comparative XRD spectra of Ag(002) of CVD deposited Ag on 17 nm GeO _x /SiO _x /Si(100) at deposition temperature of 800 °C, 850 °C and 900 °C in air, deconvoluted plots of asymmetric Ag(002) peak for (b) 850 °C (c) 900 °C deposition temperatures.	101
8.1	(a) SEM Micrographs of 2 nm Ag/17 nm GeO _x / SiO _x / Si(100) at 800 °C in air (b)after etched with Hydro fluoric acid for 90 minutes (c) SERS spectrum of Crystal Violet (CV) with a concentration of 5 × 10 ⁻¹⁰ M drop casted on 2 nm Ag/17 nm GeO _x / SiO _x / Si(100) at 800 °C in air etched with HF for 90 min and (d) SERS spectrum of Crystal Violet (CV) of above the sample at different points denoted by different colors showing the consistency of the substrate with uniform enhancement.	106

8.2	SEM micrographs of 2 nm Ag/ 17nm GeO _x / SiO _x / Si(100) at 800 °C in (a) low vacuum (b) UHV ambiances and (c) comparative SERS spectra of CV (5×10 ⁻¹⁰ M) on (a), (b)	108
8.3	(a) comparative SERS spectrum of CV of 5×10 ⁻¹⁰ M on Ag/17 nm GeO _x /SiO _x /Si(100), Ag/17 nm GeO _x /SiO _x /Si(110), Ag/17 nm GeO _x /SiO _x /Si(111) substrate at 800 °C in air for deposition time of 30 minutes (b) comparative SERS spectrum of CV of 0.5 nM on Ag/17 nm GeO _x /Si(110), Ag/17 nm GeO _x /SiO _x /Si(111) substrate at 800 °C in air for deposition time of 60 minutes.	109
8.4	SEM Micrographs of Silver nanostructures deposited using Ag wire as a source on 17 nm GeO _x /SiO _x /Si(110) substrate at 800 °C in air for (a) 30 minutes (b) 60 minutes and (c) SERS spectrum of 0.5 nM CV on (a) and (b)	110
8.5	SEM Micrographs of Silver nanostructures deposited using Ag wire as a source on 17 nm GeO _x /SiO _x /Si(111) substrate at 800 °C in air for (a) 30 minutes (b) 60 minutes and (c) SERS spectrum of 0.5 nM CV on (a) and (b)	111
8.6	(a) SERS spectrum of 0.5 nM R6G on Silver nanostructures deposited using Ag wire as a source on 17 nm GeO _x /SiO _x /Si(110) substrate at 800 °C in air for 30 minutes (b) SERS spectra of R6G of above sample at different points denoted by different colors showing the consistency of the substrate with uniform enhancement.	112
8.7	(a) SERS spectrum of Creatinine on Silver nanostructures deposited using Ag wire as a source on 17 nm GeO _x /SiO _x /Si(100) substrate at 800 °C in air for 30 minutes (b) SERS spectra of Creatinine of above sample at different points denoted by different colors showing the consistency of the substrate with uniform detection.	112

Chapter 1

Introduction

Recently, the area of nanoscience and nanotechnology is growing very rapidly and is one of the emerging fields which has impact on many fields due to its diversified applications. Information technology and communication, medicine, materials, space, energy, water *etc* [1–7] are some of the fields where the nanoscience shows its virtue. Important achievements were already achieved in the area of nanoscience and nanotechnology. For instance, in realization of molecular-scale transistors using semiconducting carbon nanotubes [8] and superiority of semiconductor quantum dots in high power laser diodes [9] are some such examples. The potential application of hexagonal mesoporous silica in catalysis [10] and in controlled drug release [11] has also been demonstrated. Nanoparticles are often applied as additives *e.g.* for the reinforcement of steel [12] and for the production of precipitation-hardened alloys [13]. Material properties at nanoscale are different for two main reasons : nanomaterials have a large surface area compared to the same mass of material at its bulk form, which make materials more chemically reactive and affect their strength or electrical properties. Significance of grain boundaries increased due to the increase of surface to volume ratio at nano level. Thus, nanoparticles often exhibit exceptional physical properties such as, high coercive force [14], giant magneto-resistance [15], high thermal stability and super plasticity [13,16]. It is also expected that the quantum effects begin to dominate the behavior (optical, magnetic and electrical) of materials at this nano level. Size [17,18], shape [19], surface composition [20], dielectric environment around the particle [21] and the inter particle interactions [22] are the key factors that can modulate the chemical, optical, magnetic and electronic properties of nanomaterials [23]. As the nanoparticle size/shape plays a crucial role on their properties,

studies of the particle size and shape evolution could be useful in providing an insight into the manipulation and control of their properties and functionalities. Thus, the uniformity of the size and shape of the nanoparticles is a key factor for the design of novel advanced functional nanomaterials. Dependence of catalytic behavior of the nanoparticles with their shape is shown by several groups in literature [24].

Metallic nanoparticles are interesting due to their usage in the preparation of new materials for energy storage, communication, photonics, and sensing application [25–28] due to their optoelectronic, thermal, magnetic and excellent catalytic properties [29–32]. Conduction band is discrete in the case of nanoparticles due to quantum confinement of the electrons which is not possible in bulk metals. Metal nanoparticles are drawing great attention due to their potential applications such as seed particles (Pt, Au, Ag) and as catalysts for nanowire growth [33–36]. These particles are also suitable as optical materials due to their Surface Plasmon Resonance (SPR) properties. Owing potential applications of these nanoparticles, synthesis of metal nanoparticles with uniform size, desired shapes in large scale by cost effective methods are gathering potential interest. Among metal nanoparticles, gold and silver are of the metals which gathers great interest due to their potential applications. Silver is a very good candidate for photonic materials because of its lowest on-resonance loss at optical frequencies [37, 38]. The surface plasmon which is a collective oscillation of conduction electrons in phase with the incident light. By controlling the shape of the nanostructures, one can control the ways in which electrons oscillate, and in turn how the nanostructures scatters light, absorbs light, and enhances the local electric fields [39]. Silver nanoparticles are using as antireflection coatings for solar cells due to its light trapping ability to increase the efficiency of solar cells [40, 41]. The surface plasmons of metal nanoparticles work efficiently not only for silicon based solar cells but can also be exploited for applications like silicon based photo detectors and light emitting diodes [42]. For plasmonic based solar cells, Au and Ag nanoparticles are employed because of the tunability of their surface plasmonic resonance in the Vis-NIR region. These two metals have their own advantages like Au nanoparticles do not oxidize easily under ambient conditions, while silver nanoparticles have higher scattering efficiency than Au [40, 43–45]. Furthermore silver is a potential candidate for surface enhanced Raman spectroscopy (SERS) substrate [46]. In SERS, organic

molecules of certain concentration will be drop casted on the substrate and illuminated with a light and the scattered light will be detected using detector. In this entire process, silver plasmons play a key role to enhance the signals of these organic molecules which have very low Raman scattering cross-section as such. With the aid of silver nanoparticles these adsorbed molecules will feel the additional field, which enhances the signal strength. The enhancement factor is a ratio of intensity on the metal substrate to original molecules intensity which will be multiplied by the concentration ratio used for the experiment. Besides SERS substrate, silver is a very good candidate for antimicrobial applications as silver forms a disulfide bonds lead to change in protein structure of enzymes involved in respiration of microbes which leads to their death [47, 48]. This antibacterial activity is also depends on the shape of the silver nanostructures [49]. Owing to the potential applications of silver nanostructures, it is crucial to control the shape of these nanostructures. Recently, it was reported that the surface plasmon polaritons (SPPs) excited in noble metal structures adjacent to gain media, dramatically shrink the optical mode volume and provide the necessary feedback mechanism for a surface plasmon amplification by stimulated emission of radiation (SPASER) [50]. The atomic smoothness of the metallic film is crucial for reducing the modal volume and plasmonic losses and the atomic smoothness of the metallic films is achieved via epitaxial growth. However, the synthesis of nanoparticles with uniform size and shape is difficult. Thus, large scale synthesis of nanomaterials remains a challenge.

Epitaxy means growth of a crystalline film over a crystalline substrate, where there is a registry between the film and the substrate. There are two kinds of epitaxy: one is homoepitaxy where the material of the film and the substrate are of same and the other one is heteroepitaxy where the material of the film and the substrate are different. Heteroepitaxy is one of the main synthesis technique for self-assembled nanostructures on silicon surfaces. In this growth technique, surface and interface energies and strain are the parameters which determine the thermodynamically favored growth modes. Epitaxial growth can occur in different modes depending on the surface free energies of the overlayer, the substrate and their lattice misfit. Three established growth modes are (a) Frank-van der Merwe (FM) or layer by layer [51], (b) Volmer-Weber or island [52] and Stranski Krastanov or layer-plus-island growth [53]. In general, heteroepitaxial growth can be categorized as crystal growth under stress

and usually produces a strained epitaxial layer due to lattice mismatch between the substrate and overlayer. The strained layers grow pseudomorphically upto a critical thickness beyond which a strain relaxation occurs by introducing dislocations [54].

Endotaxy is also a type of epitaxy where the crystalline film or structures grow within the substrate instead of on top of the substrate and the term *endotaxy* here refers to the growth of coherent precipitate phases in a bulk matrix, with coherent interfaces surrounding the precipitate [55]. Endotaxy is similar to allotaxy, a process in which crystals grow by annealing of implanted species [56]. Traditionally, epitaxial or endotaxial structures can be synthesized by using molecular beam epitaxy (MBE) [57] or atomic layer deposition (ALD) [58] techniques under ultra high vacuum (UHV) conditions and the order of vacuum is $\approx 10^{-10}$ mbar. The most important feature of MBE grown structures is their crystalline quality and very low impurity level which is an important requirement for microelectronic industry. In the literature there are reports about the endotaxial nanostructures synthesized by MBE technique on silicon substrate which are almost silicides of metals like Co, Ni, Fe, Ti, Pt, Dy [59–62]. Lin et. al., observed quantum transport behavior in self assembled endotaxial nickel silicide nanowires [63]. Comparing to conventional epitaxially grown nanostructures, the endotaxial structures may find it more advantageous in planar device applications as they simplify the fabrication process. These kind of embedded or endotaxial silver nanostructures maybe used in the applications in the area of plasmonics for enhancing light absorption and other opto-electronic applications. Incorporation of Ag nanostructures on the semiconductor surface and interfaces, with various shapes would also help in integrating the optical properties of Ag nanostructures with those of semiconductor properties of silicon [60, 64–66]. No reports on endotaxy of Ag or Au is reported by any method. In this thesis, first reports of endotaxial Ag or Au are reported.

Many epitaxial or endotaxial structures of various materials are grown on Si substrate under UHV conditions using MBE method. In general, silicon substrate is covered with a ~ 2 nm SiO_x layer which is called as native oxide. In order to get an epitaxial growth on silicon substrate first we have to remove or clean the oxide layer from the surface of the substrate. The cleaning of the native oxide can be done in many ways, chemical etching, thermal etching are few among them. Generally in molecular beam

epitaxy method, the oxide layer is removed by flashing the substrate at 1200 °C for few seconds [67]. In chemical etching, silicon substrate will be dipped in particular concentration of HF solution for some time to allow SiO_x to react with the HF to form SiF_4 and the silicon substrate will be passivated with hydrogen [68]. In thermal cleaning silicon substrate will be heated up to high temperatures like 900 °C to 1200 °C to remove the SiO_x layer by reacting with substrate Si atoms to form a volatile SiO layer [69–71]. In some cases thermal treatment will be followed by Argon ion bombardment to get optically plane silicon surface [72]. Piscopiello et. al, reported the growth of epitaxial gold nano islands on top of silicon substrate by depositing gold on chemically etched silicon substrate following by annealing the sample in air [25]. In this thesis, we are presenting a simple method to remove the native oxide from the Si substrate at lower temperatures in air by using an intermediate GeO_x layer at 800 °C temperature. In this mechanism, GeO_x plays a crucial role in removing the native oxide and providing a oxide free Si substrate for silver to form substrate symmetric silver nanostructures. The effect of presence and position of the GeO_x layer and annealing ambience along with annealing temperature, initial thickness of the GeO_x layer are also discussed.

This thesis is organized as follows: The principle and instrumentation of various thin film deposition methods and characterization techniques employed in this thesis work is demonstrated in chapter 2. The study of coherently embedded silver nanostructures formation and their 3-dimensional shape in the case of (100) substrate orientation is reported in chapter 3. The study of ambience dependence in the formation of these endotaxial nanostructures is the topic of chapter 4. Understanding the role of surface and interface energies in the formation of these endotaxial nanostructures through *in-situ* XRD is discussed in chapter 5. Chapter 6 outlines the thickness dependence study, where the effect of different thicknesses of GeO_x layer at the interface and also *ex-situ* temperature dependence of these structures were studied. Chapter 7 describes the growth of Ag endotaxial nanostructures in chemical vapor deposition method and the effect of deposition time on growth and the coverage of these structures and effect of growth temperature on these structures was also discussed. SERS applications of different shaped nanostructures synthesized by both PVD and CVD methods were discussed in chapter 8. The summary of the work presented in the thesis and possibility of further research in this area is given in chapter 9.

Chapter 2

Experimental Techniques

2.1 Introduction

This chapter covers the detailed explanation of the experimental techniques employed to accomplish the objectives of this thesis. The chapter begins with an introduction to thin film deposition and various types of deposition techniques that have been used in this thesis. This is followed by description of characterization techniques: scanning electron microscopy (SEM), transmission electron microscopy (TEM), scanning transmission electron microscopy (STEM), focused ion beam (FIB), synchrotron x-ray diffraction (XRD), Rutherford backscattering spectrometry (RBS) and surface enhanced Raman spectroscopy (SERS).

The metal nanostructures can be synthesized in different methods like thermal vapor deposition, where the bulk metal is subjected to resistive heating under high vacuum/ultra high vacuum conditions. Besides above methods, chemical vapor deposition (CVD) has also been used as one of the synthesis methods. Depending on the annealing ambience and substrate orientation, the silver nanostructures morphology varies. In this thesis work, depositions of silver on silicon and germania coated silicon substrates has been done using physical vapor deposition (PVD), chemical vapor deposition (CVD) methods and germania (GeO_x) deposition has been done using the PVD system. The details will be discussed in the following sections.

2.2 Thin Film Growth

Thin film growth is an essential part in modern device fabrication. It is desirable to have an ability to control morphology and structure to meet functional requirements of devices made by stacking thin film layers. Understanding of growth kinetics is, therefore, crucial in advancing the modern technology. Besides this practical purpose, it has been a challenging fundamental scientific subject and is still an active research area.

Thin film depositions can be either purely physical-like evaporative methods, or purely chemical-like gas and liquid phase chemical processes [73]. Some of the other techniques which involve glow discharge and reactive sputtering can be regarded as physical-chemical methods. In this thesis, physical *viz.* vacuum coating method and chemical *viz.* thermal CVD method will be discussed.

2.2.1 Physical Vapor Deposition Method

Thermal evaporation (physical vapor deposition) is the vaporization of a material by heating to a temperature such that the vapor pressure becomes appreciable and atoms or molecules are lost from the surface in vacuum [74]. Physical Vapor Deposition (PVD) employs the atomic vapor cloud formed by the vaporization of material in a vacuum environment to cover all the surfaces. It involves the following sequential steps:

- (i) Conversion of deposited material into vapor by heating,
- (ii) Transportation of material from source to the target substrate
- (iii) Condensation of the vapor on the substrate and formation of thin film.

Heating of the materials in PVD system can be done in several ways. The simplest one is the resistive heating, where a boat of tungsten or molybdenum is resistively heated (by passing 200 A current at 10 V voltage), so that the material being in thermal contact to the boat, due to thermal energy I^2R (which has been possible due to Joule's heating) the material melts and evaporates (sublimation can occur as well). In electron beam evaporation, a beam of electrons is made to focus at the material,

thus heating up and evaporation from tiny localized area of the material occurs. This is done in a high vacuum (generally 5×10^{-5} to 1×10^{-6} mbar) to allow the vapor to reach the substrate without reacting with other gas-phase atoms in the chamber or to increase the mean free path of the vapors to reduce the incorporation of impurities from the residual gas in the chamber. Obviously, only materials with a much higher vapor pressure than the heating element can be deposited without contamination of the film. The principal requirement for successful thin film growth using this process is that the mean free path of the depositing material atoms must be greater than the distance between the source and substrate [75].

In this thesis work, thermal evaporation technique is employed to deposit germanium and silver. Various thicknesses of Ge (or GeO_x) and 2 nm silver were deposited using high vacuum coating unit. Germanium (GeO_x) was deposited using a molybdenum basket whereas silver was deposited using a tungsten boat. Large current was passed through this boat/basket to heat up the material to melt and evaporate for deposition. The coating unit consists of a cylindrical, stainless steel vacuum chamber, approximately 55 cm tall and 40 cm in diameter. This chamber is connected to double stage pumping system: 250 liter per min rotary pump and 280 liter per second oil diffusion pump. Pirani and Penning gauges are used to monitor the vacuum level during deposition. Thickness of the film is measured using a thickness monitor with a quartz crystal microbalance. The quartz crystal mechanically oscillates when ac voltage is applied to it (piezoelectric effect) [76]. The resonance frequency of oscillations is dependent on the mass of the film deposited onto it. Quartz thickness monitors can measure thickness of about a single atomic layer with relatively high accuracy. The calibration of quartz thickness monitor is routinely done with Rutherford backscattering (RBS) measurements. Effective thickness values are obtained by using RBS and cross-sectional TEM measurements.

2.2.2 Chemical Vapor Deposition

Chemical vapor deposition involves the formation of a thin solid film on a substrate material by a chemical reaction of vapor phase precursors. It can thus be distinguished from physical vapor deposition processes such as evaporation and reactive

sputtering which involve the adsorption of atomic or molecular species on the substrate. The chemical reactions of precursors species occur both in the gas phase and on the substrate. Reactions can be promoted by heat (thermal CVD), higher frequency radiations such as UV (Photo assisted CVD) or plasma (plasma enhanced CVD).

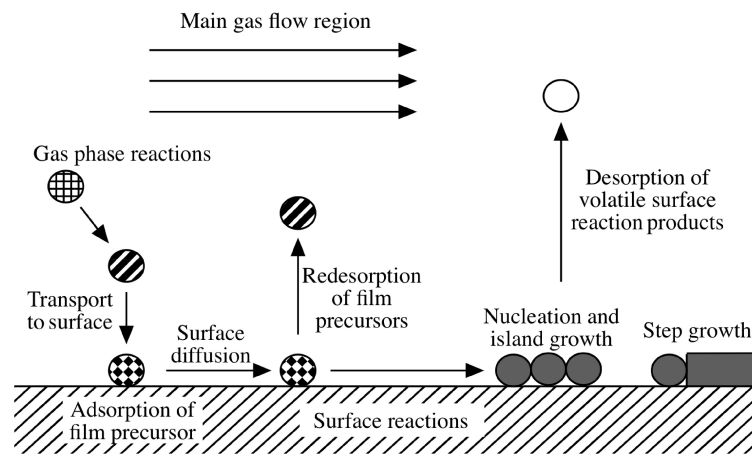


Figure 2.1: A schematic diagram of precursor transport and reaction process in CVD [77]

A more detailed picture of the basic physiochemical steps in an overall CVD reaction is illustrated in the figure 2.1, which indicates several key steps:

1. Evaporation and transport of reagents (i.e. precursors) in the bulk gas flow region into the reactor;
2. Gas phase reaction of precursors in the reaction zone to produce reactive intermediates and gaseous by-products;
3. Mass transport of reactants to the substrate surface;
4. Adsorption of the reactants on the substrate surface;
5. Surface diffusion to growth sites, nucleation and surface chemical reactions leading to film;
6. Desorption and mass transport of remaining fragments of the decomposition away from the reaction zone.

In traditional thermal CVD, growth rate depends on several parameters, such as,

temperature of the substrate, operating pressure and the composition and chemistry of the gas phase. The growth rate in kinetic growth control region is follows Arrhenius equation:

$$\text{Growth rate} \propto e^{(-E_a/RT)} \quad (2.1)$$

where E_a is activation energy, T is temperature in Kelvin and R is universal gas constant.

Precursor requirements

The characteristics of an ideal CVD precursor can be summarized as follows [77]:

1. Adequate volatility to achieve acceptable growth rates at moderate evaporation temperatures.
2. Stability so that decomposition does not occur during evaporation.
3. A sufficiently large temperature window between evaporation and decomposition for film deposition.
4. High chemical purity.
5. Clean decomposition without the incorporation of residual impurities.
6. Good compatibility with co-precursors during the growth of complex materials.
7. Long shelf-life with indefinite stability under ambient conditions.
8. Readily manufactured in high yield at low cost.
9. Non-hazardous or with a low hazard risk.

These requirements are common for most CVD precursors, sometimes the requirements of the precursors depends on the specific nature of the CVD process. For example, in a traditional CVD process, it is important that the precursor shouldn't degrade its quality or react with oxygen and water vapor in the atmosphere. This is a major disadvantage, though, in atomic layer deposition (ALD) method, as it is essential that the surface exchange reaction with [OH] is facile, otherwise very low growth rates would result.

2.2.3 Low Vacuum Annealing Setup

The indigenously built low vacuum annealing setup used for this work is a horizontal tube furnace with a quartz tube with the length of the quartz tube being 88 cm and its diameter being 5 cm. The maximum temperature it can go up to 1400 °C with minimum ramping rate of 1 °C/min to a value of 10 °C/min as the upper limit. SiC rods are used as the heating elements in this setup. The temperature is controlled by the temperature controller (Honeywell DC-1040) with programmable and automatic control. The heating zone inside the tube is about 15 cm. The same unit is used for the study of ambient dependence by connecting one end of the quartz tube to the oxygen or argon gas flow or rotary pump for low vacuum.

2.3 Characterization techniques

Characterization of the samples was done using transmission electron microscope (TEM), scanning transmission electron microscopy along with its energy dispersive X-ray spectroscopy and 3D tomography. Scanning electron microscopy was used to observe the morphology of the samples, along with SEM-focused ion beam is used to prepare cross-sectional TEM specimen besides conventional method of thinning and ion polishing procedures. Synchrotron X-ray diffraction (XRD) is used to check crystallinity of the samples and for the study of real time growth kinetics and Rutherford back scattering (RBS) experiments are used to check the composition and thickness. A brief introduction to Raman spectroscopy and surface enhanced Raman spectroscopy (SERS) are discussed towards the end of this chapter. All the above tools are discussed briefly in the following sections.

2.3.1 Transmission Electron Microscopy

In the advancement of materials science and engineering, it is necessary to observe, analyze and understand the phenomena occurring at the nano-scale regime. The transmission electron microscope (TEM) is a powerful and versatile instrument which permits characterization of materials [78–80]. It offers variety of information obtained from different modes such as bright field (BF) and dark field (DF) imaging, selected

area diffraction (SAD) and high resolution TEM (HRTEM). BF and DF imaging are used to characterize defects and domain structures. SAD with combination of tilting of crystal in the microscope allows reconstructing the reciprocal space and is used to obtain information about the crystal structure and identifying different phases. The first TEM was built by two German scientists, M. Knoll and E. Ruska, in 1932 [81]. Nowadays, TEMs have become widely available.

In a TEM, a high-energy ($\sim 200\text{-}300$ keV) electron beam and its interaction with the specimen is used for imaging at atomic scale. To get an insight of crystallographic information available using TEM, both imaging and diffraction modes are used regularly. For direct information of defect structure on the atomic scale, an HRTEM is particularly useful with low spherical aberration coefficient (or with aberration correction), given that this is the typical spacing between atoms in solids [79]. In selected area diffraction pattern (SAED), the sample is illuminated with a parallel beam of electrons to ensure the focusing of the transmitted and diffracted beam onto the back focal plane of the objective lens. A specific area of the sample is selected by an SAED aperture that is in an *image plane* conjugate with the sample in the electron optic system of the TEM. The inserted SAED aperture creates a virtual aperture in the sample plane, giving a selected area that is selected by available aperture values [78]. A few hundred nanometers is often the typical lateral size of the region sampled by SAED in conventional older TEM systems.

Instrumentation

A transmission electron microscope consists of an illumination system, specimen stage and imaging system similar to a conventional optical microscope. An electrostatic lens in the form of Wehnelt cap is used after the filament to converge the maximum number of emitted electrons. Illumination section consists of electron source, acceleration column and condenser lenses. The role of the illumination system in TEM is to project an electron beam on the part of the specimen that is observed. In this thesis, most of the TEM measurements have been carried out using JEOL 2010 TEM operating at 200 keV with LaB₆ thermionic emission gun. Here, high voltage is generated in a separated power supply unit using Cockcroft-Walton technique and is coupled with the accelerating column. Following the acceleration column, condenser lens system

is situated. Electrons are generated in the electron gun by thermionic emission. In a thermionic system, filament material is heated to a high enough temperature, such that, it will emit electrons when they have enough energy to overcome the work function (ϕ) according to $J = AT^2 e^{-\frac{\phi}{k_B T}}$, (where J is the current density at the tip, A is the Richardson's constant and k_B is Boltzmann constant). After leaving the electron gun the electrons are accelerated towards the anode and enter the column. Since the velocity of the electrons is close to the speed of light at an energy of 200-300 keV, the wavelength of the electrons has to be corrected for relativistic effects:

$$\lambda = \frac{h}{\sqrt{2m_0 eV(1 + \frac{eV}{2m_0 c^2})}} \quad (2.2)$$

It is to be noted that, corresponding relativistically corrected wavelength λ for 200 keV electrons is ≈ 0.0025 nm. Electrons are accelerated towards the anode at the top of the column and focus at the specimen with the help of condenser lenses. The function of the condenser lens system is to provide a parallel or convergent beam of electrons at the specimen. In practice, a complete parallel beam is not possible and the beam always possesses a certain kind of convergence when imaging at high resolution, usually in the range of ≈ 1 mrad for LaB_6 emitters. Using different size of condenser aperture, illuminated area of the specimen can be changed. Objective lens (OL) is located below the specimen. The combination of intermediate and projector lenses are used to obtain the desired image magnification. After the objective lens, objective aperture and selected area diffraction aperture are placed (shown in Figure 2.2). Finally the magnified image forms at phosphor screen. To record the image or diffraction pattern, photographic film and/or charge coupled device (CCD) can be used. The light generated on the phosphor screen is channeled to the CCD through the optical fiber and the CCD output is connected to the computer using image processing system. As electron is very highly interacting particle, the vacuum maintained inside the column of TEM, is $\approx 10^{-8}$ mbar. Among the others, three parameters are important for the best TEM imaging: the brightness, source size and energy spread of the electrons. The brightness is defined as the current density per solid angle. Accelerating the electrons results in a less diverging beam and increases the brightness. The source size is the area from where the electrons seem to originate. Due to some electron-optic effects the source size is not always equal to the actual emitting area on the tip but a cross-over size after the whenlet is referred as the virtual source size. High resolution TEM requires a planar coherent electron wave, since high-resolution

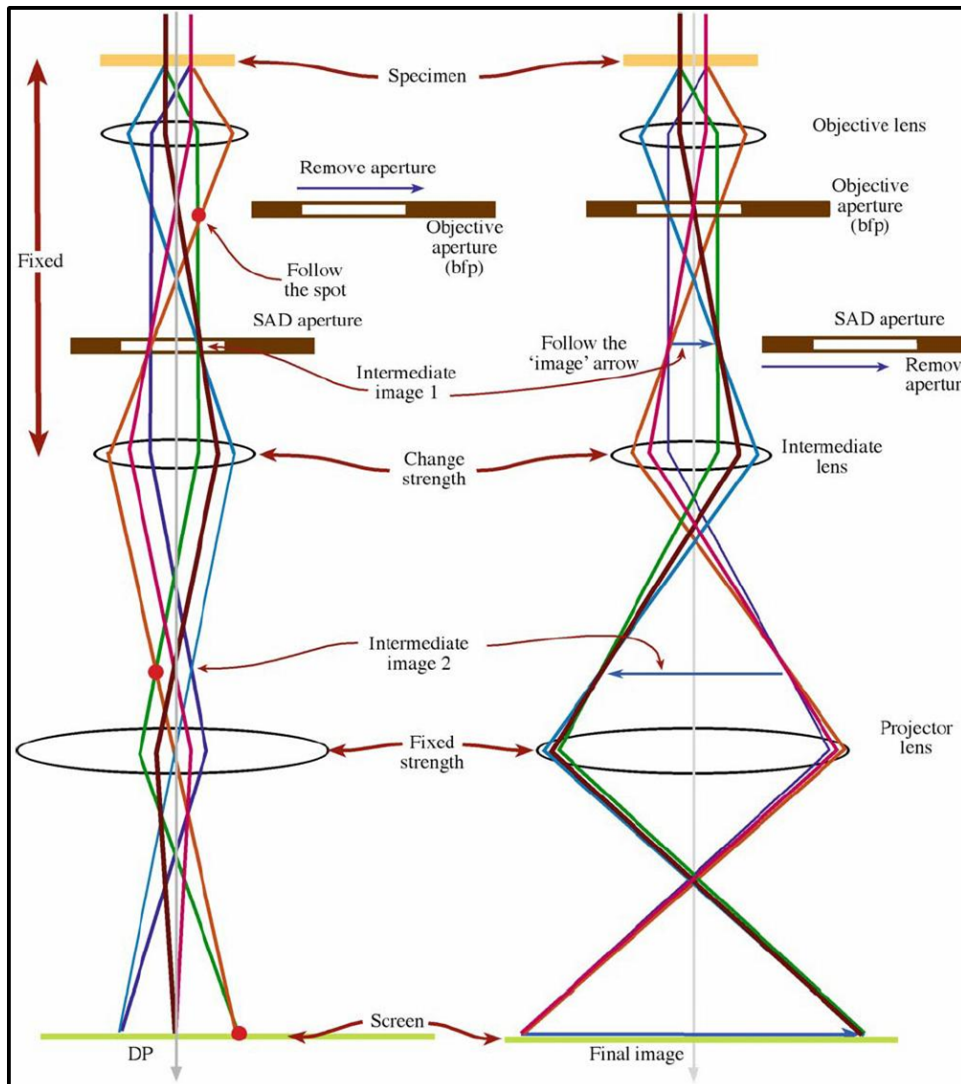


Figure 2.2: A schematic diagram of Diffraction pattern (DP) formation and Image formation [78].

images are formed by phase contrast.

Interaction of electrons with the specimen

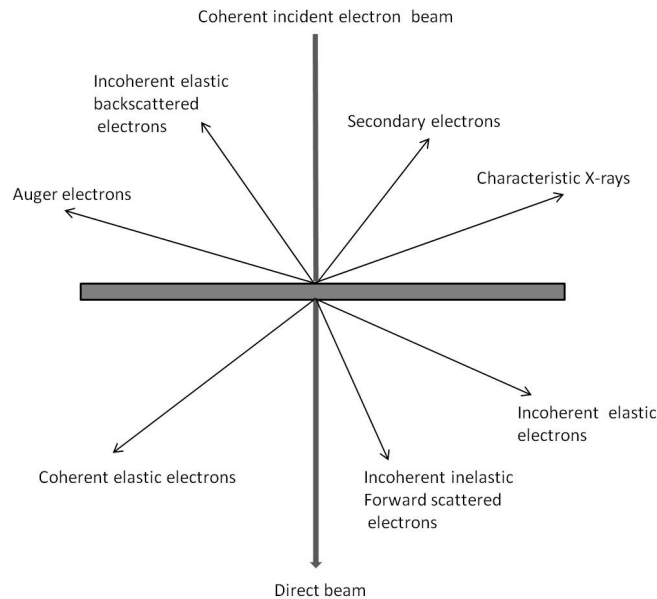


Figure 2.3: A schematic diagram of different processes taking place during electron-solid interaction.

After entering the specimen, most of the electrons are elastically scattered by the nuclei of the atoms in the specimen. Some electrons are inelastically scattered by the electrons in the specimen (figure 2.3). Compared to X-ray or neutron diffraction, the interaction of electrons with the specimen is very high and multiple scattering events dominates unless a very thin specimen is used. For thick specimen at lower resolutions, an incoherent particle model can describe the interaction of the electrons with the specimen. However, with thin specimens at high resolution, this description fails because the wave character of the electrons needed to be invoked. The electrons passing the specimen near the nuclei are somewhat accelerated towards the nuclei causing small, local reductions in wavelength, resulting in a small phase change of the electrons. Information about the specimen structure is therefore transferred to the phase of the electrons. For the formation of high resolution images, only the elastically scattered electrons are of importance. The inelastically scattered electrons contribute mostly to the background of the image. The energy loss spectrum of the

inelastic scattered electrons contains valuable information about the chemical composition of the specimen. This information can be extracted by analyzing the electron energy loss spectrum (EELS). The inelastic scattered electrons also produce Kikuchi lines in the electron diffraction pattern that is helpful for accurate crystallographic alignment of the crystals in the specimen.

Imaging and Diffraction

The conventional TEM image formation for thicker specimen is very similar to the projector principle. In this case, an incoherent particle model can describe the interaction of the electrons with the specimen. Specimen contains variation in thickness and density. So, the electrons will lose more energy when they transmit through the thicker and denser region and hence it will appear as darker object. Same way, the thinner region will appear as brighter object. This contrast in imaging mode arises due to variation of thickness and is referred as mass-thickness contrast. In *diffraction contrast*, contrast depends up on the crystallinity of the specimen. However, for thin specimen at high resolution, this description fails because the wave nature of the electrons is then needs to be invoked. If the specimen is thin enough and crystalline, then elastic scattering is usually coherent and these scattered/transmitted electrons are contribute to the image formation. After the exit of electrons (elastically transmitted coherent electron beams), the diffraction spots and image are used to form at back-focal plane and image plane of objective lens (OL), respectively. The diffraction pattern can be understood by taking the fast fourier transform (FFT) of the wave function of electron at the back focal plane of OL. The lattice image will form due to interference between the direct and diffracted beams depending on the phase difference between these two. So the highly diffracted beams are used to cut down by the objective aperture. The resolution and the details of image formation are governed by the contrast transfer function (CTF).

To retrieve structural information of the specimen from the micrograph it is necessary to calculate the trajectory of the electron wave through the specimen. In the kinematical approximation, multiple scattering of the electrons in the sample is ignored resulting in an undisturbed central beam. This approach already fails at a small thickness or a single atom. In dynamical calculations all the scattered beams

and their mutual exchange of intensity during the course of multiple scattering in the specimen are taken into account. It is possible to do full dynamical calculations but these are soon limited by the available computing power. Using the fact that the vast majority of the electrons are scattered in a forward direction with small diffraction angles Cowley and Moodie devised the multislice approximation [82].

In this thesis work, two kinds of TEM systems have been used. Majority of HRTEM has been carried out using JEOL 2010 TEM operating at 200 keV (Fig. 2.4) at IOP, Bhubaneswar. This machine is equipped with an ultra high resolution pole piece (UHR-URP22) (spherical aberration coefficient (C_s) of 0.5 mm) and can have a point-to-point resolution of 0.19 nm. For recording images and diffraction patterns charge coupled-device (CCD) based detector with 4008×2672 pixels (Model 832, Gatan Inc.) has been used. In this thesis work, STEM, EDS and 3D tomography were carried out with a 300 keV electrons in the C_s -corrected FEI Titan 80/300 system at the University of Bremen, Bremen, Germany. A probe diameter of 0.2 nm was used during HAADF and STEM-BF measurements.

Sample preparation

Sample preparation is one of the important aspect, where a lot of care needs to be taken for carrying out good TEM measurements. As the electrons transmit through the specimen, the specimen has to be thin enough to allow the electrons to pass through the sample. For conventional TEM, thickness needs to ≈ 100 nm and even lesser thickness (< 10 nm) for HRTEM imaging. Two types of samples are prepared depending on the interest of study: Cross-sectional TEM (XTEM) sample (required to probe the interface and/or bulk solid), and planar TEM specimen preparation (probe the surface morphology).

Figure 2.5 and 2.6 show the schematic diagrams for preparing both planar and cross sectional TEM sample preparation respectively along with the photographs of instruments that are used for respective part of specimen preparation.

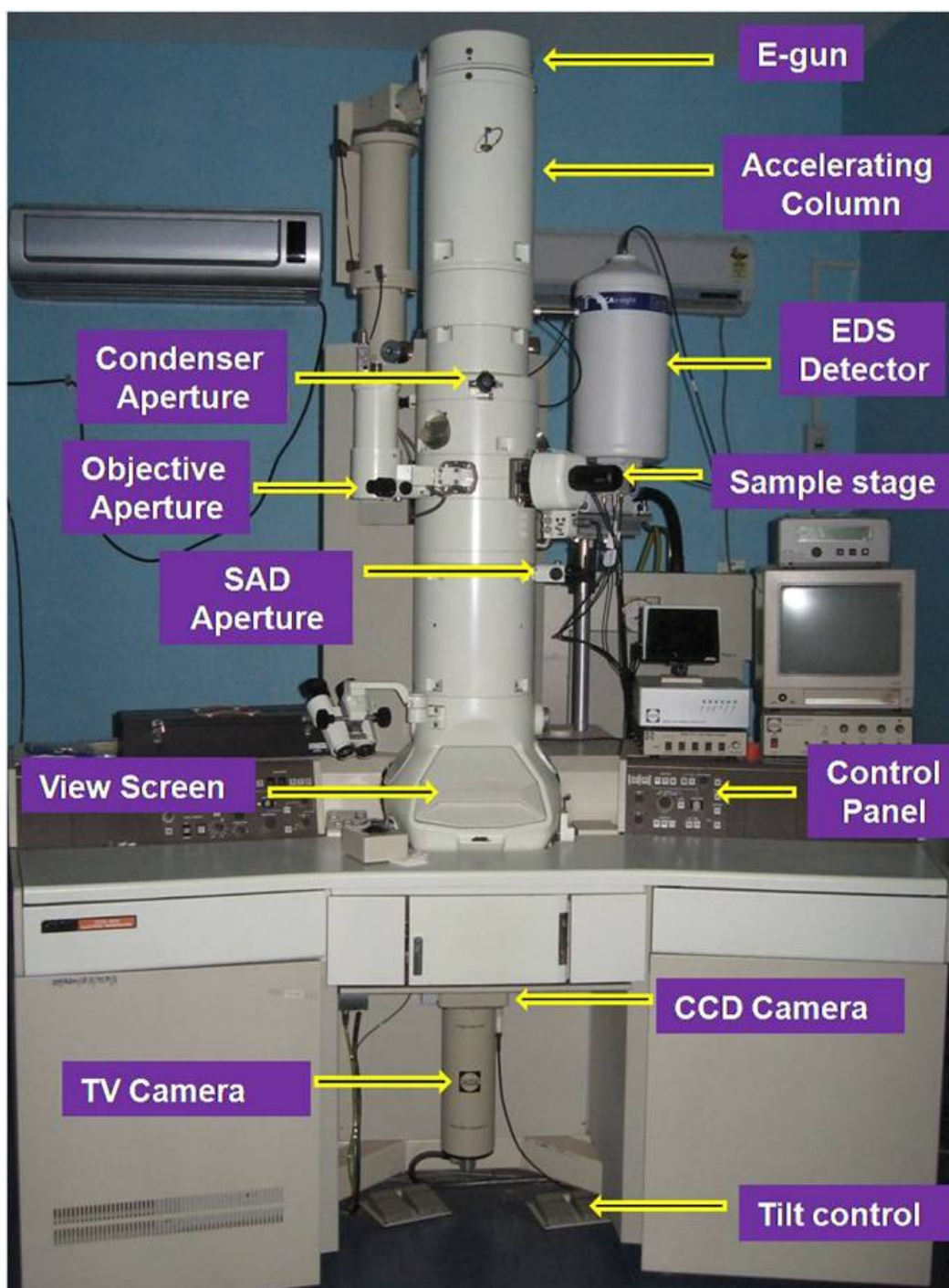


Figure 2.4: 200 keV JEOL HRTEM installed at Institute of Physics, Bhubaneswar.

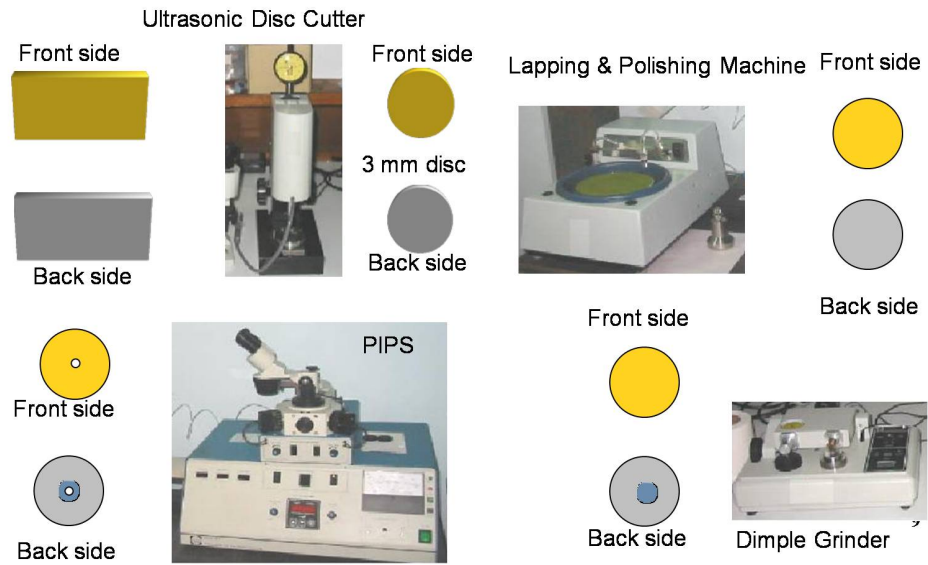


Figure 2.5: A schematic diagram of procedure to prepare a typical planar TEM specimen.

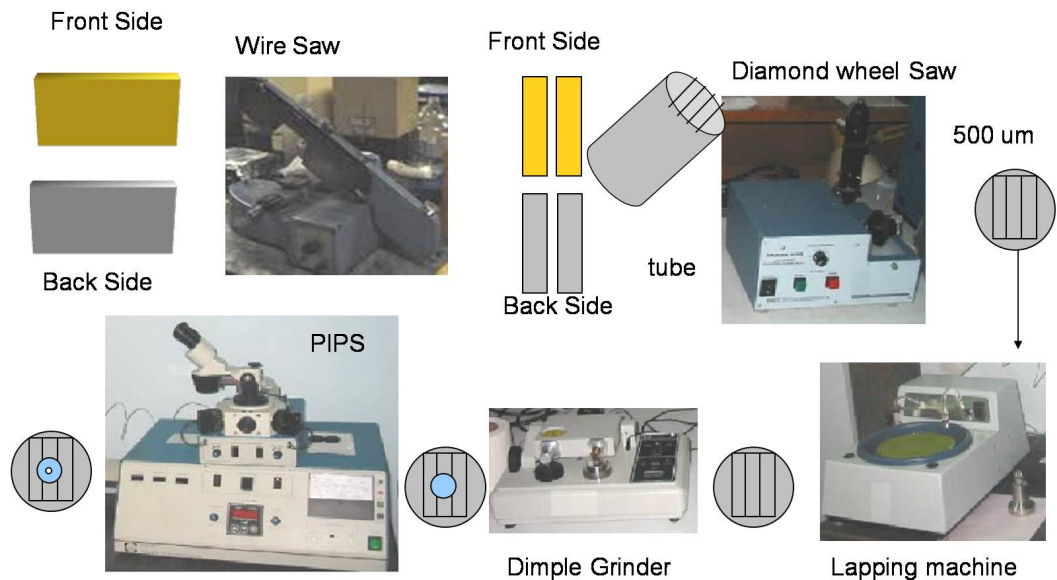


Figure 2.6: A schematic diagram of procedure to prepare a typical cross-sectional TEM specimen.

Planar specimen

For Planar TEM sample preparation, a 3 mm disc was cut from the desired substrate using ultrasonic disc cutter and thin down to $\sim 100 \mu\text{m}$ using the lapping and polishing system. Here, the mechanical thinning starts with a larger grit size and finished with finer grit size. Then the specimen is dimpled to lower the thickness at the center (down to 30-40 μm) and polished using dimple grinder (DG) system (model 656, Gatan, USA). In this process, the edge remains thicker but center part becomes thinner. Electron transparency of this dimpled sample is achieved by ion milling using precision ion polishing system (PIPS) (model 691, Gatan, USA). During ion milling process, a 3.0 keV Ar ion beam is used to sputter the material from the specimen in grazing incidence (4° - 7°) (Fig. 2.5). A Gentle mill ion milling system (Technoorg Linda) is also used for further thinning with much lower energies (200-400 eV Ar ions).

Cross-sectional specimen

For Cross-sectional TEM sample preparation, two rectangular pieces of size (2.5×3) mm^2 each were cut from the desired sample using abrasive slurry wire saw (model 850, SBT). These pieces were pasted face to face using epoxy (G1 epoxy, Gatan, USA) as close as possible. It will ensure an optimal ion milling rate i.e. if the glue quantity will be too high, the ion mill will remove it quicker than the sample resulting a sharp hole with a sharp edge, opaque to electron beam, so care is taken to have enough material. Following this, the sample is inserted into a stainless steel tube having inner and outer diameter 2.5 mm and 3 mm respectively. After setting in, a 1 mm slice is made using low speed diamond wheel saw (model 650, SBT). The slice is thinned mechanically (by lapping and dimpling) followed by 3.0 keV Ar ion milling to achieve the electron transparency. The procedure for thinning XTEM sample is also like planar specimen but in this case one needs to do the lapping from both sides and dimpling for one side. The procedure of cross-sectional specimen is pictorially explained in Figure 2.6, along with the instruments used for the same. Mechanical thinning of the sample from both sides followed by dimpling on one side will be taken to the PIPS to obtain the electron transparency.

2.3.2 FIB-SEM-Cross beam system

The combination of field emission scanning electron microscope (FESEM) and focused ion beam (FIB) is an important system that can be used for semiconductor and material science related applications. A scanning electron microscope (SEM) uses an electron beam to form an image instead of light as compared to a compound microscope. Since their development in the early 1950's, scanning electron microscopes have been used in many areas of study in the medical and physical science communities. The focused ion beam (FIB) technique was mainly developed during the late 1970's and the early 1980's. Modern FIB systems are becoming widely available in semiconductor research and processing environments, as well as in failure analysis and chip-design centers. The technology enables localized milling and site specific deposition of conductors and insulators with high precision. Hence it is widely used in device modification, mask repair, process control and failure analysis and also the preparation of specimens for transmission electron microscopy (TEM).

In thesis work, the cross-beam system with components: scanning electron microscope (SEM, Gemini Column, Carl Zeiss, Neon 40), focused ion beam (FIB, Orsay Physics), gas injection system (GIS, Orsay Physics), STEM detector, four quadrant back scattered electron detector (Carl Zeiss) and EDS detector (INCA, Oxford) [figure 2.7] has been used. The two beams (electron and Ga ion beams) are focused on the same point of the sample. Both beams coincide at a crossover point 5 mm below the objective lens of the SEM. The working distance (WD) for the FIB in this coincidence point is ≈ 12 mm. The geometrical layout and arrangement of the two columns enables perpendicular tilt of the sample to the ion beam in the coincidence point. To provide full eucentric tilt at all operating conditions, a 6-axis motorized eucentric specimen stage is used. This allows real time simultaneous FIB machining and non-destructive non-contaminating SEM imaging at high resolution. The sample can be tilted between 0° and 54° to face perpendicularly the ion or the electron beam. At 0° tilt, imaging at normal incidence with the electron beam is possible while at 54° , imaging and machining with the FIB is generally performed. Both imaging techniques are based on the collection of secondary electrons. The FIB column operates at an accelerating voltage ranging from 2 to 30 kV with a minimal Gaussian beam diameter ≈ 7 nm. The beam current can be varied from 1 pA to 50 nA. The FIB system can be used for imaging, milling and deposition (using GIS). One micromanipulator

(Kleindiek) is attached inside the specimen chamber for TEM lamella preparation (for lift out). The system is equipped with a computer controlled gas injection system that can offer up to five different gases for metal and insulator deposition or enhanced and selective etching. The GIS is composed of five independent channels for gas injection. Gas flows from a reservoir through a capillary. Temperature of reservoirs and capillaries are independently controlled. The needles at the end of the capillaries are mounted on a micro stage table. Thus they can be precisely positioned close to the working area ($< 100 \mu\text{m}$) in order to create a local high gas pressure. A turbo molecular pump ensures a dynamic pumping and maintain the base pressure in the chamber (10^{-6} mbar). The cross beam system can also be used for both e-beam and ion beam lithography (ELPHY Quantum lithography system, Raith).

In the following section, the working principle of SEM and FIB will be discussed individually.

Scanning Electron Microscopy (SEM)

The SEM consists a field emission gun, GEMINI electron-optics, a lateral secondary electron (SE) detector (*Everhart-Thornley*), a backscatter detector and an in-lens SE detector. The main characteristic of the electron optics is the use of a booster voltage and an objective lens which acts as a combined electrostatic/electromagnetic lens. The electrons generated at the gun tip are accelerated to the set acceleration voltage. However, the booster voltage, which is installed directly after anode, is always at a potential of an extra 8 kV when the set acceleration voltage is ≤ 20 kV. When low voltages are used, this arrangement will ensure that the energy of the electrons in the beam path will always be 8 kV higher than the set acceleration voltage and will reduce the influence of magnetic stray fields on the electron beam. Before the electron beam exits the objective lens, the electrostatic lens reduces the potential by an opposite 8 kV field. The main advantage of this technique is that a stable beam is obtained even at low acceleration voltages. In addition to acting as a retardant voltage towards the electrons ejected from the electron column, the electrostatic lens will act as a collector for the electrons generated at the sample surface. The sample electrons are accelerated and focused back up the beam path, where the in-lens SE detector is positioned (annular detector). The combination of the electrostatic lens

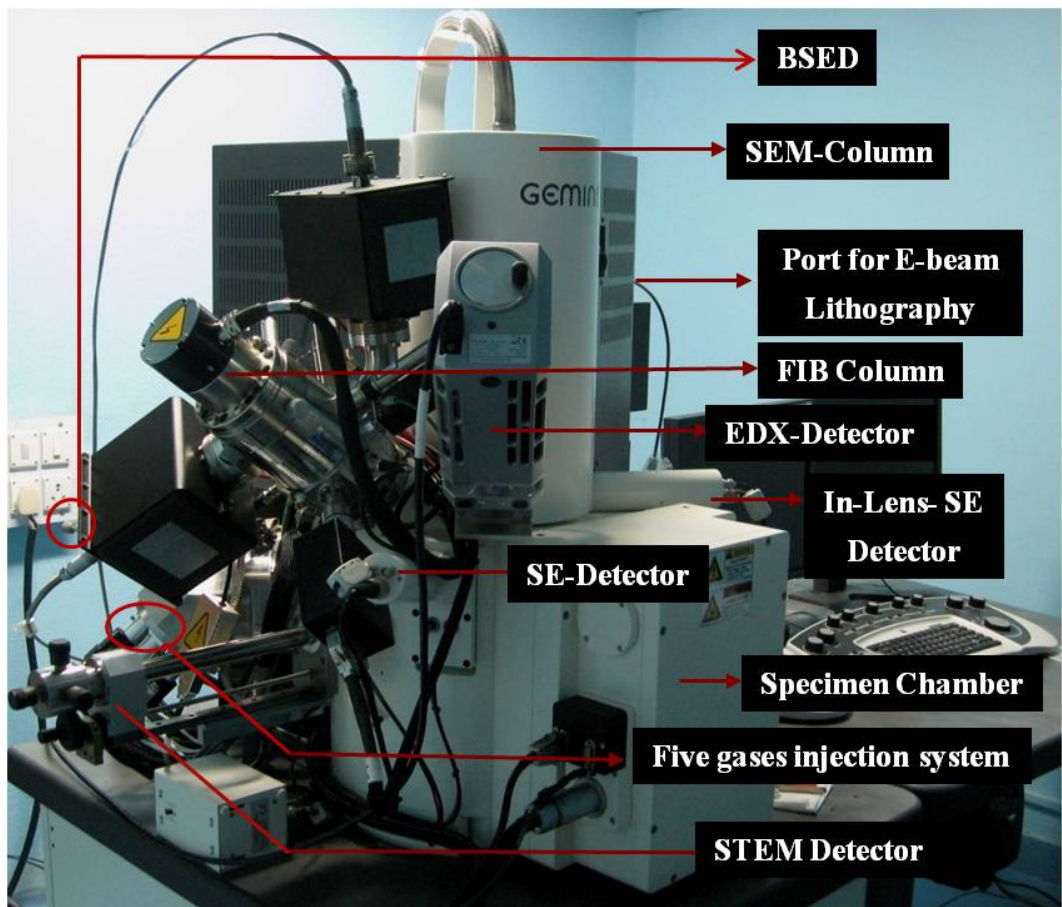


Figure 2.7: FIB-SEM crossbeam system installed at Institute of Physics, Bhubaneswar.

and the in-lens detector results in a very high detection efficiency for the in-lens detector even at low (< 1 kV) acceleration voltages [83].

Image Formation

SEM image formation depends on the secondary electron emission of surfaces bombarded by primary electrons. The energy distribution, the angular distribution and the yield of secondary electrons from materials and the escape depth of secondary electrons is dependent on the interaction of electrons with specimen [84]. These interactions can be divided into two major categories: elastic interactions and inelastic interactions. Elastic scattering results from the deflection of the incident electron by the specimen atomic nuclei or by outer shell electrons of similar energy. This kind of interaction is characterized by negligible energy loss during the collision and by a directional change of the scattered electrons. Incident electrons that are elastically scattered through an angle of more than 90° are called backscattered electrons (BSE), and yield a useful signal for imaging the sample. Inelastic scattering occurs through a variety of interactions between the incident electrons and the electrons and atoms of the sample, and results in the primary beam electrons transferring substantial amount of energy to that atom. The amount of energy loss depends on whether the specimen electrons are excited singly or collectively and on the binding energy of the electron to the atom. As a result, the excitation of the specimen electrons during the ionization of specimen atoms leads to the generation of secondary electrons (SE). In addition to those signals that are utilized to form an image, a number of other signals are produced when an electron beam incident on a sample, such as x-ray emission, Auger electrons and cathodoluminescence (figure 2.8). Basically, when primary electrons impinge on the sample, the primary electrons cause either secondary electrons (SE's) or backscattered (BSE's) to be emitted from the sample. These are used for image formation in SEM. As a result of inelastic interactions of the primary electrons with the sample, the secondary electrons are emitted from the sample with energy less than ≈ 50 eV [85]. The energy distribution of the backscattered electrons has a peak just below the primary electron energy and a tail towards zero. As the secondary electrons are lower in energy than the backscattered electrons, they can be isolated from the high energy backscattered electrons with an electric field. Because of the low energy of the secondary electrons, the only electrons that come from the

topmost layers of the sample can be detected. due to this, surface morphology can easily be studied using SEM. The higher energy backscattered electrons can escape from deeper in the sample. The number of backscattered electrons depends on the atomic number of the sample. Hence, a backscatter electron image gives information about the composition of the sample.

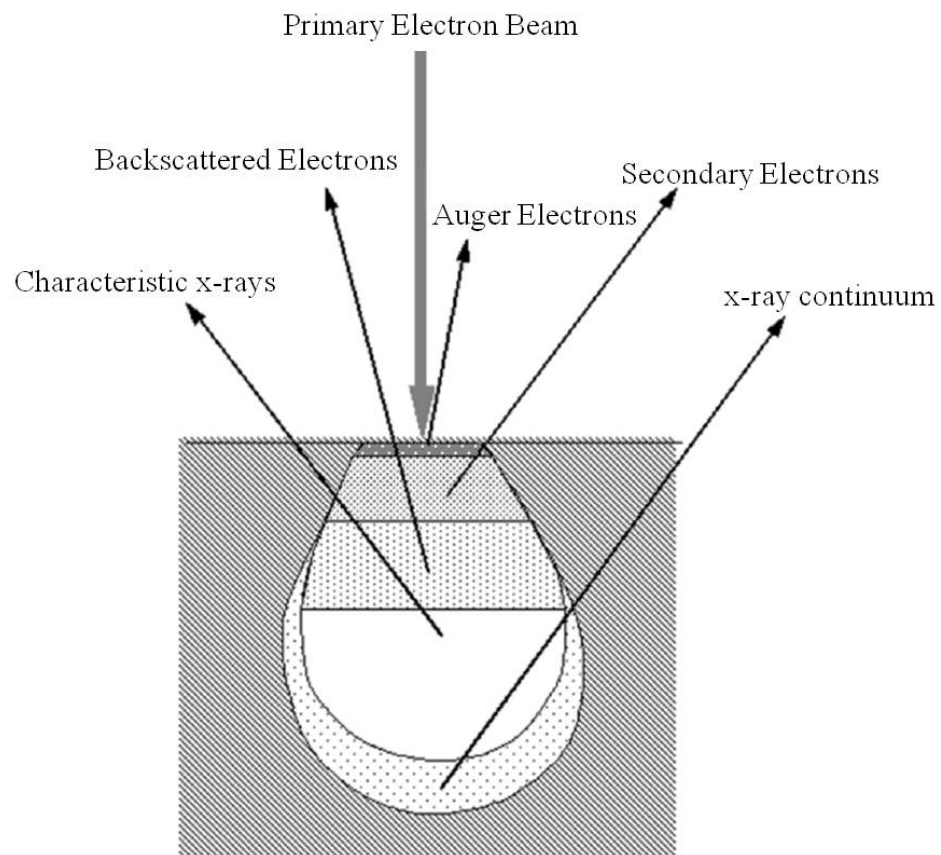


Figure 2.8: A schematic diagram of different processes taking place during electron–solid interaction

Most commonly an *Everhart-Thornley* detector (E-T detector) is used to detect the electron signals in the scanning electron microscope for high resolution images. The E-T detector consists of a Faraday cage covering a scintillator, a light guide and a photomultiplier. The Faraday cage is placed outside the detector and either a negative or a positive bias voltage can be applied to it. When a negative bias voltage is applied, all secondary electrons are repelled and hence only the backscatter electron signal is detected. When a positive bias voltage is applied to the Faraday cage, the secondary

electrons are attracted to the detector. The positive bias voltage causes the trajectory of electrons emitted from the sample over a large solid angle to be deviated towards the detector. In the detector, the electrons are accelerated to the scintillator where they induce light emission. The light is guided to the photomultiplier tube to amplify the signal and converting it into an electric current which can be read out on a screen.

Focused Ion Beam (FIB)

The design of the column is similar to that of a scanning electron microscope, the major difference being the use of a gallium ion (Ga^+) beam instead of an electron beam. A vacuum of $\approx 1 \times 10^{-7}$ mbar is maintained inside the column. The basic components of a FIB system consists of an ion source, acceleration/ion optics column, a beam deflector and a substrate stage. The ion beam is generated from a *liquid-metal ion source* (LMIS) by the application of a strong electric field. This electric field causes the emission of positively charged ions from a liquid gallium cone, which is formed on the tip of a tungsten needle, the typical extraction voltage used for this is ≈ 7 kV. After a first refinement through the aperture, the ion beam is condensed in the first electrostatic lens. The upper *octopole* then adjusts the stigmation of the beam. The ion beam energy is typically between 2 keV and 30 keV, with beam currents varying from 1 pA to 50 nA. Using the variable aperture mechanism, the beam current can be varied, allowing both a fine beam for high-resolution imaging on sensitive samples and a heavy beam for fast and rough milling. Blanking of the beam is accomplished by the blanking deflector and aperture, while the lower *octopole* is used for raster scanning of the beam over the sample in a user-defined pattern. In the second electrostatic lens, the beam is focused to a fine spot, enabling a best resolution in the sub 10 nm range. All operations such as manipulating the stage, controlling valves for gas delivery, turning on and off pumps and manipulating the ion beam are carried out via software. A system of vacuum pumps (combination of Turbo with rotary) is used to maintain the vacuum inside the column and the work chamber. The ion column is additionally provided with one or two ion pumps.

2.3.3 Scanning Transmission Electron Microscopy (STEM)

In STEM, process of the image formation is different compared to the conventional TEM. The electron beam is sharply focused onto the specimen plane with a diameter in the sub-nanometer range. The signal on the (ring-shaped) high angle annular dark field (HAADF) detector comes from electrons scattered to large angles well above 30 mrad. Local information is finally retrieved by mapping the HAADF signal against the position of the probe. Therefore, the probe is rastered over the specimen to get the local information. Atomic resolution images, diffraction patterns from nanometer regions and nanometer scale spectroscopy data can be obtained either simultaneously or sequentially from the same region of the specimen in the STEM which is the virtue of it. [86,87].

High Angle Annular Dark Field Imaging (HAADF)

The HAADF detector is an annulus of scintillator material coupled to a photomultiplier tube in a way similar to the BF (bright field) detector. It therefore measures the total electron signal scattered in angle between an inner and an outer radii. These radii can both vary over a large range, but typically the inner radius would be in the range of 30–100 mrad and the outer radius 100–200 mrad. As the scattering angle increases, the scattered intensity from an atom approaches the Z^2 dependence that would be expected for Rutherford scattering from an unscreened Coulomb potential. Hence the contrast depends on $\approx Z$ of the material. So, HAADF imaging is also called *z-contrast imaging*. In practice, this limit is not reached and the Z exponent falls to values typically around 1.7 [89] due to the screening effect of the core electrons. This sensitivity to atomic number results in images in which composition changes are more strongly visible in the image contrast than would be the case for high-resolution phase-contrast imaging. Often the center of the detector is a hole, and electrons below the inner radius can pass through the detector for use either to form a BF image, or more commonly to be energy analyzed to form an electron energy-loss spectrum (figure 2.9). An energy dispersive x-ray spectrometer is usually used to get a compositional mapping with sub-nm resolution.

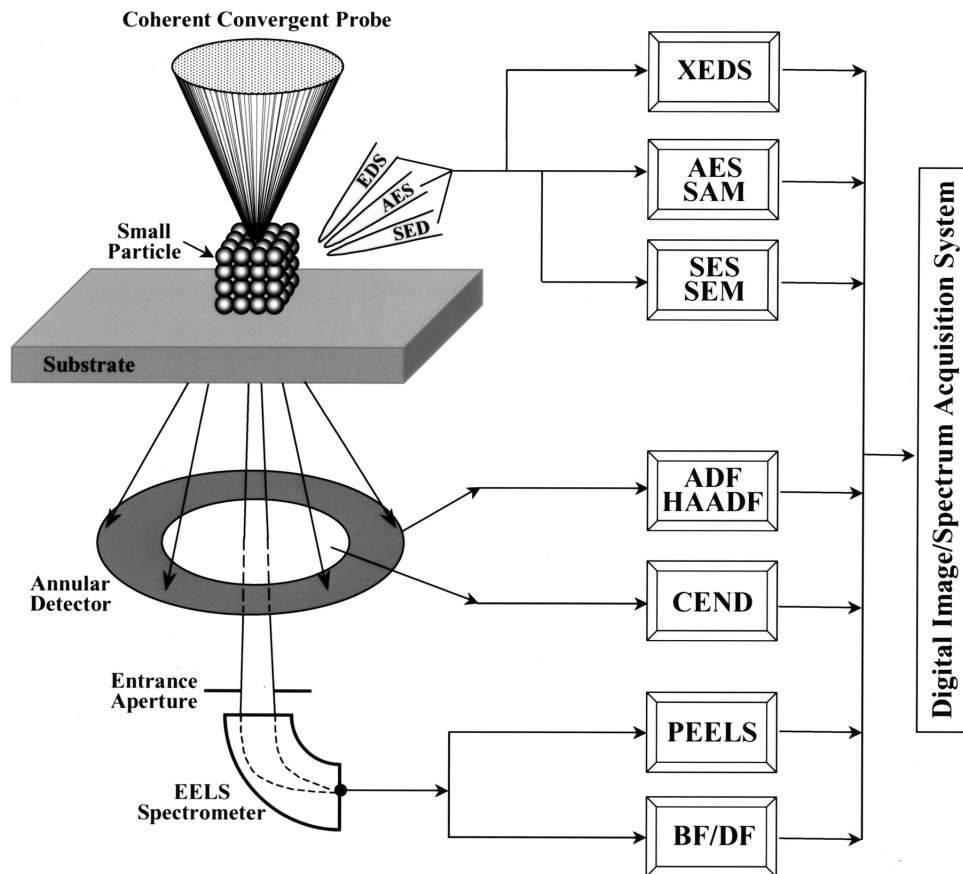


Figure 2.9: Schematic diagram illustrates the various signals generated inside a scanning transmission electron microscope that can be used to form high-resolution images, nanodiffraction patterns or spectra of the region-of-interest. X-ray energy dispersive spectroscopy (XEDS); Auger electron spectroscopy (AES) and scanning Auger microscopy (SAM); secondary electron spectroscopy (SES) and secondary electron microscopy (SEM); annular dark-field (ADF) and high-angle annular dark-field (HAADF); coherent electron nano-diffraction (CEND); parallel electron energy-loss spectroscopy (PEELS); bright-field (BF) and dark-field (DF) [88].

Energy Dispersive X-ray Spectroscopy(EDS)

An incident electron is inelastically scattered at an atom of the specimen and knock outs a core electron, then an electron from a higher orbital fills the empty state (hole) in lower (core) orbital. The energy difference between these two orbitals is released in form of photons (when the core level electron of high enough atomic number is knocked out, the emitted photons have energy in the X-ray regime), whose energy is characteristic for the transition in the respective target atom by following Mosley's Law

$$\sqrt{\nu} = a(Z - b)$$

where ν is the characteristic X-ray frequency, a , b are the constants and Z is the atomic number of the atom. These X-rays are detected by spectrally resolved (the number of counts in a given energy width of typically few eV/channel) with an appropriate energy dispersive detector, like Si(Li) or SDD(silicon drifted detector). Typical energy resolution of such EDS detector is about 135 eV, which is good to carry out elemental characterization. To create an elemental map, an energy dispersive X-ray (EDX) spectrum is recorded for each scan point in STEM mode. The energy windows can be selected around certain spectral peaks, so that the respective peak intensity can be mapped against the position of the STEM probe. In this thesis, STEM based energy dispersive spectrometry (EDS) measurements were used to analyze the chemical composition of the materials.

Electron Tomography

Electron tomography is a tomography technique for getting detailed 3-dimensional structures of nano/micro structures or atomic columns. Electron tomography is an extension of traditional transmission electron microscopy and uses a (scanning) transmission electron microscope ((S)TEM) to collect the data. The process is as follows: a beam of electrons is passed through the sample different angles by rotating the sample around its center. At each tilted angle information is collected, this collected information is used to reconstruct a three dimensional image of the sample. Features with a diameter as small as 1-2 nm can be resolved in three dimensions by electron tomography [90].

The 3D information is reconstructed digitally from a tilt series of 2D projections, by acquiring images during the tilt of the sample from -70° to $+70^\circ$ while correcting simultaneously for image drift and focus changes. This tilt series is then processed off-line using software programs like inspect3D or matlab 3D tools to reconstruct the original 3D structures [91].

In this thesis, STEM, Electron tomography and EDS were carried out with 300 keV electrons in the Cs-corrected FEI Titan 80/300 system at the University of Bremen, Germany. The probe diameter was 0.2 nm during HAADF and STEM-BF mode.

2.3.4 X-Ray Diffraction

X-ray diffraction is a technique used for determining the crystal structures, such as lattice parameters and strain in the system. Crystal consists of regularly arranged array of atoms, and X-rays are electromagnetic waves. X-rays striking an electron produces secondary spherical waves emanating from the electron. This phenomenon is called elastic scattering and the electron is called scatterer. A regular array of scatterers produce a regular array of spherical waves which can interfere constructively or destructively.

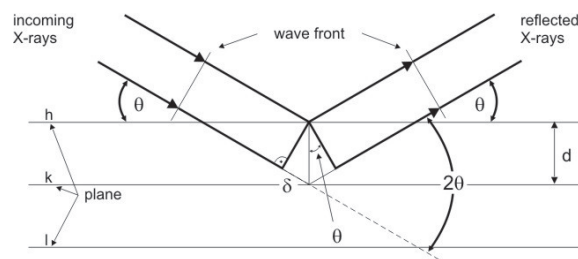


Figure 2.10: Schematic diagram of Bragg's Law

Incident X-rays fall on a sample and are reflected with the same angle as the incident angle, and these reflected beams undergo interference. This interfered beam is collected by a scintillation detector, which is converted into a voltage pulse. This pulse is fed to a computer to display the spectrum of intensity versus angle of incidence. The instrumentation of an XRD system broadly consists of an X-ray source, a goniometer for mounting the

sample and the detector in the reflection geometry. When the sample stage moves in the θ plane the detector will move in the corresponding 2θ plane to collect the data. Using X-ray diffraction technique crystalline samples can be characterized and growth directions, alloy formation and material compositions can be determined.

Bragg's Law

The diffraction of monochromatic X-rays takes place at those particular angles of incidence which satisfy the *Bragg law*, mathematically, Bragg's law can be written as follows:

$$2d\sin\theta = n\lambda \quad (2.3)$$

Here d is the inter-planar spacing of the diffracted planes, θ is the incident angle, n is an integer and λ is the wavelength of the incident X-ray beam (figure 2.10). When the diffraction condition in the equation 2.3 is satisfied, the scattering amplitude is determined by

$$F = N \int dV n(r) e^{(-iG \cdot r)} = NS \quad (2.4)$$

where S is called the structure factor and is defined as an integral over a single cell, with $r=0$ at one corner.

$$S = \sum_j f_j \exp[-i2\pi(v_1x_j + v_2y_j + v_3z_j)] \quad (2.5)$$

where f_j is called atomic form factor and can be written as $f_j = \int dV n_j(\rho) \exp(-iG \cdot \rho)$. $(x_j y_j z_j)$ is called a basis vector and $(v_1 v_2 v_3)$ are the miller indice of a plane for which the scattering factor is calculating. The structure factor S need not be real because the scattered intensity is S^*S , S^* is a complex conjugate of S so that S^*S is always a real quantity. At a zero S the scattered intensity will be zero, even though G is a perfect reciprocal vector or the plane satisfies the Bragg condition and such planes are called missing reflections.

In our experiments, we used synchrotron X-rays at Photon Factory, Japan because of their high intensity which will enable us to detect small amount of material. The energy tunability of synchrotron radiation allows to work with an appropriate wavelength for specific experiments.

Instrumentation

The Photon Factory is an accelerator-based light source facility and operates two storage rings, the 2.5 GeV PF ring and the 6.5 GeV PF Advanced Ring (PF-AR). The Photon Factory supplies brilliant X-rays and VUV light, which provide the means to understand the function of materials and life. The X-rays provided by the light source are directed towards beam line 18-B to perform the experiments at multipurpose monochromatic hard X-ray station by using bending method. This facility has been developed by Prof. M. K. Sanyal and his group at SINP, in collaboration with department of science and technology (DST). The X-ray beam is focused onto the sample using a double crystal monochromator consisting of channel cut Ge single crystal. Sample is mounted on 6 axis goniometer which has an angular resolution of 10^{-3} mrad.

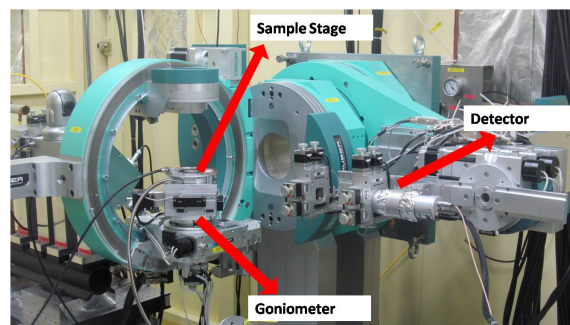


Figure 2.11: Experimental setup to perform X-ray diffraction installed at Indian beam line 18-B, Photon Factory, Japan

This goniometer allows us to move the sample in X, Y and Z axis and also can be rotated in Euler angles θ , χ , ϕ . Sample will be mounted on this goniometer which is aligned eucentrically. Incident X-rays fall on the sample and diffracted beam is collected by scintillation counter (model X2000, Cyberstar). This detector has a detector head of ϕ 48 mm with a preamplifier. This detector consisting of a fast scintillation detector and a pulse processor unit with a maximum throughput of 3×10^6 counts/second (cps) at 10 keV. This detector is connected with a computer through a serial link RS232. The diffracted signals are collected by this detector and pre-amplified and send it to the amplifier for the further signal processing and counting process.

Heating Stage for XRD

Many interesting phenomena occur at elevated temperatures. The use of XRD during annealing of specimen in real time is a powerful technique to understand the phase transformations, grain growth and crystal orientations leading to understand surface free energy minimization at elevated temperatures. In thesis work, *in-situ* experiments were done using a heating holder (Model DHS 1100, M/s. Anton Paar GmbH, Austria). It is custom designed to anneal the sample in different environments upto 1100 °C from room temperature (Figure 2.12). Control of the temperature will be done through TCU 200 controlling unit.



Figure 2.12: Heating stage used to perform the *in-situ* XRD measurements at Photon Factory, Japan (model DHS 1100, Anton Paar GmbH.)

The heating holder has a sample holder made of aluminium nitride above the heater to hold the sample of maximum diameter up to 25 mm and thickness up to 2 mm. This sample stage has virtues like fast and stable heating up to 1100 °C, excellent temperature homogeneity across the heating plate, accurate measurement of the sample temperature and chemically resistant ceramic heating plate with minimum tilt and expansion during the heating. The sample can be heated in many environments, like vacuum upto $\approx 10^{-2}$ mbar, air, inert gas and nitrogen. It can be operated at high pressure of 0.3 bar as well. Near the sample holder, there is a Pt-10% Rh-Pt thermocouple to measure the temperature. In order to maintain vacuum or avoid

oxygen contamination on the sample, a high transparent graphite material which has a transparency of 65% for Cu K_α radiation. Cooling of the stage is carried out using compressed air upto 200 °C and below this, the cooling of the stage is free cooling.

2.3.5 Rutherford Backscattering Spectrometry

Rutherford backscattering spectrometry (RBS) is a non destructive analytical technique used to determine the structural and compositional details of a material by analyzing the backscattered high energy ions. It is based on classical scattering in a central-force field [92]. Aside from the accelerator, which provides a collimated beam of MeV particles (usually He^+ or He^{++} ions), the instrumentation is simple. Semiconductor surface barrier detectors are used that have an output voltage pulse proportional to the energy of the particles scattered from the sample into the detector. The technique gives quantitative information, as MeV Helium ions undergo close-impact scattering collisions that are governed by the well-known Coulomb repulsion between the positively charged nuclei of the projectile and target atom and cross-section is given by Rutherford cross-section. More about various aspects of RBS technique can be found in ref. [93].

Kinematic factor

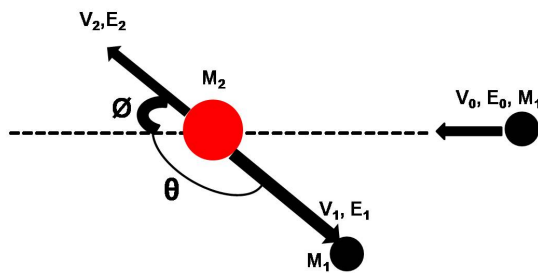


Figure 2.13: A schematic diagram of the interaction of two particles [93].

Kinematic factor (K_{M_2}) is defined as the ratio of energies of incident and backscattered ion. When a projectile with mass and energy M_1 and E_0 collides elastically with a stationary particle (target atoms) of mass M_2 ($M_2 > M_1$), energy will be transferred from the projectile to the target atoms. If the projectile energy (E_0) is much larger

than the binding energy of the target atoms, but less than the energy required for nuclear reactions and resonances, then the kinematic factor for this system shown in figure 2.13 can be expressed as:

$$K_{M_2} = \frac{E_1}{E_0} = \left[\frac{M_1 \cos\theta + (M_2^2 - M_1^2 \sin^2\theta)^{1/2}}{M_1 + M_2} \right]^2 \quad (2.6)$$

where E_0 is the incident ion energy, E_1 is the backscattered ion energy, M_1 is the atomic mass of the projectile (He ion), M_2 is the atomic mass of the target and θ is the angle of scattering.

Thickness analysis

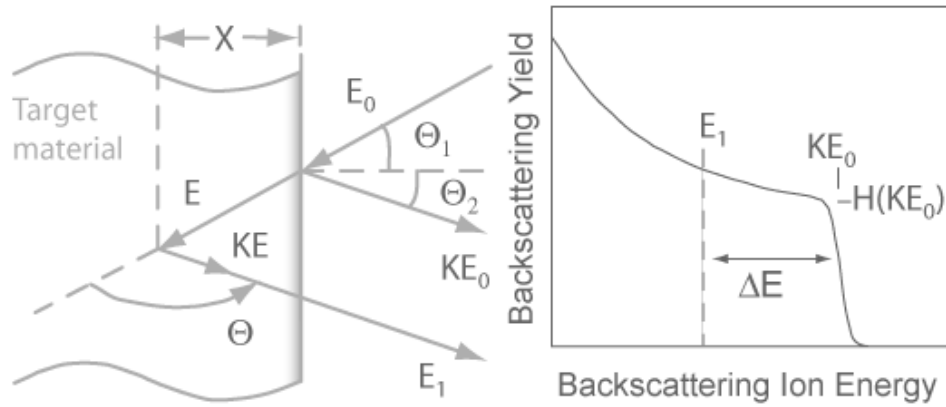


Figure 2.14: A schematic diagram of the RBS spectrum for a thin film [93].

Relative number of backscattered ions from a target atom within a certain solid angle $d\Omega$ is called as differential scattering cross section, and is given by

$$\frac{d\sigma}{d\Omega} = \frac{1}{Nt} \frac{dQ/d\sigma}{Q} \quad (2.7)$$

where N is the atomic density of the target atoms, and t is its thickness. σ is called average differential scattering cross section and can be defined as,

$$\sigma = \frac{1}{\Omega} \int_{\Omega} \frac{d\sigma}{d\Omega} d\Omega \quad (2.8)$$

and the differential scattering cross-section for an elastic collision between two atoms is given by Rutherford's formula,

$$\frac{d\sigma}{d\Omega} = \left[\frac{Z_1 Z_2 e^2}{4E_0} \right]^2 \frac{4}{\sin^4\theta} \frac{\left[1 - \left(\frac{M_1}{M_2} \sin\theta \right)^2 \right]^{1/2} + \cos\theta}{\left[1 - \left(\frac{M_1}{M_2} \sin\theta \right)^2 \right]^{1/2}} \quad (2.9)$$

where Z_1 and Z_2 are the atomic numbers of the projectile and target material respectively.

In other words, the total no of scattered particles can be written in terms of the height of the spectrum as $H_i = \sigma(E_i)QN.dt$, when the beam is falling normally onto the sample. Here, i denotes the number of equally smallest slabs for which backscattered energy can resolute, that means $t = i.dt$ and $\sigma(E_i)$ must be calculated at each backscattered energy E_i . Now, the total number of counts (area under the curve) is $A = \sum_i H_i$. In figure 2.14, H_0 denotes the total number of counts at energy $K_{M_2}E_0$. So total no of counts is given by,

$$A = H = \sum_i H_i = \sum_i \sigma(E_i)\Omega QN.dt = \sigma\Omega QNt \quad (2.10)$$

The value of A can be obtained by taking the area under the spectrum. From the RBS experiment, "Nt", effective thickness is determined as one can measure Ω , Q , A and σ is calculated using Rutherford scattering formula.

Instrumentation

RBS instrumentation can be broadly divided into three parts: accelerator, target chamber and detector (energy analyzer). In the accelerator part, H or He ions are generated through ionizing H or He gas at the source respectively. An injector magnet (90° bending magnet) is used to select the pre-accelerated He ions. Then, these ions are accelerated using the accelerator within the energy range of 1–3 MeV. Analyzing magnet is used to select the desired charge state of the accelerated He ions. Finally, the collimated beam of ions fall on the sample (target chamber). In the target chamber, a surface barrier detector (SBD) is used to detect backscattered projectiles kept at a very high angle ($\geq 150^\circ$). The sample is connected with the current integrator to get the total number of incident ions on the sample. The back scattered ions are collected by SBD and the signal is amplified by the preamplifier. This pre-amplified signal is further amplified by an amplifier, and the amplified signal is converted into digital signal by analog to digital converter (ADC). This converted data is goes to

multi channel analyzer (MCA). Finally, the output of MCA can be fed to the computer, where the resulting RBS spectrum can be stored. For the present thesis work, we have used 45° degree beam line of the 3 MV tandem Pelletron accelerator (9SDH2, NEC, USA) facility at IOPB [94]. Surface barrier detector was placed at 170° at a distance of about 11 cm from the sample holder. For the RBS measurements, 2.9 MeV He^+ ions were used and RBS simulation was carried by SIMNRA software package [95].

2.3.6 Raman Spectroscopy

In 1928, the Indian physicist C. V. Raman discovered that the visible wavelength of a small fraction of the radiation scattered by certain molecules differs from that of the incident beam and furthermore that the shifts in wavelength depend upon the chemical structure of the molecules responsible for the scattering [96].

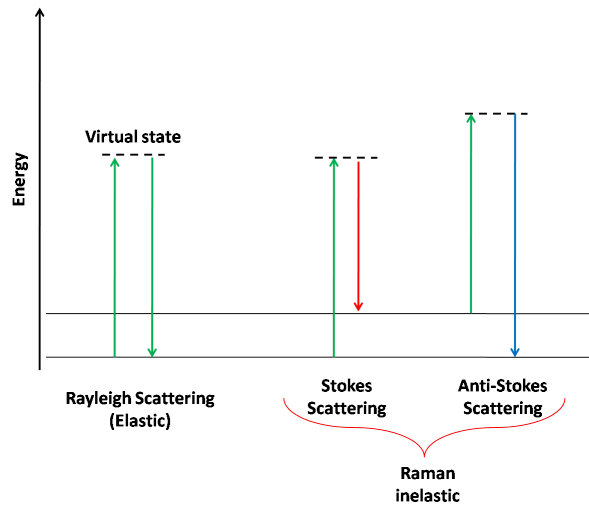


Figure 2.15: Schematic diagram of Raman scattering

The Raman spectroscopy is based on an inelastic light scattering by molecules (the Raman effect). In the Raman scattering process, a photon interacts momentarily with a molecule and is then scattered into surroundings in all directions. During the brief interaction with molecule, photon loses or gains energy which is then detected

and analyzed.

The Raman effect occurs when light impinges upon a molecule and interacts with the electron cloud of the bonds of that molecule. The incident photon excites one of the phonons into a virtual state. For the spontaneous Raman effect, the molecule will be excited from the ground state to a virtual energy state, and relax into a vibrational excited state, which generates Stokes Raman scattering [97]. If the molecule was already in an elevated vibrational energy state, the Raman scattering is then called anti-Stokes Raman scattering.

Surface Enhanced Raman Spectroscopy (SERS)

Surface enhanced Raman spectroscopy involves obtaining Raman spectra in the usual way on samples that are adsorbed on the surface of colloidal metal particles (usually silver, gold, or copper) or on rough surfaces of these metals. SERS phenomena were first discovered from measuring pyridine adsorbed on electrochemically roughened silver materials in 1974 by Martin Fleischman and his colleagues at Southampton University (Southampton, England) [98]. However, they concluded that the greatly enhanced signals were from the increased surface area. In 1977, Richard Van Duyne and his group at Northwestern University (Chicago, IL, USA) confirmed the SERS phenomena and firstly proposed the electromagnetic enhancement mechanism [99]. Both Nie and Kneipp groups achieved single-molecule detection independently with different experimental conditions [100, 101]. Nie et. al., study included a correlated topographical and optical characterization of unaggregated silver nanoparticles dosed with Rhodamine 6G (R6G) molecules. They concluded that the single-molecule enhancement was 10^6 to 10^7 larger than the population averaged enhancement. The Kneipp research group, on the other hand, probed small (100-150 nm) silver colloid aggregates dosed with crystal violet molecules. The large (10^{14}) single-molecule enhancement is hypothetically attributed to large electromagnetic fields generated by fractal-pattern clusters of silver colloid nanoparticles [101].

SERS Mechanism

Although the detailed mechanism of SERS enhancement has not been fully understood, most of the researchers believe in two different kinds of mechanisms are possible. One is attributed to electro magnetic enhancement (EM) and the other one is chemical enhancement.

(i) Electro magnetic (EM) enhancement in which the local electromagnetic (EM) field enhancement at the metal surface or rough metal structures due to surface plasmons. Surface plasmons are oscillating conduction electrons of the electromagnetic fields on a metal interface. In order to produce surface plasmon, the dielectric constant of the metal must be negative. Typical metals that support surface plasmons are silver, gold, copper, platinum, titanium, and chromium.

Generally, silver generates more surface plasmons than other metals due to its large negativity of dielectric constant. On smooth surfaces, plasmon excitation energy escapes and is lost as heat. Rough surfaces with localized space could accumulate some of the plasmons so that the plasma energy is radiated and generate high local electromagnetic fields. This is where rough surfaces or nanoparticle arrangement on surface are generally used in SERS experiments as these provide an area at which these localized collective oscillations can occur. The light incident on the surface can excite a variety of phenomena in the surface creates complexity which can be minimized by choosing the surface with features whose size is much smaller than the wavelength of light used, as only dipolar contribution will be recognized by the system. This dipolar term leads to the enhancement by contributing to surface plasmons. Incident light field is enhanced due to contribution from plasmon scattering which will excite the Raman modes of the molecules being studied leads to increase in the Raman signals. At each stage the electric field enhancement is E^2 , for a total enhancement is E^4 [102]. This enhancement is not possible for all frequencies of incident light. When the frequency of the incident light and the Raman signal frequency are nearly matches with the plasmon frequency then only resonance will occur and the enhancement of the field will be E^4 . If the incident light frequency and the Raman signal are not in resonance with plasmon frequency then the enhancement will not be maximum [103]. The choice of the nanoparticles or the metal surface is also dictated by plasmon frequency. Raman modes are generally excited by Visible or UV light.

The metal surface or nanoparticles should have their plasmon peak in this region to get maximum enhancement. Gold and Silver are the common metals used for SERS experiments because they have plasmon peak in these wavelength regime to provide maximum enhancement.

The enhancement observed in many systems cannot be explained fully based on electromagnetic theory as it can be applied regardless of the molecules being studied. Molecules with a lone pair of electrons can form a bond to the surface; a different enhancement mechanism has been described besides electromagnetic theory. This mechanism is based on the charge transfer between the metal surface and the chemisorbed molecule. This mechanism is valid only in specific case and probably occurs in concert with the electromagnetic mechanism [104, 105]. The HOMO to LUMO transition for many molecules needs much more energy than the UV or visible radiation energy involved in typical Raman experiments. When the HOMO and LUMO of the adsorbate molecule falls symmetrically about the Fermi level of the metal surface then half of the energy can be enough to make the transition, due to the action of metal as charge transfer intermediate [104]. In this way if a transition is possible in UV that can be occur in visible region in the presence of metal [103].

In this thesis, SERS measurements were done using micro-Raman spectrometer (LABRAM-HR) using laser excitation lines of 514.5 nm at room temperature at University of Hyderabad, Hyderabad and some experiments were done at Institute of Material and Minerals Technology, Bhubaneswar. The reason for recording SERS spectra with this excitation wavelength was to study resonance of adsorbate on Ag nanostructures. All measurements were made in a backscattering geometry, using a 50X microscope objective lens with a numerical aperture of 0.7. Typical laser power at the sample surface was 1mW with a spot size of 2 μm . A 20 μl of the CV solution (0.5 nM) were dropped onto the SERS substrate and dried naturally. A fixed volume micro-pipette with disposable tips was used to prevent contamination. In our tests the dropped solution soon spread over the whole SERS substrate but remained confined to the substrate. Crystal violet molecules were used to study the SERS due to its high Raman scattering cross-section.

Chapter 3

Coherently Embedded Ag Nanostructures in Si : 3D Imaging

3.1 Introduction

In this chapter, synthesis and characterization of coherently embedded Ag nanostructures that are formed during annealing of a 2 nm Ag/17 nm GeO_x/SiO_x/Si is studied. Three dimensional shape of these coherently embedded endotaxial structures for the case of Si(100) orientation has been determined using STEM based tomography technique. The role of GeO_x layer in the formation of substrate symmetric silver nanostructures on silicon substrate is also discussed.

Silver is a potential candidate for plasmonic applications due to its lowest onresonance loss in the visible spectrum. Besides plasmonic applications, silver nanostructures can also be used as antennas to convert light in to localized electric fields or as wave guides to route the light to specified locations with a precision of few nanometers [106], photonic crystals and in infrared polarizers [107, 108]. Embedded Ag nanoparticles have been found to enhance the light absorption in semiconductors, due to their strong plasmonic near-field coupling [109]. Due to the large contingent of applications of Ag nanostructures, it is a challenge to control the shapes, size, composition and placement/position of Ag nanostructures. Wiley et al., reported a solution-phase polyol synthesis for controlled shapes of Ag nanostructures, such as, pentagonal nanowires, cuboctahedra, nanocubes, nanobars etc [110].

In this chapter, we are discussing on the growth of various shapes of coherently embedded or/and endotaxial Ag nanostructures on silicon substrates using a physical vapor deposition method (PVD). We present a simple process to grow substrate symmetry-driven silver nanostructures on silicon substrate by annealing the samples at ≈ 800 °C in air. The very nature of Ag nanostructures (i.e. embedding coherently in substrate) would provide a stable substrate for SERS applications. We present 3-D imaging of these embedded structures using scanning transmission electron microscopy (STEM) based tomography. Our results reveal an interesting process involving a low-temperature etching of native oxide of the silicon substrate using GeO_x as an intermediate layer to help the growth of the endotaxial Ag nanostructures. The term endotaxy here refers to the growth of precipitate phases in a bulk matrix, with coherent interfaces surrounding the precipitate [55]. Using traditional gas phase or solution phase methods, formation of various shapes and sizes of Ag nanostructures has been reported, but they are not endotaxial in nature. It is also be noted that, traditionally, endotaxial structures were prepared with molecular beam epitaxy (MBE) in ultra high vacuum conditions (UHV) [59]. Earlier reports indicated that endotaxial structures have potential applications in thermoelectric, magnetic systems, spin polarized contacts, opto-electronic components and nanoelectronics [59].

3.2 Experimental Section

Silicon wafers of various orientations i.e., (100), (110) and (111) were cleaned by standard procedure of rinsing and sonication with alcohol and de-ionized water. A ≈ 2 nm thick SiO_x (native oxide) layer is also present on all the silicon substrates. Deposition of GeO_x and silver was done by physical vapor deposition (PVD) system. We have used three configurations: (a) a ≈ 17 nm thick GeO_x was deposited on Si(100), Si(110) and Si(111), then the deposition of 2 nm silver was done on 17 nm $\text{GeO}_x/\text{SiO}_x/\text{Si}$. (b) a ≈ 2 nm thick Ag was deposited on Si followed by GeO_x deposition of about 17 nm thick and (c) a 2 nm thick Ag was deposited on Si. All these three types of samples are annealed in a horizontal tube furnace up to 800 °C in atmosphere. A Carl Zeiss Neon 40 Field Emission Gun Scanning Electron Microscope (FEGSEM) and JEOL JEM-2010 high resolution transmission electron microscope (HRTEM) were used to study the morphology and structure. An FEI Titan 80/300

TEM/STEM microscope operated at 300 KeV was used for all STEM measurements. The HAADF detector covered an angular range of 33-200 mrad. For tomography, a single-tilt Fischione tomography sample holder was used and images have been acquired between -66° and $+66^\circ$ of tilt around the substrate surface normal in steps of 2° . The simultaneous iterative reconstruction technique (SIRT) was used for reconstruction with 10 iterations.

Planar and X-TEM samples were prepared by mechanical thinning of the specimen followed by argon ion milling to achieve electron transparency. Synchrotron based x-ray diffraction measurements have been carried out at BL-18B, Photon Factory (PF), KEK using 11.38 keV x-rays.

3.3 Results and discussion

3.3.1 Growth of Endotaxial Ag nanostructures in Si(100): A simple PVD method

Using physical vapor deposition and annealing in ambient conditions, we have succeeded in growing the coherently embedded nanostructures of Ag in Si. The results presented in figure 3.1 depict the shape variation of Ag nanostructures depending on the substrate orientation. For (100), (110) and (111), the surface unit cell has 4-fold, 2-fold and 3-fold symmetry, respectively. The shape of Ag nanostructures is commensurate with the substrate surface symmetry (4, or 2 and 3 fold symmetry for (100), (110) and (111) orientations, respectively) as shown in figure 3.1.

Figure 3.1 (a) depicts a bright field (BF) planar TEM micrograph for 2 nm Ag/17 nm $\text{GeO}_x/\text{SiO}_x/\text{Si}(100)$ annealed at $\approx 800^\circ\text{C}$ in air for 30 minutes. This shows formation of square/rectangular shaped silver nano-structures on Si(100) substrate following a four-fold symmetry of the substrate unit cell. By considering about 220 particles from many TEM micrographs, the average length of the square/rectangle shape Ag nanostructures is found to be $110\text{ nm} \pm 50\text{ nm}$ and average breadth is $100\text{ nm} \pm 40\text{ nm}$ with an aspect ratio of 1.1. Also, figure 3.1 (b) reveals the formation of silver nanorod structures for the 2 nm Ag/17 nm $\text{GeO}_x/\text{SiO}_x/\text{Si}(110)$ annealed at ≈ 800

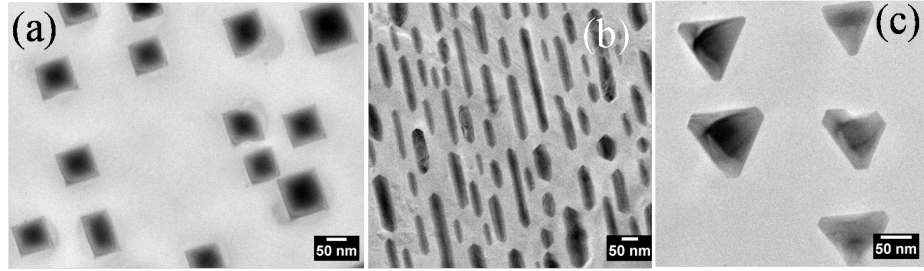


Figure 3.1: Planar TEM Micrographs of 2 nm Ag/17 nm $\text{GeO}_x/\text{SiO}_x$ on (a) Si(100), (b) Si(110) and (c) Si(111) annealed at 800 °C in air.

°C in air for 30 minutes, following the substrate's two-fold symmetry. The average length and width of the rod shaped Ag nanostructures is found to be $150 \text{ nm} \pm 80 \text{ nm}$, $30 \text{ nm} \pm 10 \text{ nm}$ with an aspect ratio of ≈ 5.0 ; From the associated error it is clear that a wide distribution of sizes is observed. Figure 3.1 (c) is for the 2 nm Ag/17 nm $\text{GeO}_x/\text{SiO}_x/\text{Si}(111)$ annealed at $\approx 800 \text{ °C}$ in air for 30 minutes and this reveals the triangular nanostructures formed by following a three-fold symmetry of the Si(111) substrate unit cell.

Figure 3.2 (a) shows a low magnification cross-sectional TEM (X-TEM) bright field (BF) image of as-deposited 2 nm Ag/17 nm $\text{GeO}_x/\text{SiO}_x/\text{Si}(100)$. This confirms the presence of spherical silver nanoparticles on top of an amorphous GeO_x layer. It should be noted that a physical vapor deposition of Ge in high vacuum condition yielded GeO_x layer. Oxygen partial pressure in the chamber is high compared to UHV in high vacuum ($\approx 10^{-5}$ mbar) might be a reason for the formation of GeO_x . The as-deposited Ag thin film showed isolated irregular nanostructures. From figure 3.2 (a), the thicknesses of the GeO_x and the native oxide (SiO_x) layers were found to be $\approx 17 \text{ nm}$ and $\approx 2 \text{ nm}$, respectively. Figure 3.2 (b) depicts a low magnification BF X-TEM micrograph of 2 nm Ag/17 nm $\text{GeO}_x/\text{SiO}_x/\text{Si}(100)$ at $\approx 800 \text{ °C}$ (annealing done in air for 30 minutes). From this micrograph, the thickness of GeO_x is found to be $\approx 75 \text{ nm}$ and that of SiO_x is $\approx 20 \text{ nm}$ thick. Following the annealing in air, the GeO_x and SiO_x layer thicknesses was increased by a factor of ≈ 3.4 and ≈ 9 , respectively. The cross-sectional image taken (for 2 nm Ag/17 nm $\text{GeO}_x/\text{SiO}_x/\text{Si}(100)$ @800 °C), shown in figure 3.2 (b), confirms the embedding of silver into the silicon substrate. Figure 3.2 (c) represents a high resolution lattice image of a small area shown in

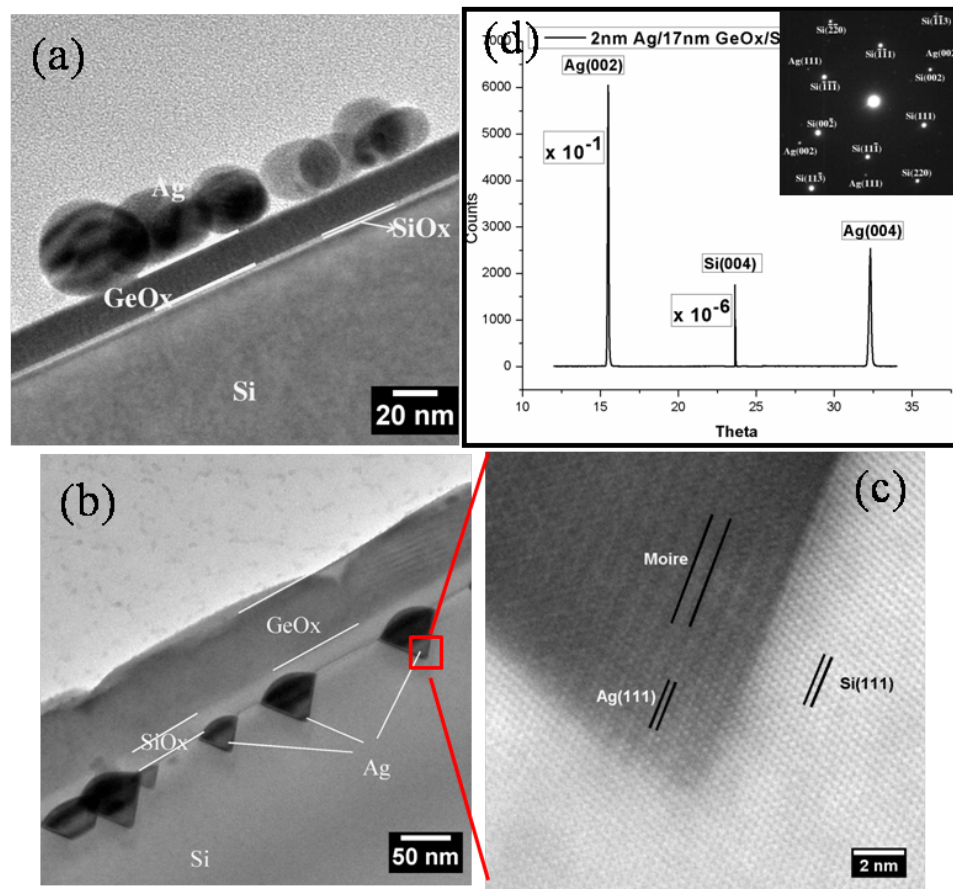


Figure 3.2: X-TEM Micrographs of 2 nm Ag/17 nm GeO_x/SiO_x/Si (100) (a) Low Mag of as-deposited (b) Low Mag of 800 °C annealed in air (c) HR-X-TEM depicts endotaxial structures (with Moire fringes) and (d) X-ray diffraction pattern showing the single crystalline nature of the Ag nano structures which also complimented by a selected area diffraction (SAD) pattern taken from a single structure.

Figure 3.2 (b). This lattice image confirms the presence of Ag (111) (0.238 ± 0.005 nm) and Si (111) (0.315 ± 0.005 nm) lattice planes as an endotaxial structure. The lattice images depict the presence of Moiré fringes in the structures, which confirms the presence of the coherent embedment nature of silver nanostructures in silicon. The Moiré fringe spacing can be determined by

$$d_m = \frac{d_1 d_2}{(d_1 - d_2)^2 + d_1 d_2 \beta^{2^{1/2}}}$$

where d_1, d_2 are lattice spacings of the planes which are constituents of Moiré fringes and β is the angle between the planes [111]. The Moiré fringe spacing of 0.96 nm was calculated between Ag(111) and Si(111) planes with $\beta=0$. This matches well with the measured fringe spacing from our measurements (Figure. 2(c)) is 0.95 ± 0.01 nm. Figure 3.2 (d) is the synchrotron XRD spectrum of the 2 nm Ag/17 nm $\text{GeO}_x/\text{SiO}_x/\text{Si}(100)$ at ≈ 800 °C in air for 30 minutes, which depicts the single crystalline nature of the silver nanostructures on silicon (100) substrate. In the XRD spectrum only Ag(002) and Ag(004) peaks were observed along with the Si(004) peak which belongs to the substrate. The XRD data confirms the presence of crystalline Ag structures over a wide range. The inset of figure 3.2 (d) shows the selected area electron diffraction (SAED) pattern taken on a single endotaxial nanostructure. The pattern confirms the single crystalline nature of the silver nanostructures. XRD and SAED confirm the macroscopic and microscopic nature of the Ag nanostructures.

3.3.2 Plausible Mechanism

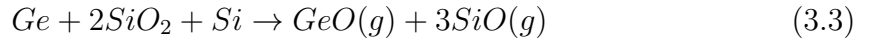
We propose a plausible mechanism involved in the enhanced desorption of SiO_x and GeO_x at initial stages [112]. During annealing of the sample, GeO_x desorbs into volatile GeO from the metal edges by forming intermediate solid GeO(s) [113] It has been reported that GeO desorbs from a solid GeO layer at > 300 °C [114]. In our case, the metal could be a catalyst for the formation of GeO(s) which then desorbs as GeO gas [115].



Wang et al. reported the disproportionation of GeO into Ge and GeO_2 [116], and they have also shown the formation of crystalline germanium above 600 °C annealing.



Ge formed in the disproportionation of GeO thus has a possibility to react with native SiO_x to form volatile SiO around 750 °C. Furthermore, Yun et al., reported the desorption of SiO from SiO_2 in the vicinity of Ge: [117]



In a proposed cyclic process the GeO formed in this reaction (3) also disproportionate into GeO_2 and Ge and the Ge will help desorption of SiO_2 into volatile SiO resulting a competition between GeO disproportionation, SiO desorption and SiO_2 formation. It is well known from literature that silver diffuses into silicon through an interstitial-substitution mechanism [118, 119]. Ag diffusion to reach the silicon surface has been enhanced due to desorption of SiO_x and GeO_x . This would presumably happen during annealing. During cooling, initially, oxidation of the silicon substrate occurs which might be a reason for increased thickness of the SiO_x layer, the condensation of GeO_x might take place at a lower temperature compared to SiO_x . The increase of the GeO_x layer is also observed from the cross-sectional TEM micrograph (figure 3.2(b)) which might be explained through the stoichiometric oxide formation.

3.3.3 Chemical Analysis and 3D Imaging

In order to understand the chemical nature of the system, a two-dimensional energy-dispersive x-ray (EDX) analysis of a typical endotaxial structure has been performed in STEM mode as shown in Figure 3.3. The high-angle annular dark field (HAADF) Z-contrast STEM micrograph in figure 3.3 (a) depicts the investigated region containing a 50 nm wide pyramidal structure. As shown by the Oxygen map in figure 3.3(b), the endotaxial structure itself is free of oxides while the presence of oxygen is clearly confirmed in the top two oxide layers. Together with the silicon map in figure 3.3(c) and the germanium distributions in figures 3.3(d,e), the first oxide layer from the substrate side is identified as SiO which turns into the topmost layer of mixed GeO and SiO. Moreover, figure 3.3(c) exhibits a significant silicon deficiency in the endotaxial formation, suggesting the substitution of silicon here. In fact, the silver map in figure 3.3(f) reveals that the investigated structure consists of silver which is also in agreement with the high Z-contrast observed in the HAADF image (as in figure 3.4 (a), (b)). Together with the SAED shown in figure 3.2(d), we can

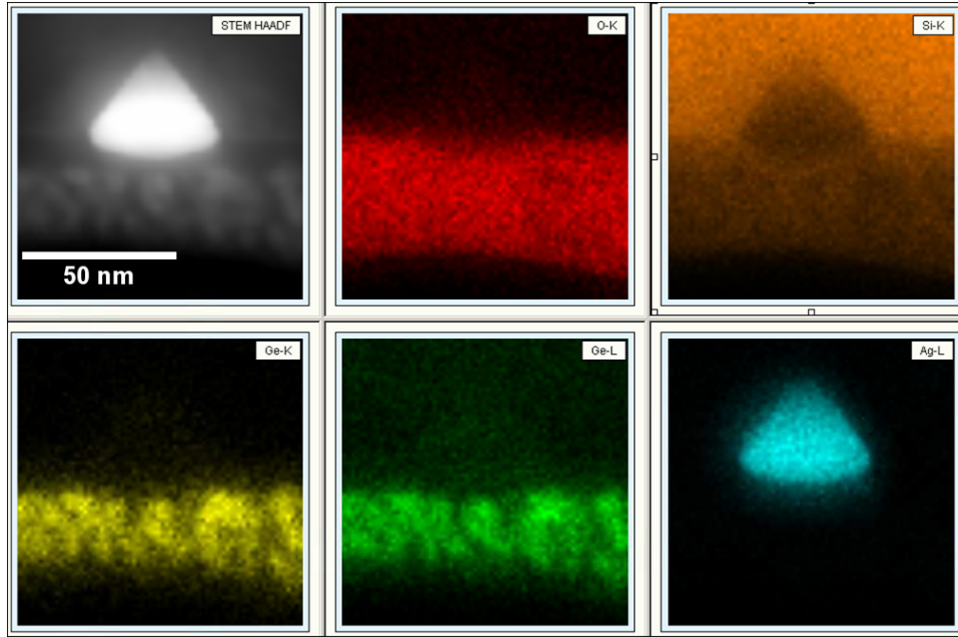


Figure 3.3: STEM- EDX Elemental of mapping 2 nm Ag /17 nm $\text{GeO}_x/\text{SiO}_x/\text{Si}$ (100) at 800 °C (a) STEM Micrograph, (b) Oxygen mapping, (c) Si mapping, (d), (e) Ge K, L mapping and (e) Ag mapping

preclude the presence of silver silicide because silver and silicon lattice spacings constitute a ratio of $\frac{3}{4}$ which matches with the expectation for the pure materials exactly.

The plane- and cross-sectional TEM studies in figures 1(a) and 2(b,c) already imply that the silver nanostructures obey a pyramidal shape with a quadratic base which has a [100] surface normal. Moreover, figure 3.4(b) exhibits an angle of $\alpha=70.0^\circ$ between the projected Ag/Si interface which agrees well with the theoretical angle of 70.5° for 111 facets. However, to prove that the silver nanostructures are indeed terminated by four microscopically flat 111 facets in addition to the quadratic base, STEM tomography has been performed to allow for the 3D reconstruction shown in figure 3.4(b). This demonstrates the termination by $(\bar{1} 1 \bar{1})$ and $(1 1 \bar{1})$ facets in this particular perspective.

Finally, we calculated the equilibrium shape of silver embedments in silicon theoretically by considering energies for different crystallographic orientations of the Ag/Si interface. We took the energies from Xin et al., [120] who computed energies for

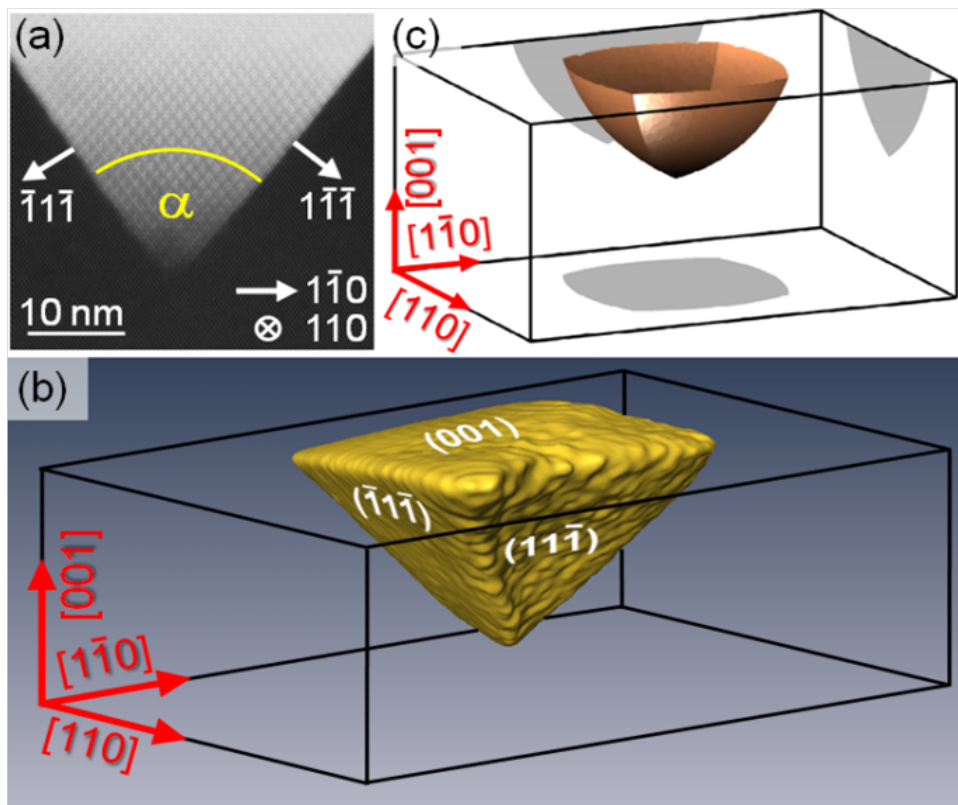


Figure 3.4: (a) STEM HAADF micrograph of 2 nm Ag/17 nm GeO_x/ SiO_x/ Si(100) at 800 °C annealed in air, with selected directions indexed from this 2D projection. (b) Reconstructed 3D tomography view of one of the endotaxial islands, showing that the silver embedment is terminated by (111) facets and an (001) base. (c) Result of the Wulff construction, explaining this pyramidal shape and its orientation theoretically in terms of interface energy

Ag(001)/Si(111), Ag(011)/Si(111) and Ag(111)/Si(111) twisted interfaces. By Wulffs construction [121,122], we then found the terminating facets of the Ag embeddings in figure 3.4(c) for the case that the Ag facets are lying on Si (111) facets. As the shape agrees well with the reconstruction in figure 3.4(b), we conclude that the observed pyramid formation is driven by Ag/Si interface energy minimization and takes the shape close to thermodynamic equilibrium.

3.3.4 Other Substrate Orientations i.e. Si(110), Si(111)

For 2 nm Ag/17 nm $\text{GeO}_x/\text{SiO}_x/\text{Si}(110)$ annealed in air at 800 °C yields nanorod structures shown in figure 3.1(b). Figure 3.5 (a) shows the low mag cross-sectional TEM micrograph of the 2 nm Ag/17 nm $\text{GeO}_x/\text{SiO}_x/\text{Si}(110)$ annealed in air at 800 °C revealing the endotaxial nature of these nanorods and from the fig 3.5(b) which is HRTEM micrograph of one of the nanorod a lattice spacing of 0.145 nm on the nano structure and 0.193 nm on the substrate were measured. These measured values are matching with inter planar spacing of Ag(220) plane and Si(220) plane respectively and these planes are parallel to each other. Figure 3.5 (c) is the SAED pattern taken on one of the nanorod revealing the single crystalline nature of these nanostructures along with the fact that the arrangement of these nanorods is parallel to the substrate.

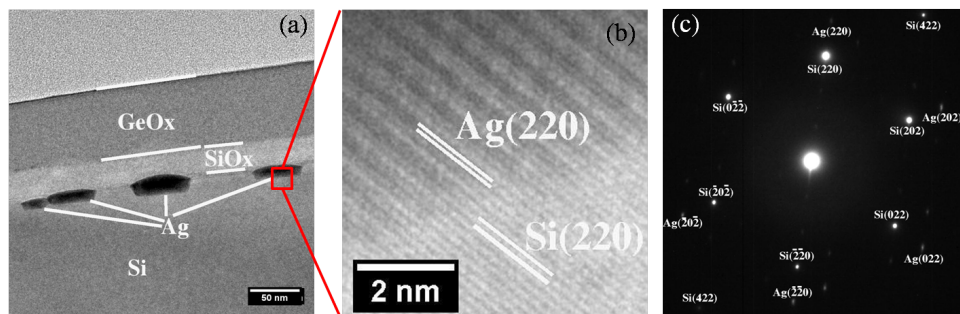


Figure 3.5: X-TEM Micrographs of 2 nm Ag/17 nm $\text{GeO}_x/\text{SiO}_x/\text{Si}(110)$ at 800 °C in air (a) Low Mag X-TEM (b) HR-X-TEM depicts endotaxial structures (with Moire fringes) and (c) Diffraction pattern on single structure

For 2 nm Ag/17 nm $\text{GeO}_x/\text{SiO}_x/\text{Si}(111)$ annealed in air at 800 °C yields nanotriangular structures shown in figure 3.1(c). Figure 3.6 (a) shows the low mag cross-sectional

TEM micrograph of the 2 nm Ag/17 nm $\text{GeO}_x/\text{SiO}_x/\text{Si}(111)$ annealed in air at 800 °C revealing the hat shaped embedded nanostructures and from the fig 3.6(b) which is HRTEM micrograph of one of the nanostructure, a lattice spacing of 0.236 nm on the nanostructure and 0.316 nm on the substrate were measured. These measured values are matching with inter planar spacing of Ag(111) plane and Si(111) plane respectively and these planes are parallel to each other. Figure 3.6 (c) is the SAED pattern taken on one of the nanostructure revealing the single crystalline nature of these nanostructures along with the fact that the arrangement of these nanostructure is parallel to the substrate. The extension of the triangle within the substrate leads to hat shape of the structure due to high removal of Si atoms along Si(111) direction might be a reason.

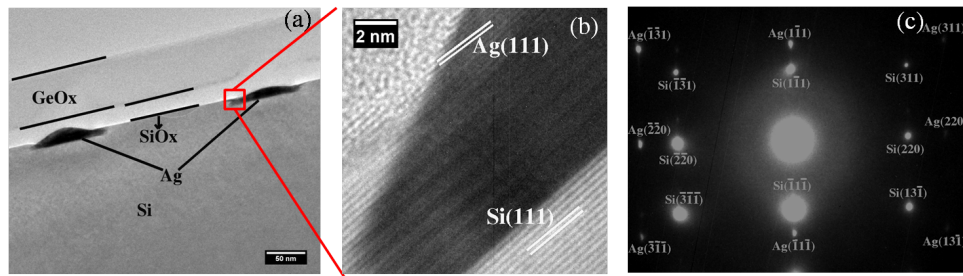


Figure 3.6: X-TEM Micrographs of 2 nm Ag/17 nm $\text{GeO}_x/\text{SiO}_x/\text{Si}(111)$ at 800 °C in air (a) Low Mag X-TEM (b) HR-X-TEM depicts endotaxial structures (with Moire fringes) and (c) Diffraction pattern from a single structure

3.3.5 Role of GeO_x Layer

In order to understand the role of GeO_x to form substrate symmetric endotaxial silver nano structures, samples of silver on native oxide silicon substrate are also prepared and annealed at ≈ 800 °C under the same conditions, like 2 nm Ag/17 nm $\text{GeO}_x/\text{SiO}_x/\text{Si}(100)$. Figure 3.7 (a) is the SEM micrographs of 2 nm Ag/2 nm $\text{SiO}_x/\text{Si}(100)$ annealed at ≈ 800 °C. Interestingly, no ordered structures have been observed. Figure 3.7(b) is the low magnification X-TEM micrograph of as deposited 2 nm Ag/ $\text{SiO}_x/\text{Si}(100)$ revealing the silver nanoparticles on silicon substrate separated by native oxide layer. Figure 3.7(c), (d) are the X-TEM images of low magnification and high resolution of 2 nm Ag/2 nm $\text{SiO}_x/\text{Si}(100)$ annealed at ≈ 800 °C

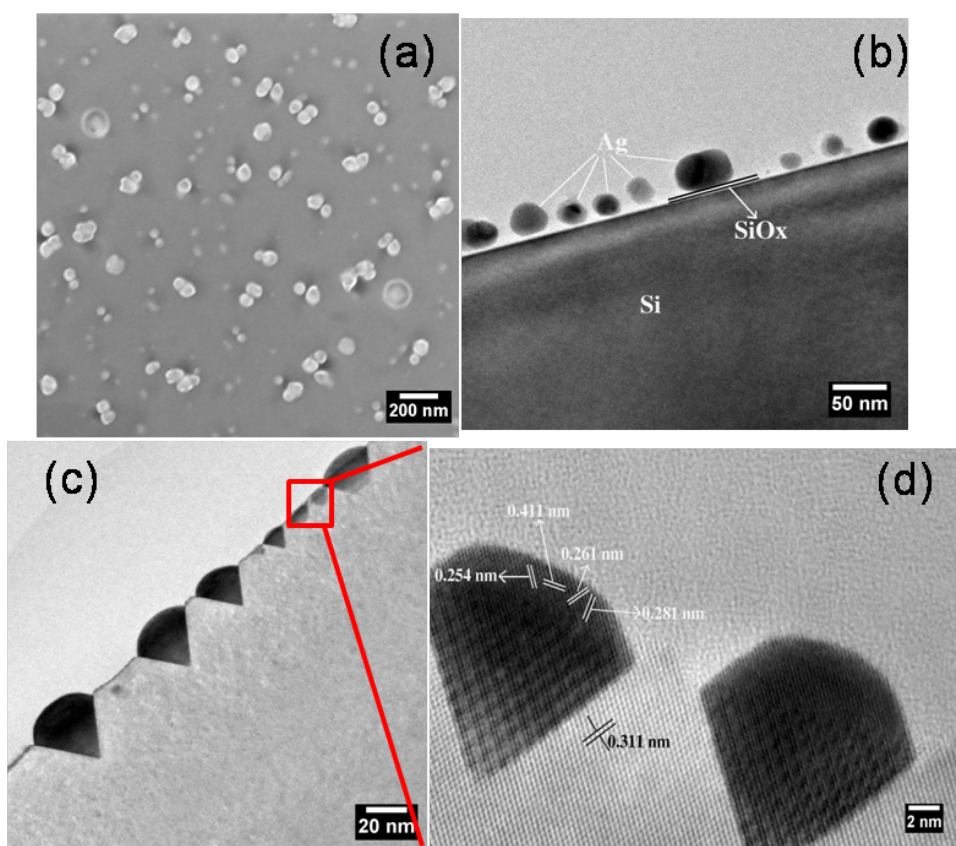


Figure 3.7: (a) SEM Micrograph of 2 nm Ag/SiO_x/Si (100) at 800 °C in air, X-TEM Micrographs of 2 nm Ag/SiO_x/Si (100)(b) as-deposited and annealed at 800 °C in air (c) Low Magnification (d) HRTEM of selected area depicts endotaxial structures.

in air revealing the embedding of silver into silicon substrate like 2 nm Ag/17 nm $\text{GeO}_x/\text{SiO}_x/\text{Si}(100)$ at 800 °C. From the HR-X-TEM image, inter planar spacings of 0.254 nm, 0.261 nm, 0.281 nm and 0.411 nm on the structures and 0.311 nm on the substrate have been measured. From these values, 0.254 nm, 0.261 nm are matching with the (131) planes of Ag_2Si , 0.281 nm is matches with the (200) planes of Ag_2Si phase. HR-X-TEM image depicts the presence of Moire fringes in the structures, the Moire fringe spacings using $\text{Ag}_2\text{Si}(131)$ and $\text{Si}(111)$ planes with zero angle yields 1.47 nm, which matches with the measured value $1.46 \text{ nm} \pm 0.02 \text{ nm}$. In this case, formation of Ag_2Si was found within the structures and these structures are also endotaxial in nature (figure 3.7(d)). This can be explained through the consumption of thermal energy for alloy formation. Mc Brayer et al., reported that silver inter diffuses through SiO_2 layer in the form of Ag^+ ion, [123] which will react with the silicon atoms to form alloy at lower temperatures compared to silver atoms. From the observations of 2 nm Ag/2 nm $\text{SiO}_x/\text{Si}(100)$ @800 °C, presence of GeO_x plays a key role in the formation of substrate symmetric single crystalline silver endotaxial nanostructures. We now address the position of GeO_x layer in the formation of these nanostructures.

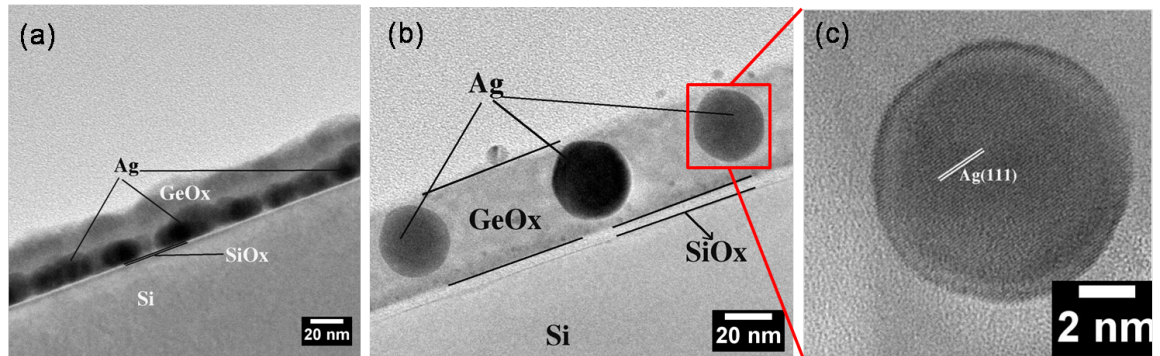


Figure 3.8: X-TEM Micrographs of (a) low mag of as-deposited 17 nm $\text{GeO}_x/2 \text{ nm Ag /SiO}_x/\text{Si}(100)$ (b) Low Mag (c) HR-X-TEM of 17 nm $\text{GeO}_x/2 \text{ nm Ag /SiO}_x/\text{Si}(100)$ @ 800 °C in air respectively..

In order to understand the role of GeO_x position at Ag and Si interface, samples of 17 nm $\text{GeO}_x/2 \text{ nm Ag}/2 \text{ nm SiO}_x/\text{Si}$ were prepared and annealed under the same condition as above both systems were annealed. Figure 3.8 (a) is the low magnification X-TEM micrograph of as deposited 17 nm $\text{GeO}_x/2 \text{ nm Ag}/2 \text{ nm SiO}_x/$

Si(100) shows the irregular Ag structures on top of native oxide are covered along with the inter particle space is filled by GeO_x layer. Figure 3.8 (b) and (c) are the X-TEM micrographs of low magnification and HR-X-TEM of 17 nm GeO_x / 2 nm Ag/2 nm SiO_x / Si(100) annealed at 800 °C. X-TEM micrograph reveal the formation of embedded Ag nanostructures in the GeO_x layer and the presence of oxide layer in between the silicon substrate and nanostructures. From HR-X-TEM image, inter planar distance of 0.239 nm on spherical nano particles which corresponds to Ag (111) plane was measured. Oniki et. al., reported that desorption of GeO_2 into volatile GeO occurs at lower temperatures in presence of metals compared to the absence of metal at the SiO_2 /Si interface. This could be one of the possible reasons for the embedded Ag nanostructure formation because of the incomplete desorption of GeO_x within the time and temperature available for the system to react with SiO_x . From above observations it is evident that the position and presence of GeO_x layer plays a key role in the formation of substrate symmetric single crystalline silver endotaxial nanostructures.

3.4 Chapter Summary

Substrate symmetry driven silver nano structures are formed on silicon surface by annealing the 2 nm Ag/17 nm GeO_x / SiO_x /Si samples in ambient conditions at high temperatures. Endotaxial nano squares/rectangles are formed in the case of Si(100), endotaxial nanorods are formed on Si(110) and endotaxial nano triangles are formed for Si(111) substrate according to their 4-fold, 2-fold and 3-fold symmetries of substrate unit cells respectively. These results show a simple and novel procedure to fabricate controlled shapes of Ag or Ag_xSi_y endotaxial nanostructures. 3-D structural analysis was carried out using STEM-tomography for the case of Si(100) substrate orientation. Not only the presence of GeO_x effects the substrate symmetric structures formation but also its position also play a critical role. The detailed study of effect of annealing ambience on these structures will be discussed in the next chapter.

Chapter 4

Study of the Buried Interfaces during the Silver Endotaxy in Silicon under Various Ambient Conditions

4.1 Introduction

In the previous chapter, growth of coherently embedded silver nanostructures under simple conditions, such as, annealing in air at high temperature and the use of faster etching of native oxide in presence of an intermediate layer (GeO_x) has been presented. In this chapter, results on the role of ambience during high temperature annealing is presented. This is an important aspect as these results enable to complement and help to understand the growth mechanism of endotaxial structures. Annealing under the Ar, O_2 , low vacuum (LV) and ultra high vacuum (UHV) environment has been studied for Ag/ GeO_x / SiO_x /Si(100) system.

Metal nano particles play key role in many applications due to their high surface area availability and plasmonic properties. It is known that metal nano particles are good optical materials due to their surface plasmon resonance (SPR) properties. Among metal nano particles silver has wide photonic applications due to its lowest on resonance loss in the visible spectrum [37, 38]. Size, shape and coverage of the nano particles play a crucial role in SPR peak positions and surface enhanced Raman

scattering (SERS) signal enhancement. Many optical applications are governed by the electron-relaxation rates that depend on the size of the nanostructures [124]. It is known that the quantum size and the chemical interface effect caused by static and dynamic charge transfer between a particle and the surrounding material would play an important role. [38, 124–130] Embedded Ag nanoparticles found to enhance the light absorption in the semiconductors, due to their strong plasmonic near-field coupling [131]. This chapter is focused on understanding the role of ambience during annealing process. In this work, we report on the effect of ambience to understand the reaction processes at the interfaces in Ag/GeO_x/SiO_x/Si(100) system by annealing it under various conditions, such as air, low vacuum, argon flow, oxygen flow, and ultrahigh vacuum (UHV). By changing the ambient conditions, we show that the size, shape and position of silver nanostructures and surrounding matrix around these Ag nanostructures can get modified. Availability of oxygen appears to play a vital role in the reaction at the interfaces. A proper understanding of the processes would yield to make us of this particular system to grow controlled endotaxial Ag nanostructures. The present study is a step in this direction. A detailed characterization of resulting surface and interfaces has been carried out ex-situ using field emission scanning electron microscopy (FESEM), transmission electron microscope (TEM), synchrotron x-ray diffraction (XRD) and Rutherford backscattering spectrometry experiments (RBS).

4.2 Experimental methods

Silicon (n-type, with 6-14 ohm-cm resistivity) wafers were cleaned by ethanol and ultrasonicated with ethanol for 10 minutes and rinsed with deionized water. A thin layer of ≈ 2 nm SiO_x is found to be present as native oxide. Deposition of germanium and silver was done by physical vapor deposition (PVD) process using a resistive heating boat in high vacuum conditions. Germanium deposition in PVD system resulted in the formation of GeO_x. First, a ≈ 17 nm GeO_x was deposited on Si (100), and this was followed with further deposition of ≈ 2 nm Ag on 17 nm GeO_x/SiO_x/Si (100). This system consisting of 2 nm Ag deposited on 17 nm GeO_x/SiO_x (native oxide)/Si (100) is henceforth represented as AGS. Annealing of the samples at 800 °C was carried out in a side entry furnace with a quartz tube of 80 cm length and 5

cm diameter under different ambient conditions: (i) air (ii) argon with a flow rate of 20 sccm (iii) low vacuum of $\approx 10^{-2}$ mbar and (iv) oxygen with flow rate of 20 sccm and in (v) ultra high vacuum of $\approx 10^{-9}$ mbar using MBE chamber. Cross-sectional TEM samples were prepared by mechanical polishing followed by low energy Ar^+ ion milling to achieve the electron transparency. TEM measurements were carried out by using 200 keV electrons. Synchrotron X-Ray Diffraction (XRD) measurements were done at Photon Factory, KEK, Japan (at Indian Beam line 18B) with a wavelength of 1.089 Å. RBS measurements were carried out using 3.0 MeV He^+ ions. Scanning electron microscope (SEM) measurements were carried out with 30 keV electrons using a field emitter gun based (FEG) SEM.

4.3 Results and discussions

The results of ambience dependence are divided into two cases: (i) embedded spherical silver nanostructures formed in oxygen ambience, spherical nano structures in the case of UHV annealing, and (ii) substrate symmetric endotaxial silver nano structures formed in air, low vacuum and argon ambiances. Figure 4.1 (a) is the SEM micrograph of the as-deposited AGS specimen (i.e., 2 nm Ag/17 nm $\text{GeO}_x/\text{SiO}_x/\text{Si}(100)$) depicting the irregular shaped silver islands. Figure 4.2(a) depicts a low magnification cross-sectional TEM (XTEM) image of as-deposited AGS revealing the position of silver nanostructures on top of ≈ 17 nm GeO_x layer on native oxide covered silicon substrate.

Initially, the results for the embedded case (i.e oxygen ambience) will be discussed: Figure 4.1(b) depicts a scanning electron microscopy (SEM) micrograph of AGS annealed at 800 °C in oxygen ambience with a flow rate of ≈ 20 sccm. This SEM micrograph reveals the irregular shaped structures. Figure 4.2(b) depicts a low magnification cross-sectional TEM micrograph revealing the embedded spherical silver nano particles in the SiO_x layer. The average diameter of these embedded silver nanostructures found to be $\approx 19 \text{ nm} \pm 8 \text{ nm}$. During annealing of the sample, GeO_x desorbs into volatile GeO from the metal edges by forming intermediate solid GeO(s) [113]. As reported earlier by Bernstein and Cubicciotti [115], increasing the oxygen pressure decreases the rate of evaporation of GeO(s) resulting into two possible

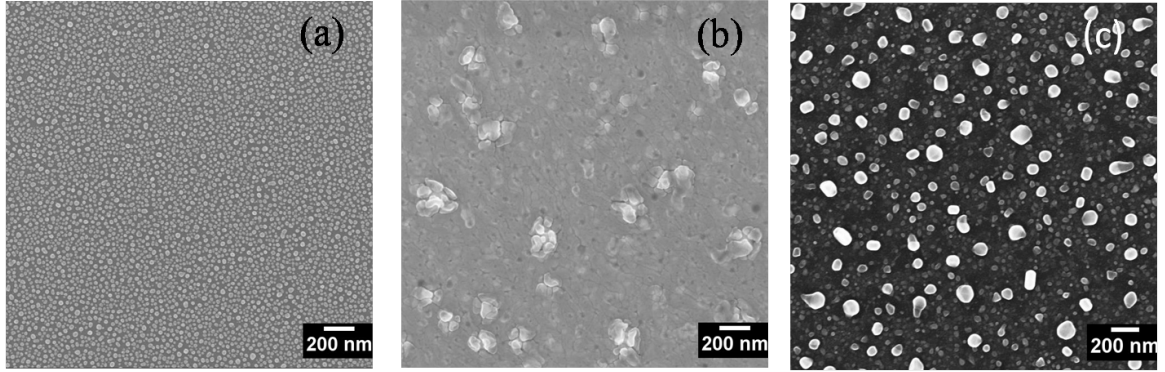
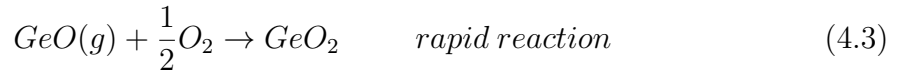


Figure 4.1: SEM Micrographs of 2 nm Ag /17 nm $\text{GeO}_x/\text{SiO}_x/\text{Si}(100)$ (a) As-deposited (b) Annealed in oxygen (c) Annealed in UHV at 800 °C for 30 minutes.

reactions: (a) formation of GeO_2 and (b) formation of volatile $\text{GeO}(g)$ from $\text{GeO}(s)$ which are slower reactions compared to the formation of GeO_2 from $\text{GeO}(g)$ [115]



From above reactions, it is clear that there won't be any GeO is available for disproportionate to produce Ge. Ge production is a key factor to enhance the possibility of desorption of native oxide as discussed in our earlier work [112]. In case of annealing under oxygen environment, there would be enhanced growth of SiO_x layer due to the availability of more oxygen which reduces the availability of atomic Si. Availability of atomic Si, Ge are the key factors for the enhanced desorption of SiO_x layer as explained by Yun et al., in terms of Ge and Si fluxes at 810 °C [117]. Due to the enhancement in the growth of the SiO_x layer, silver particles were embedded within this oxide layer. Under these annealing conditions, enhanced thickness occurs for GeO_x as well. It is found that that thickness of GeO_x was increased from 17 nm to 30 nm, while the SiO_x layer thickness was increased from 2 nm to 23 nm (Oxide layer thickness is considered from silicon interface). These values are determined by analyzing several cross-sectional TEM micrographs. Incorporation of oxygen into GeO_x film to form a stoichiometric GeO_2 might be a reason for the thickness increment whereas for SiO_x case, increase in the thickness due to silver particle embedding into the SiO_x

layer and also growth of SiO_2 (similar to dry oxidation process). In this process, there appear to have no availability of atomic germanium to initiate the enhanced desorption of the native oxide layer from the silicon substrate which could be crucial phase for the formation of endotaxial structures. In order to understand the role of atomic germanium availability to form endotaxial structures samples were annealed in lower oxygen partial pressures (viz in air, low vacuum and argon ambiances) compared to oxygen ambience.

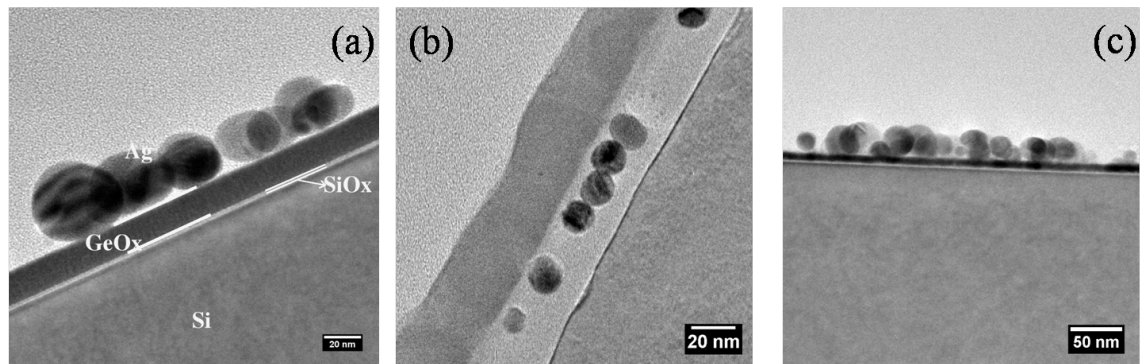


Figure 4.2: X-TEM Micrographs of 2 nm Ag /17 nm $\text{GeO}_x/\text{SiO}_x/ \text{Si}(100)$ (a) As-deposited (b) Annealed in oxygen (c) Annealed in UHV at 800 °C for 30 minutes.

Figure 4.1(c) is the SEM micrographs of the AGS annealed in UHV ambience showing the irregular shaped silver nanostructures. Figure 4.2(c) is the corresponding XTEM image revealing the formation of spherical silver particles on top of the substrate. From the figure 4.2(c), thickness of the SiO_x layer is measured 4 nm and the Ge layer thickness is 7 nm with polycrystalline in nature which can be observed from figure 4.3(a) and figure 4.3 (b) is the HR-XTEM image of the AGS annealed in UHV which is also complementing the SAED pattern result. From SAED pattern, polycrystalline rings were measured and the ring radii are 3.28 \AA , 2.02 \AA which corresponds Ge(111) and Ge(220) planes. From the HR-XTEM image, inter planar distance is measured as 3.28 \AA , which is matching with the Ge(111) planes within the error limit. The disproportionation reaction of GeO yields crystalline germanium after the temperature of 600 °C [116] which might be reason for the presence of polycrystalline germanium at the interface between silver nanostructures and SiO_x layer. In the chamber the

oxygen partial pressure is very low ($\approx 1 \times 10^{-10}$ mbar by considering working pressure as 5×10^{-9} mbar). Due to the nonavailability of enough oxygen to react with the Ge to form GeO the continuation of cyclic reaction could be broken leading to no desorption of SiO_x . Supply of atomic Si is also a key thing which is suppressed by the reduction of GeO_x i.e. GeO_x lose oxygen to silicon to form SiO_x layer [132]. Desorption of SiO_x layer is suppressed and acts as a barrier to Ag atoms to diffuse on to the SiO-Si interface. From above two ambience cases, it can be concluded that endotaxial structures cannot be formed where the presence of oxygen is either very high or very low.

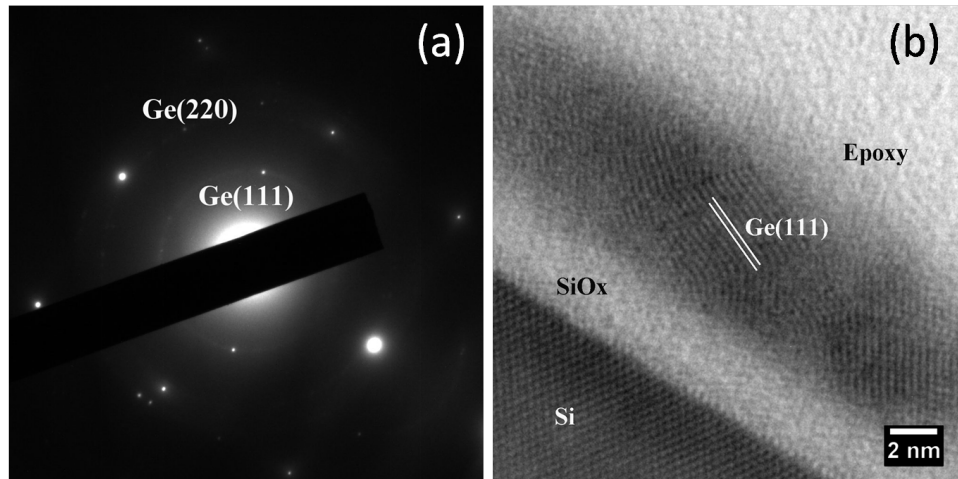


Figure 4.3: (a) SAED Pattern showing a polycrystalline rings of Ge, (b) HRX-TEM complementing the SAED result for 2 nm Ag /17 nm $\text{GeO}_x/\text{SiO}_x/$ Si(100) annealed at 800 °C in UHV

For the other ambience annealing conditions except oxygen, UHV ambience, silver endotaxial structures have been observed for AGS system annealed (for 30 minutes) at 800 °C. Figure 4.4 (a), (b) and (c) are the SEM Micrographs of AGS system annealed at 800 °C in air, low vacuum and Argon ambiances, respectively and these depict the formation of substrate symmetric silver nano square/rectangular structures. Figure 4.5 (a),(b) and (c) are the low magnification cross-sectional TEM (X-TEM) micrographs of AGS system at 800 °C in air, low vacuum and argon ambiances respectively, depicting the formation of endotaxial silver nano structures.

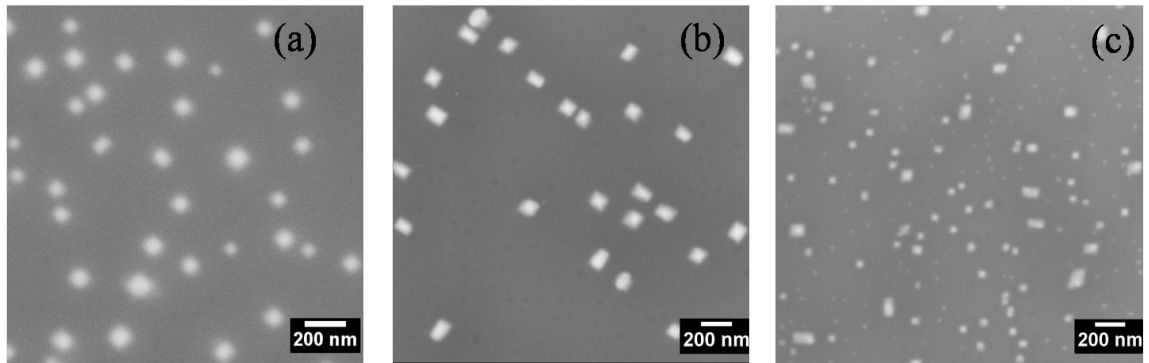


Figure 4.4: SEM Micrographs of 2 nm Ag/17 nm GeO_x/2 nm SiO_x/Si(100) (a) Annealed in air (b) Annealed in low vacuum. (c) Annealed in argon at 800 °C for 30 minutes.

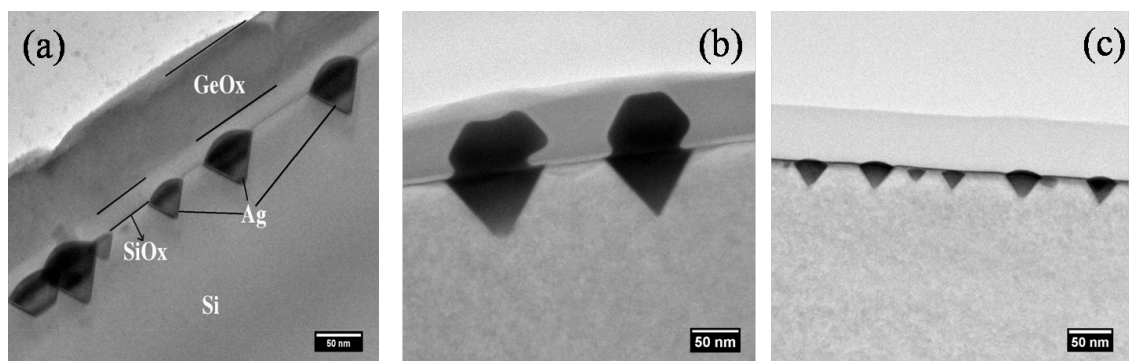


Figure 4.5: X-TEM Micrographs of 2 nm Ag/17 nm GeO_x/2 nm SiO_x/Si(100) (a) Annealed in air (b) Annealed in low vacuum. (c) Annealed in argon at 800 °C for 30 minutes.

Table 4.1: Details related to depth, height, coverage, oxide thickness, length, breadth and aspect ratio for endotaxial Silver nanostructures.

Ambience	Air	Argon	Low Vacuum
Depth (nm)	36 ± 8	27 ± 7	72 ± 7
Height (nm)	10 ± 5	—	67 ± 5
Coverage	9.3%	3.9 %	3.6 %
No. Of Oxides	2	—	2
GeO _x thickness (nm)	75 ± 12	—	65 ± 12
SiO _x thickness (nm)	20 ± 2	—	7 ± 1
Length (nm)	111 ± 22	100 ± 19	132 ± 16
Breadth (nm)	102 ± 17	93 ± 18	91 ± 12
Aspect Ratio	1.1	1.1	1.4

Interesting changes were observed in size, depth, height and surrounding media around the silver endotaxial nanostructures. Various parameters like length, breadth, depth and height that are tabulated in Table-4.1, are schematically shown in Figure 4.6. The details of coverage, no. of oxide layers present at the interface, height of the structures from the Si interface and depth of the structures (where depth is defined as the distance from Si interface to vertex of the cone) are given in detail in the table-4.1.

Mechanism for the formation of endotaxial nanostructures in above cases has been discussed in chapter 3 of this thesis [112]. But, the variation in the size and dimensions of the nanostructures can be observed for all three different ambiances. Considering the case of air and low vacuum annealing cases, these parameters are highly influenced by the oxygen partial pressure. In the case of annealing in air, the oxygen partial pressure is ≈ 212 mbar (assuming air pressure is 760 torr and the composition of air is 78% nitrogen and 20% of oxygen) where as the partial pressure of oxygen in the case of low vacuum is $\approx 1 \times 10^{-2}$ mbar (order of vacuum is $\approx 5 \times 10^{-2}$ and the composition is almost same as air). Partial pressures were calculated using Daltons Law. From the partial pressures of oxygen, it is clear that the availability of oxygen is more in the case of air annealing than in the case of low vacuum annealing, which plays a role in the SiO₂ formation and also in the disproportionation reaction where the generation of atomic or molecular Ge is taking place. More availability of atomic Ge is possible at lower oxygen partial pressures, which means desorption of SiO₂ is more compared to the formation of SiO₂ to allow the silver to diffuse through the

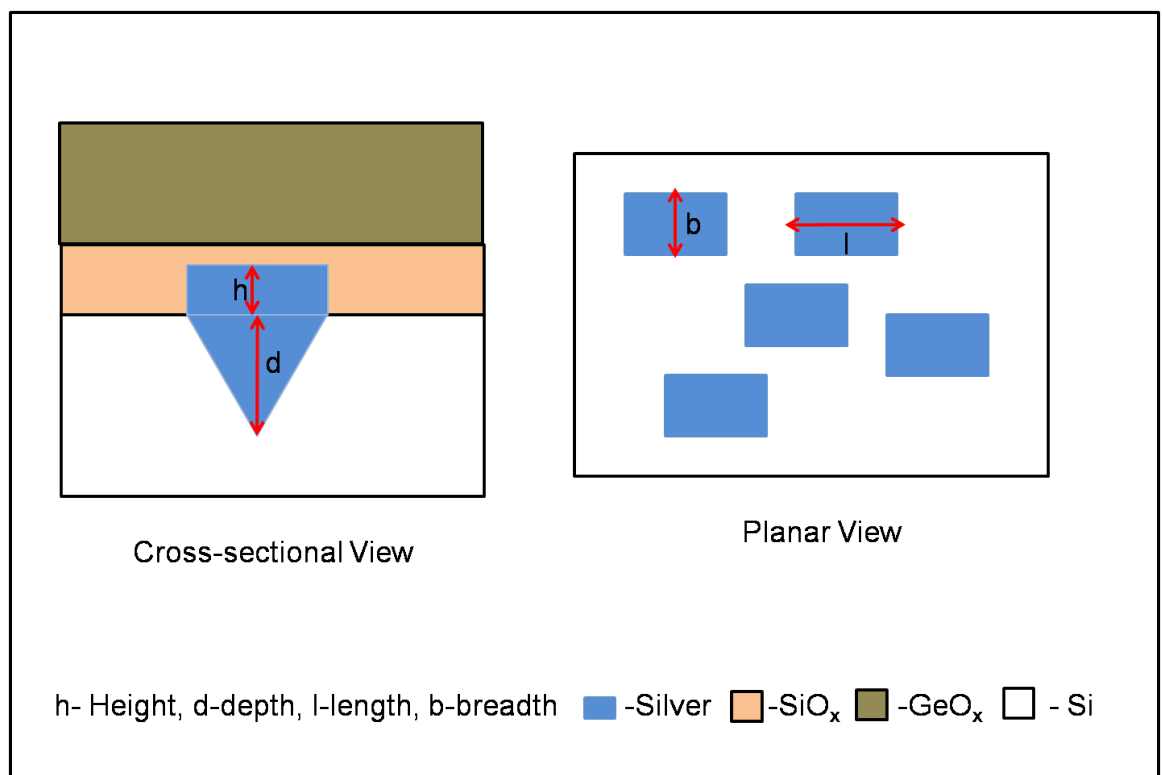


Figure 4.6: Schematic diagram explaining the consideration of height, depth, length and breadth of the silver endotaxial nanostructures.

layer into the substrate. From the above data, it is clear that a different dielectric media or the thickness of the dielectric media surrounding the nanostructures appears to vary as seen from the figure 4.5 (a), (b).

In case of annealing in argon flow, it is expected that volatile GeO and silver vapors would be carried out by the flow, resulting in the reduction of the amount of Ge and Ag. This is evident from the RBS spectrum of this sample shown in figure 4.7(b). The smallest size of endotaxial nanostructures (in terms of depth and height of the nanostructures) were obtained for argon flow annealing when compared to annealing in either low vacuum or air case. The width of the RBS spectrum (shown in figure 4.7(b) is much smaller than the other cases which confirms the lowest availability of silver).

Figure 4.7(a) is the RBS spectra of AGS as deposited sample which is fitted with SIMNRA software [95]. The parameters used for fitting are as follows: calibration parameters are 1.572 keV/channel and intercept of 121 eV. By fitting the RBS spectra of the AGS as-deposited sample using SIMNRA software, quantification of germanium and silver was evaluated. The germanium concentration in the GeO_x layer is 45% with an effective thickness of ≈ 120 ML (with a typical value of one ML $\approx 1 \times 10^{15}$ atoms/cm²) along with 55% oxygen content. The silver layer effective thickness was found to be 22 ML assuming the density of bulk silver. Figure 4.7 (b) shows comparative RBS spectra of the AGS system: for as-deposited sample, annealed at 800 °C in air, oxygen, low vacuum and argon ambiances. Figure 4.7 (c) shows the comparative peak positions of germanium and silver of AGS as-deposited and annealed in different ambient conditions. From RBS spectra of the as-deposited sample, the peaks of germanium (at energy ≈ 2414 keV) and silver (at energy ≈ 2590 keV) are well separated. Whereas in the case of AGS - at 800 °C annealed in air, the peaks of germanium and silver have overlapped with each other and the peak positions were calculated by deconvoluting the peaks which are at 2416 keV and 2526 keV, for Ge and Ag, respectively. From the sample AGS at 800 °C annealed in oxygen, the peaks of germanium and silver are also overlapped to a smaller extent and the peak positions were calculated by deconvolution of the peaks and these founded to be at 2413 keV and 2554 keV, respectively. For the case of AGS at 800 °C annealed in low vacuum, the peaks of germanium and silver are found overlap to smaller extent the

peak positions were calculated by deconvoluting the peaks which are at 2415 keV and 2584 keV. It is to be noted that when the annealing was done in Argon ambience, germanium is absent and only the silver peak is present at 2571 keV. In this case, the absence of germanium peak may be explained as the formation of volatile GeO (g) under the Ar flow would be pumped down away from the system.

When He⁺ ion penetrate through the GeO_x layer they lose energy which is denoted by dE/dx. The value of dE/dx = 284 eV/nm, for 3 MeV Helium ions in GeO₂ with density of 4.25gm/cm³ ($\frac{dE}{dx}$ value for SiO₂ is also approximately equal to GeO₂ value) which is calculated by using SRIM software [133]. The shift in the Ge peak position is ± 2 keV which corresponds to ≈ 4 nm thickness change in GeO_x (assuming it as GeO₂) layer with respect to as-deposited case. In the case of silver peak, a huge shift towards lower energy is observed in the case of air annealed system with an energy difference of 64 keV which corresponds to ≈ 110 nm depth with respect to as-deposited system's silver peak position. For this case the thickness of the top oxide layers was determined $\approx 95 \pm 12$ nm from TEM. For the case of oxygen annealed sample, the silver peak was shifted by an amount of 36 keV which corresponds to ≈ 63 nm, but from TEM the thickness of the oxide layers is found to be $\approx 42 \pm 5$ nm. For the case of low vacuum annealed case, the silver peak was shifted to 2584 keV from 2590 keV, with a shift of 6 keV corresponds to a thickness of ≈ 11 nm.

Synchrotron XRD measurements were done on AGS system as-deposited, annealed at 800 °C in air, argon and low vacuum samples to check the crystalline nature of the aforementioned silver endotaxial nanostructures and their orientation relationship with silicon. Figure 4.8 (a) is the XRD full scan of AGS system annealed in low vacuum revealing the peaks corresponding to Ag(002) at 15.48°, Si(004) at 23.65° and Ag(004) at 30.96° respectively, which confirms the formation of single crystalline silver endotaxial nanostructures whose orientation is parallel to the substrate orientation. Figure 4.8 (b) is a SAED pattern taken on a single silver endotaxial nanostructure which is indexed using the lattice spacing and angles between the spots, which confirm the single crystalline nature of endotaxial structures. This complements with XRD data as well. Figure 4.8 (c) is the comparative XRD spectrum of Ag(002), Ag(004) peaks of 2 nm Ag/ 17 nm GeO_x/SiO_x/Si(100) annealed at different ambiances (in air, argon and low vacuum). The normalized peak heights shown in figure 4.8 (c),

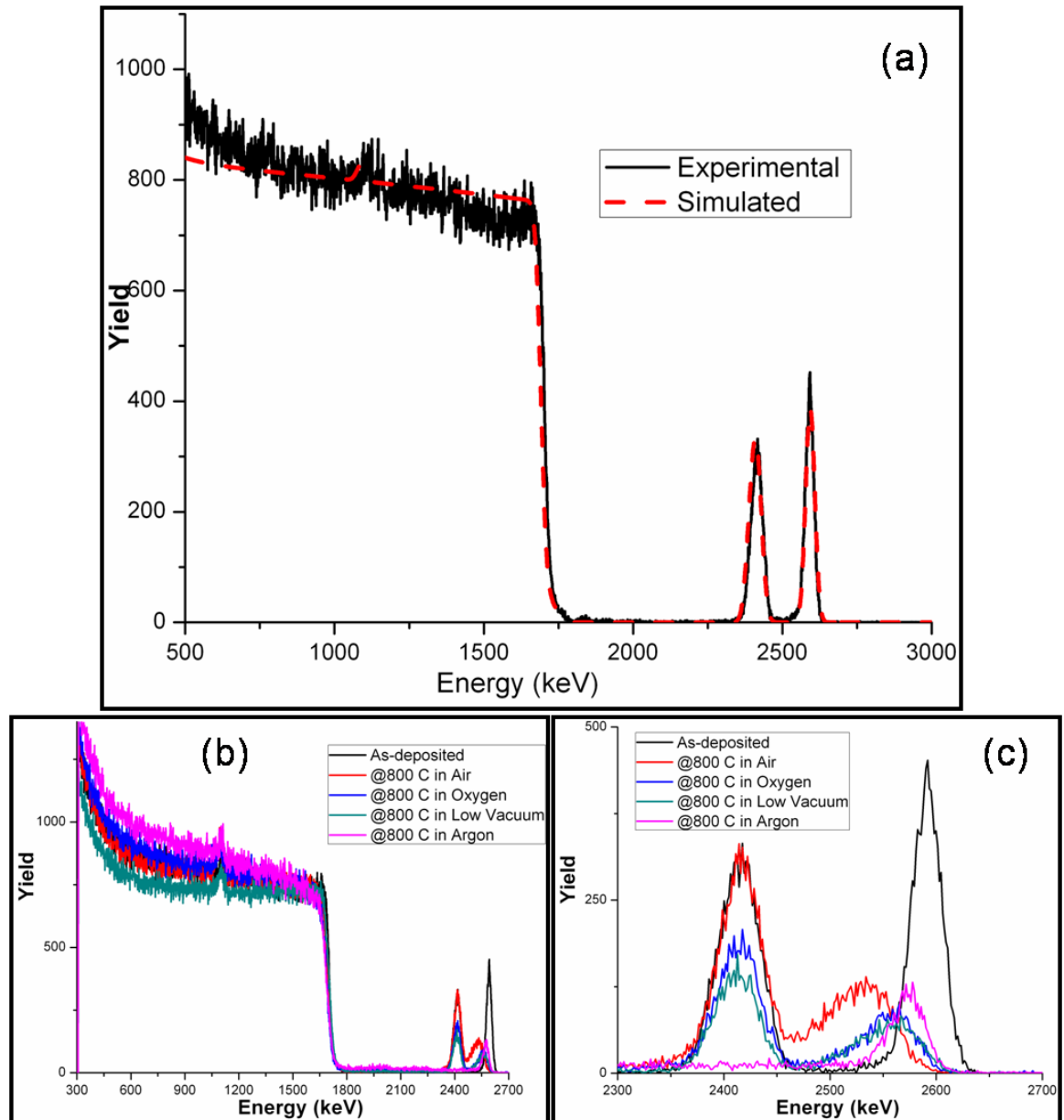


Figure 4.7: (a) RBS Spectra of experimental and simulated data of 2 nm Ag /17 nm $\text{GeO}_x/\text{SiO}_x/\text{Si}(100)$ as-deposited case, (b) comparative RBS spectrums of 2 nm Ag /17 nm $\text{GeO}_x/\text{SiO}_x/\text{Si}(100)$ as-deposited, Annealed in air, oxygen, low vacuum and argon at 800 °C for 30 minutes and (c) comparative peak positions of Ge and Ag of RBS spectrum.

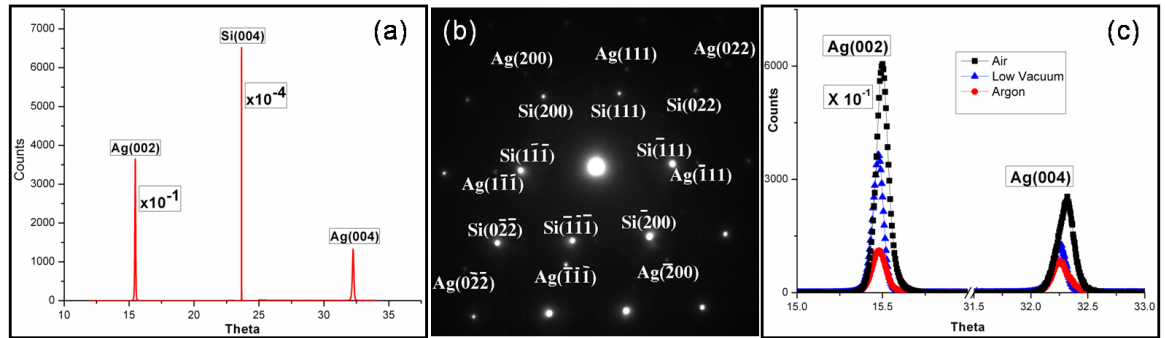


Figure 4.8: XRD spectrum of 2 nm Ag /17 nm $\text{GeO}_x/\text{SiO}_x/\text{Si}(100)$ annealed at 800 °C in low vacuum (b) SAED pattern taken on a single Ag nano structure for AGS-LV and (c) comparative HR-XRD spectrum of Ag(002), Ag(004) peaks for different ambiances.

further confirms lesser value of Ag concentration or effective thickness.

4.4 Chapter Summary

Silver endotaxial nanostructures with different size were synthesized in air, low vacuum and argon ambiances whereas embedded silver nanostructures were obtained for the case oxygen ambient. Endotaxial structures were not formed in either very high oxygen available ambience or very oxygen available ambience. Oxygen partial pressure plays a crucial role in the formation of endotaxial structure formation. In the case of endotaxial structures, changing the annealing ambient yielded to form Ag nanostructures at different depth inside the silicon and height above the silicon interface. Thickness of the oxide layers formation over these nanostructures was also changed under different ambient conditions. To understand the relative growth kinetics, *in-situ* XRD measurements would be presented.

Chapter 5

Real Time In-situ XRD Study of Endotaxial Growth of Ag Nanostructures in Silicon

5.1 Introduction

In this chapter, *in-situ* study of the 4 nm Ag/17 nm GeO_x/SiO_x/Si annealed in air ambient case will be discussed along with the role of surface and interfacial energies in the formation of these endotaxial structures.

A self-assembly process is promising for future nanostructure systems [134]. Understanding of self-assembly is very important which can be understood by understanding the role of energetics during the process. In-situ characterization is a powerful tool to understand the processes while they are happening. During the crystal growth, in-situ XRD study gives very useful information related to strain, growth direction of the crystal and epitaxial information in the case of two different materials. In this report, we are reporting the interplay of surface energy and interface energy of metal silicon system at high temperatures during the growth of metal endotaxial structures on silicon substrate at atmospheric conditions using an intermediate GeO_x etchant layer. Theoretically, Xin et. al have calculated the interface energies of Ag/Si twisted interfaces and found that Ag(111)/Si(111) interface have lowest energy at a twist angle of 30° [120]. But in our experiments, we found that Ag(111)/Si(111) interface formed without any twist angle or at a twist angle of 0°. In order to generalize

the mechanism of endotaxial nanostructures formation with the aid of GeO_x etchant layer at atmospheric conditions, Au endotaxial nanostructures were also synthesized by following the same method at 800 °C. But for the gold endotaxial nanostructures the thickness of the etchant layer is less compared to the synthesis of silver endotaxial nanostructures [112, 135]. The importance of the study of surface and interface phenomena has been steadily increasing and now constitutes one of the most significant aspects of the semiconductor industry. Knowledge of surface properties of Si, Ge and Ag nanostructures are crucial for rapidly developing area of nanotechnology. Metal nanoparticles on semiconductor substrate, facilitates to exploit the nanoparticle properties and to fabricate novel and larger integrated devices. Metal nanoparticles exhibit unique electronic, magnetic, photonic and catalytic properties which can be employed for the preparation of new materials for energy storage, photonics, communications, and sensing applications [136, 137]. For example, metal over layers have been exploited to tune the characteristics of epitaxial islands/quantum dots, including their size, density and shape [138, 139]. In this chapter we are discussing about the play of interfacial and surface energies during the growth of silver endotaxial nanostructures observed in-situ by XRD measurements.

5.2 Experimental details

Silicon (100), (110), (111) orientations wafers were cleaned by standard procedure of rinsing with alcohol and de-ionized water. Deposition of germanium was done by physical vapor deposition (PVD) system. We have used crystalline Ge wafer and Ge powder, as a source material for deposition. It appears that a GeO_x film was grown instead of pure Ge. This could be due to the vacuum environment in the high vacuum deposition system. In this process, a ≈ 17 nm GeO_x was deposited on Silicon samples. Following this a ~ 4 nm Ag film was deposited using Molecular beam Epitaxy (MBE) system. Annealing of the samples was done in-situ using a heating stage (M/s. Anton Paar, Austria) at Photon Factory, KEK, Japan. The wave length of the X-rays used for the experiment is 1.089 Å and the experimental geometry is reflection geometry with θ - 2θ scanning mode. Scheme 5.1 shows the schematic diagram of experimental geometry.

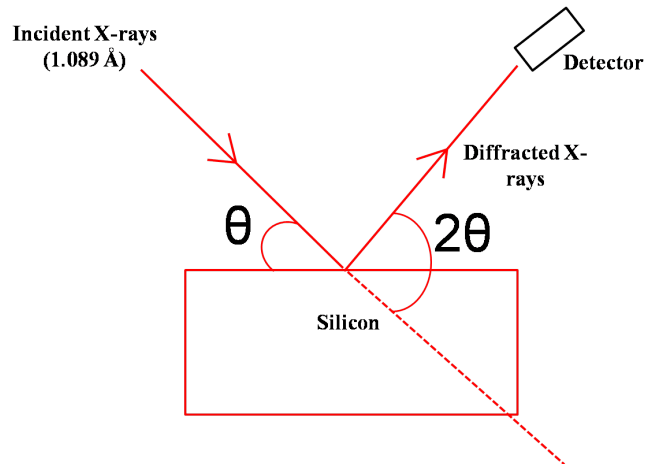


Figure 5.1: Schematic diagram of the experimental geometry used to perform the *in-situ* annealing of the samples at Photon factory, KEK, Japan.

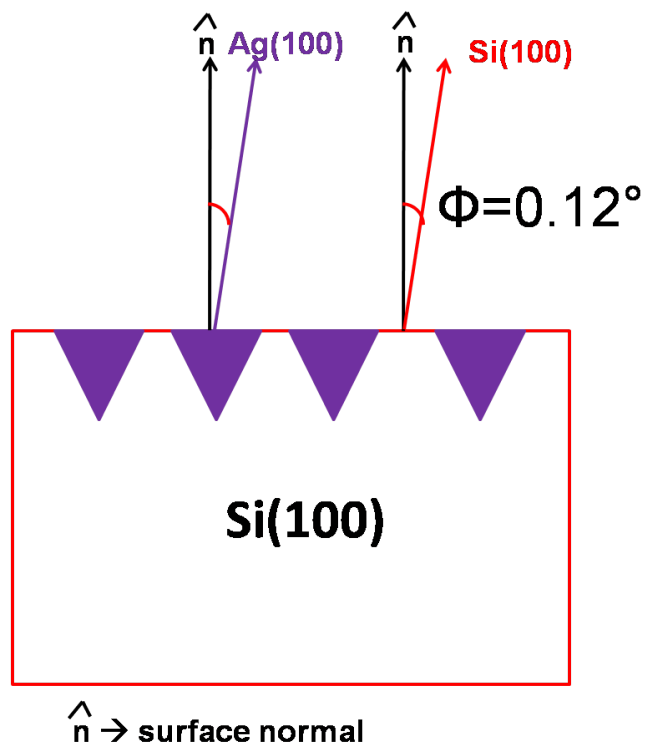


Figure 5.2: Schematic diagram showing the relation between the axes of silver and silicon crystals along with the surface normal of the corresponding substrate.

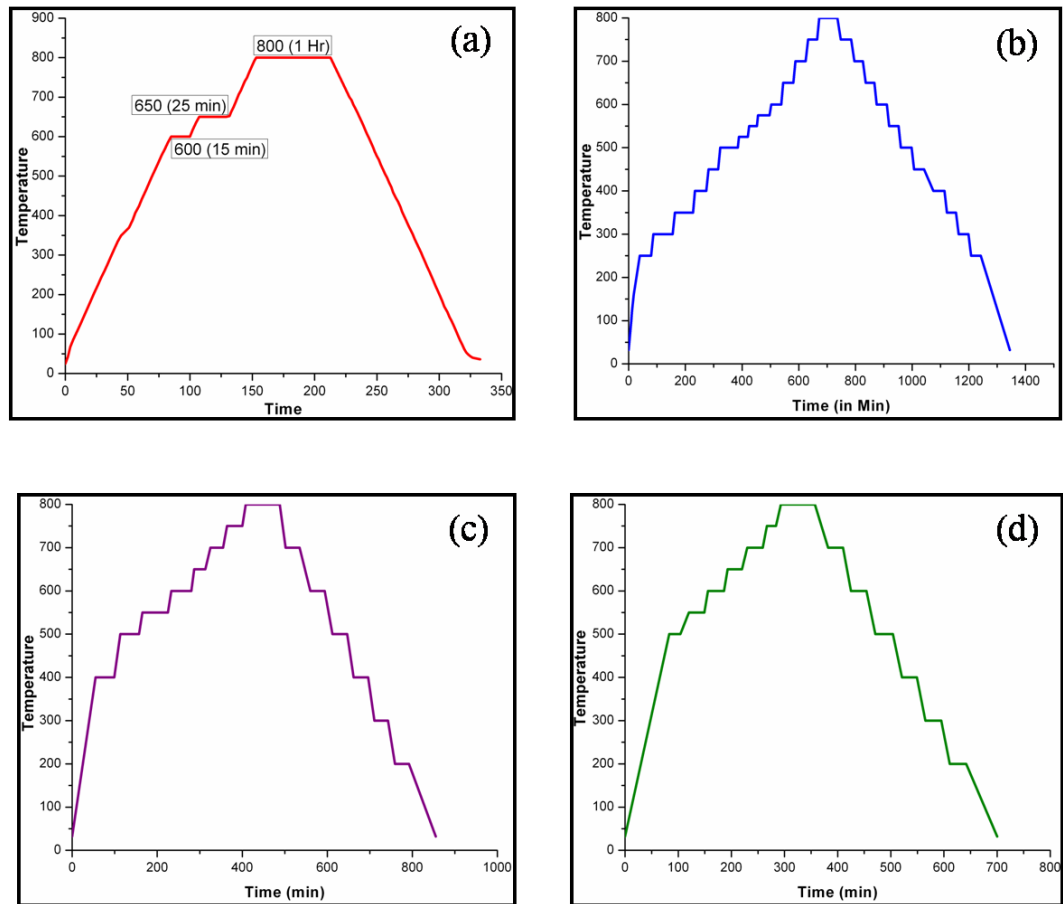


Figure 5.3: Schematic diagram of the experimental procedure followed during in-situ annealing and cooling of (a) 4 nm Ag/ 17 nm $\text{GeO}_x/\text{SiO}_2/\text{Si}(100)$ sample continuous ramping for heating and cooling (Numbers in the paranthesis denotes the time for which the specimen has been kept at that temperature)(b) 4 nm Ag/ 17 nm $\text{GeO}_x/\text{SiO}_2/\text{Si}(100)$ sample's stepwise annealing and stepwise cooling, (c) 4 nm Ag/ 17 nm $\text{GeO}_x/\text{SiO}_2/\text{Si}(110)$ sample's stepwise annealing and stepwise cooling and (d) 4 nm Ag/ 17 nm $\text{GeO}_x/\text{SiO}_2/\text{Si}(111)$ sample's stepwise annealing and stepwise cooling. At each step sample was kept for 10 minutes for achieving equilibrium and then the XRD measurements were taken.

Before annealing, X-ray diffraction (XRD) measurements were taken on the as-deposited sample. Annealing was done with a ramping rate of 7 °C/minute and XRD spectra were collected continuously. A schematic was presented in figure 5.3 that explains the annealing and cooling procedures followed during the real time XRD measurements.

5.3 Results and discussion

4 nm Ag/17 nm GeO_x/SiO_x/Si(100) sample was annealed in air with a ramp rate of 7 °C/min. During annealing, XRD spectra for Ag(002) were recorded continuously with increment of temperature. Upto 650 °C, no peak was observed for Ag(002). At 650 °C, a small peak was observed at a θ of 15.28° which corresponds to Ag(002). Figure 5.4(a) is the peak area plot of Ag(002) peak versus temperature showing increment of intensity, the corresponding schematic process is represented in figure 5.3 (a). The peak intensity is more or less constant upto 750 °C, after arriving 750 °C step increment in the peak area has been observed. After reaching 800 °C, sample was kept for one hour to observe the change in peak area of Ag(002) with respect to time. Figure 5.4 (b) is the plot of Ag(002) peak area versus stabilization time. From figure 5.4 (b), increment of peak area is observed up to 1500 seconds and afterwards it is more or less constant. This curve was fitted with an exponential decay function of the form $A e^{(-x/t)} + y$, where A, y, t are the constants and the fitted values are -415, 452, 1159 respectively.

During the cooling, XRD spectra were also recorded. During the cooling of the sample, peak position of Ag(002) is shifting towards higher angles implies the contraction of lattice constant due to the cooling. The shift in the peak position was plotted with respect to cooling temperature and shown in figure 5.4 (c). Lattice constant was calculated for the peak position plotted in figure 5.4 (c) at each temperature by using Bragg's equation. θ is increasing with decrement in the temperature as shown in figure 5.4 (d) which is due to decrease in the lattice constant a . Lattice constant a is inversely proportional to $\sin\theta$ or θ . Thermal expansion of silver might be the reason for shifting the peak position of Ag(002) peak during the cooling which can be calculated theoretically using the thermal expansion coefficient α and the temperature difference ΔT . So, lattice constant was calculated at each temperature by taking

thermal expansion of bulk silver into account. Lattice constant a_T at temperature T is

$$a_T = a_0(1 + \alpha\Delta T)$$

where $a_0 = 4.085$ Å lattice constant of silver at room temperature (i.e. at 27 °C), $\alpha = 19.6 \times 10^{-6}$ thermal expansion coefficient of bulk silver [140] and $\Delta T = T - 27$ temperature difference. Figure 5.4 (d) is the plot of lattice constant at each temperature determined experimentally using the data (figure 5.4(c)) versus cooling temperature, and also theoretically calculated values with respect to cooling temperature. From figure 5.4 (d), it is clear that, the lattice constant coincide to the bulk lattice constant, below 400 °C while at higher temperatures, a deviation occurs. This could be due to the fact that α is different for nanostructures that are being embedded in Si.

During annealing of fcc metals, the surface tries to minimize its surface energy, and the lowest surface energy for a fcc metal is for (111) facet and the order of surface energies for low index planes of fcc materials is as follows: $E_{(111)} < E_{(100)} < E_{(110)}$ [141]. In order to understand the role of surface energy in the formation of endotaxial structures, a controlled experiment was performed. The experimental procedure was schematically shown in scheme 5.3(b). This time XRD measurements were taken for all the three low index planes viz. (111), (100) and (110) at each temperature with an interval of 50°C after a stabilization time of 10 minutes. Once the temperature was stabilized at a given temperature, XRD for (111), (110), (100) facets has been carried out; one after the other before raising to next temperature. Upto 500 °C, no peaks were observed. At 500 °C, Ag(111) peak started appearing at angle 13.23°. The peak intensity of Ag(111) peak grew with increment in the annealing temperature upto 700 °C and beyond 700 °C the peak intensity got reduced. At 800 °C, after completion of one hour stabilization time Ag(111) peak intensity becomes zero. Evolution of Ag (111) peak with respect to temperature was shown in figure 5.5 (b) with square points. Evolution of Ag(200) peak was started at 575 °C and its intensity increased with annealing temperature. At 700 °C, Ag(002) peak intensity become larger than the Ag(111) peak intensity. Figure 5.5 (a) is the 3D plot of Ag(111) and Ag(200) peaks with respect to annealing temperature and figure 5.5 (b) is the plot of peak areas of Ag(111), Ag(200) peaks. After 700 °C, Ag(002) peak intensity increases by the expense of Ag(111) peak intensity. It is expected to happen the following reaction

at 750 °C:

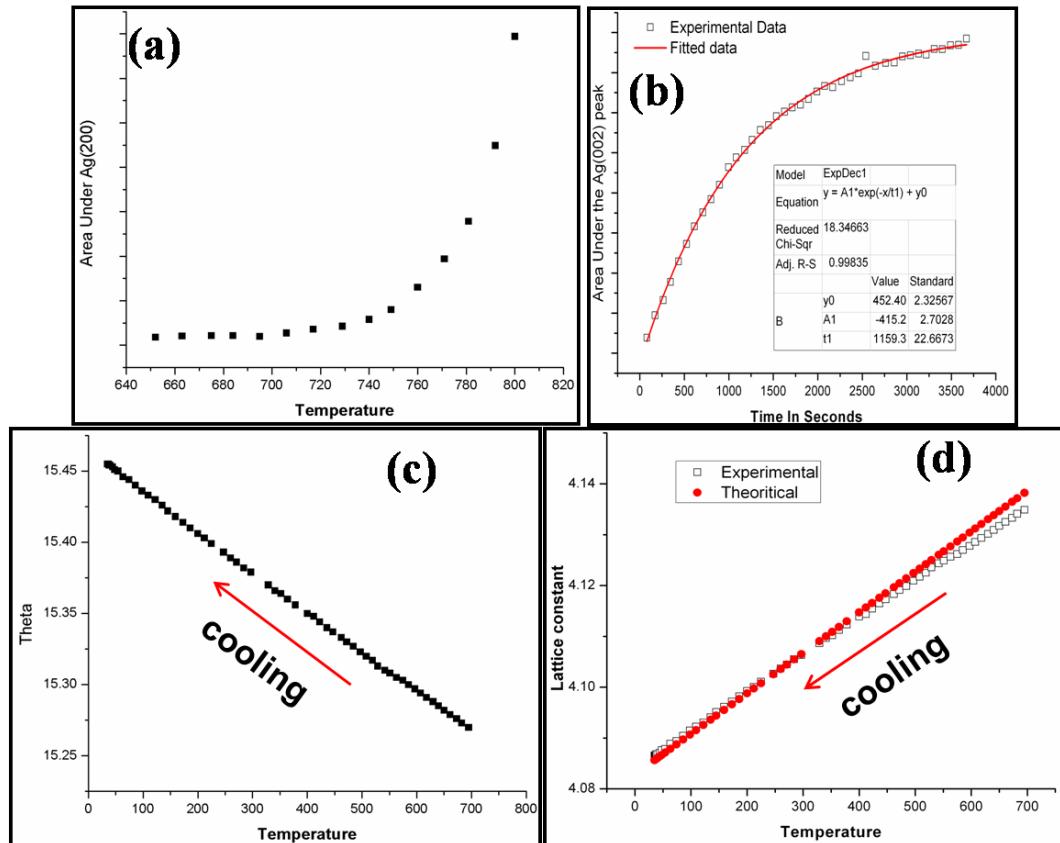


Figure 5.4: (a) Plot of peak areas of HR-XRD spectrum of Ag(002) peaks of 4 nm Ag/17 nm GeO_x/SiO_x/ Si(100) annealed in-situ up to 800 °C in air with respect to temperature increment, (b) plot of Ag(002) peak area with respect to stabilization time at 800 °C. (c) Plot of Ag(002) peak position shift (d) calculated lattice constants corresponding to the Ag(002) peak shift and theoretical fitting using thermal expansion of silver during the cooling of 4 nm Ag/17 nm GeO_x/SiO_x/ Si(100) annealed in-situ up to 800 °C in air.

During annealing, supply of silicon atoms for the above reaction to occur will come from the substrate. Removal of silicon atoms along (111) plane is easier than other facet orientations and these Si atoms are expected to participate the reaction. In this case, interfacial energy is also comes into picture and there will be a competition between surface and interface energy minimization. As silver substitutes the silicon atoms along (111) direction and try to form an interface as Ag(111)/Si(111) to minimize the interface energy. In our previous work, it is already proved that

the Ag(111)/Si(111) interfaces formed with a twist angle of zero in the endotaxial structures formed after cooling. As (100) facet is the second lowest surface energy facet and this facet was observed at the top of the interface. This structure is the equilibrium structure as per Wulff's construction [121]. Figure 5.5(c) is a plot of ratio of intensity of Ag(002) to Ag(111) reflection and the plot is fitted with the exponential growth function. From figure 5.5(c), one can observe that the peak intensity of Ag(111) is decreasing exponentially with respect to Ag(002) intensity and they have about equal intensities at 606 °C (from the fitting). However, the role of interface energy with respect to temperature is not clear because the surface free energies of (111), (100) are the lowest compared to (110). More systematic experimental studies and theoretical calculations are needed.

In order to understand the role of interface at increasing thermal energy (i.e. at higher temperatures), a 4 nm Ag/17 nm GeO_x/SiO_x/ Si(110) sample was annealed in air as shown in schematic 5.3 (c). Figure 5.6 (a) shows the XRD of Ag(111) peak of the sample, 4 nm Ag/17 nm GeO_x/SiO_x/ Si(110) annealed at 800 °C in air, at 550 °C along with the Ag(002) reflection as shown in figure 5.6(b). Around 650 °C, Ag(220) peak started evaluating from the substrate was observed due to the substrate orientation. After 650 °C, Ag(220) peak intensity was increased rapidly and the peak evaluation with respect to temperature has been shown in figure 5.6 (c).

Further, annealing process depicted in figure 5.3 (d) has been carried out for 4 nm Ag/17 nm GeO_x/SiO_x//Si(111) annealed in air. Figure 5.7 (a) shows the 3D plot of Ag(111) peak of the sample 4 nm Ag/17 nm GeO_x/SiO_x/ Si(111) that was annealed at 800 °C in air. This peak starts around 550 °C and the peak area under the Ag(111) peak was plotted with respect to temperature as shown in figure 5.7(b). From this, it is obvious that the (111) peak intensity is rapidly increased beyond 650 °C, which is similar to above two cases.

5.4 Chapter Summary

Understanding of the role of surface and interfacial energy in the growth of endotaxial metal nanostructures on silicon substrate at atmospheric conditions using GeO_x

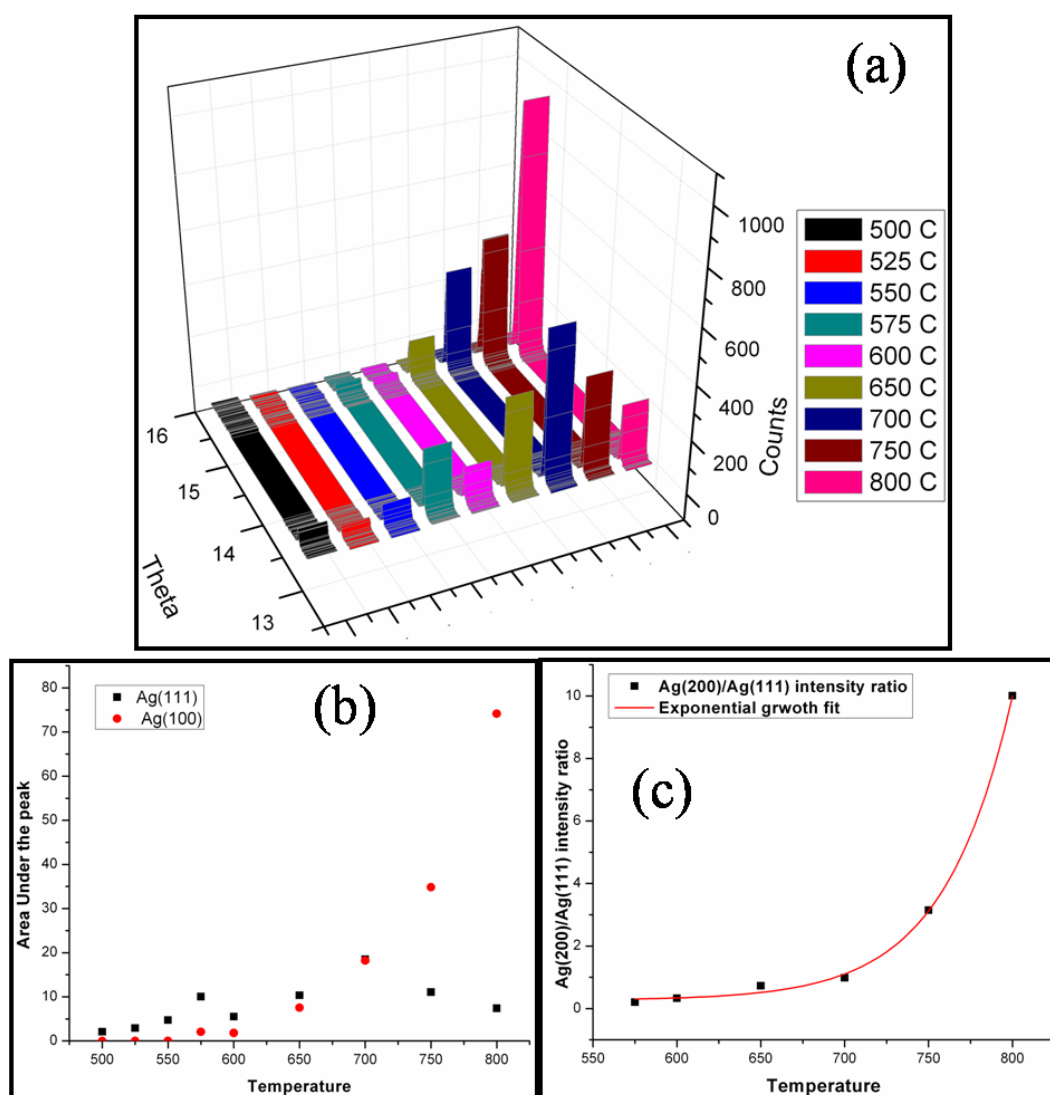


Figure 5.5: (a) 3D plot of Ag(111) and Ag(002) peaks (b) plot of Ag(111) and Ag(002) peak areas with respect to temperature during the annealing of 4 nm Ag/17 nm GeO_x/SiO_x/ Si(100) in-situ up to 800 °C in air (c) plot of intensity ratio of Ag(200) to Ag(111) with respect to temperature.

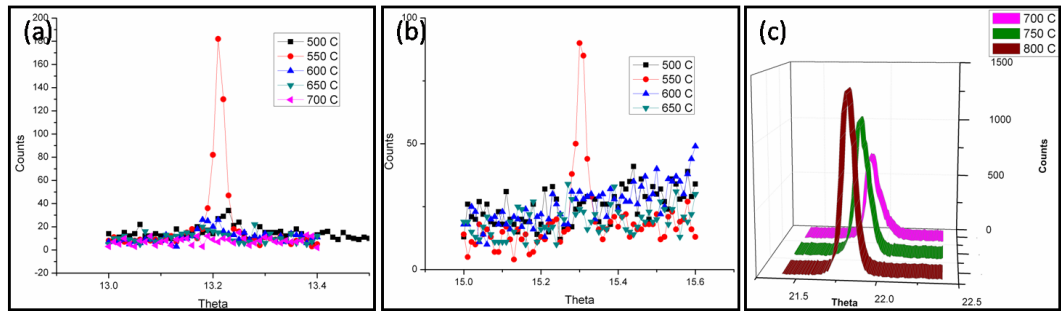


Figure 5.6: Peak evolution of (a) Ag(111) (b) Ag(002) peaks and (c) 3D plot of Ag(220) with respect to increasing temperature during the annealing of 4 nm Ag/17 nm $\text{GeO}_x/\text{SiO}_x/\text{Si}(110)$ in-situ up to 800 °C in air.

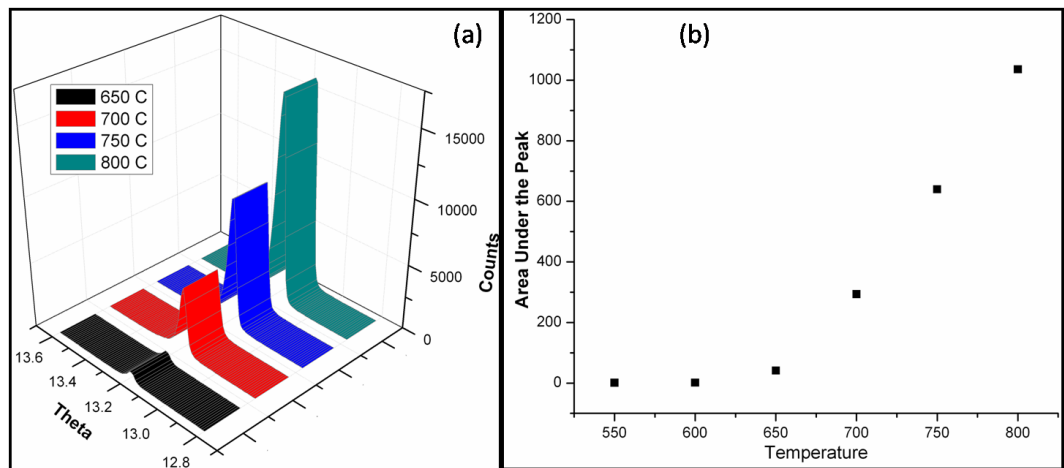


Figure 5.7: (a) 3D plot of Ag(111) peak (b) Plot of Ag(111) peak areas with respect to temperature during the annealing of 4 nm Ag/17 nm $\text{GeO}_x/\text{SiO}_x/\text{Si}(111)$ in-situ up to 800 °C in air.

layer as an etchant. Interface energy is playing a crucial role in the formation of these endotaxial structures and it is come into picture around 650 °C. In the case of Si(100) substrate, Ag(002) peak grows by the expense of Ag(111).

Chapter 6

Effect of GeO_x Thickness and Annealing Temperatures on Ag Endotaxial Nanostructures

6.1 Introduction

Formation of silver endotaxial nanostructures in silicon substrate and the role of GeO_x presence and position along with annealing ambiance dependence was discussed in earlier chapters. In this chapter the effect of annealing temperature and GeO_x thickness dependence on the formation of silver endotaxial nanostructures will be discussed. It is known that metallic particles such as gold nanorods [142] or silver nanorods [143] or silver nanodiscs [144] exhibit anisotropic optical properties that are directly related to their aspect ratio. Not only the size of the particles but also the shape and the dielectric media around the particles also effects their properties especially in optical properties. Light is trapped on the metal coated surfaces in the form of surface plasmons. These surface plasmons of the metal nanoparticles' absorption or scattering is a recent approach to enhance the silicon solar cell efficiency [145, 146]. Scattering phenomenon appeared to be advantageous for Si based solar cells whereas for organic solar cells absorption is beneficial [42].

In order to control the shape and size of the nanoparticles during synthesis is a challenging work. Several groups have reported the synthesis of different shapes of nanoparticles by chemical methods like solvothermal [147–149], hydrothermal [150]

and redox [151] reactions. Self assembly is one of the way to synthesis nanoparticles. In self assembly method initial conditions or parameters like temperature [152], thickness of the film, annealing ambient [153] and substrate orientation are governing factors to control the shape, size and dielectric media around the nanoparticles. In this chapter we are discussing about the effect of annealing temperature and the initial thickness of GeO_x on the formation of metal endotaxial nanostructures in silicon substrate.

6.2 Experimental details

Si(100) wafers were cleaned by standard procedure of rinsing with alcohol and deionized water. Deposition of Germania, silver and gold was done by physical vapor deposition (PVD) system as discussed earlier. Three values of thicknesses were used for GeO_x: ≈ 5 nm, ≈ 17 nm and ≈ 60 nm. On these substrates, a 2 nm Ag was deposited using PVD technique. Similarly, a 2 nm Au was deposited on 5 nm GeO_x/SiO_x/Si(100), 17 nm GeO_x/SiO_x/Si(100) samples to try for endotaxial Au nanostructures. For temperature dependent study, 2 nm Ag/17 nm GeO_x/SiO_x/Si(100) were considered and annealed at 700 °C, 750 °C and 800 °C in air. In an effort to understand the role of GeO_x thickness in the formation of Ag endotaxial structures, 2 nm Ag/5 nm GeO_x/SiO_x/Si(100), 2 nm Ag/17 nm GeO_x/SiO_x/Si(100) and 2 nm Ag/60 nm GeO_x/SiO_x/Si(100) samples were annealed up to 800 °C in air. Similarly, 2 nm Au/5 nm GeO_x/SiO_x/Si(100) and 2 nm Au/17 nm GeO_x/SiO_x/Si(100) samples are also annealed at 800 °C in air to study the growth of Au endotaxial nanostructures in Si and dependence of GeO_x thickness in the formation of endotaxial nanostructures. Scanning electron microscopy (SEM), transmission electron microscopy, x-ray diffraction and Rutherford backscattering spectrometry techniques were employed to elucidate the results.

6.3 Results and discussion

6.3.1 Temperature Dependent Study

Figure 6.1(a) depicts a SEM micrograph of 2 nm Ag/17 nm $\text{GeO}_x/\text{SiO}_x/\text{Si}(100)$ annealed up to 700 °C in air revealing the nanostructures formation. The structures appears to have no substrate symmetry. Figure 6.2 (a) is the corresponding low

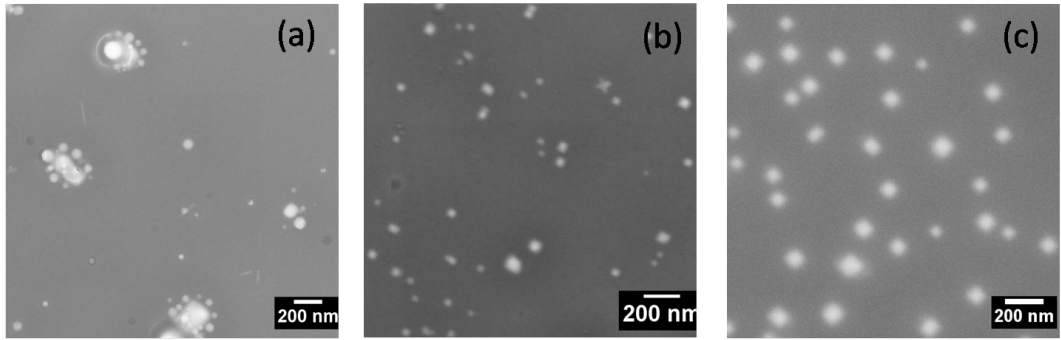


Figure 6.1: SEM micrographs of 2 nm Ag/17 nm $\text{GeO}_x/\text{SiO}_x/\text{Si}(100)$ annealed at different temperatures in air (a) 700 °C (b) 750 °C (c) 800 °C

magnification X-TEM image of the 2 nm Ag/17 nm $\text{GeO}_x/\text{SiO}_x/\text{Si}(100)$ annealed up to 700 °C in air revealing the embedding of silver into silicon the shape of the nanoparticles is spherical. From this micrograph, the thickness of the top oxide layers is measured and the values are for GeO_x layer is ≈ 32 nm and for SiO_x layer is ≈ 4 nm. Figure 6.2 (b) is the HR-X-TEM micrograph of one of the embedded silver nanostructure in silicon substrate. Figure 6.2 (c) is the SAED pattern taken on the single structure showing the dominant Ag(111) single crystalline reflection and no other reflections were found. From the above results 700 °C annealing temperature is not optimal for getting endotaxial structures in the case of 2 nm Ag/17 nm $\text{GeO}_x/\text{SiO}_x/\text{Si}(100)$ sample.

Figure 6.1(b) depicts a SEM micrograph of 2 nm Ag/17 nm $\text{GeO}_x/\text{SiO}_x/\text{Si}(100)$ annealed up to 750 °C in air revealing the substrate symmetric silver nanostructures formation with a coverage of 3.6 %. Figure 6.3 (a) is the corresponding low magnification X-TEM image of the 2 nm Ag/17 nm $\text{GeO}_x/\text{SiO}_x/\text{Si}(100)$ annealed up to 750 °C in air revealing the embedding of silver into silicon and formation of endotaxial nanostructures along with some structures which are still under formation. In this

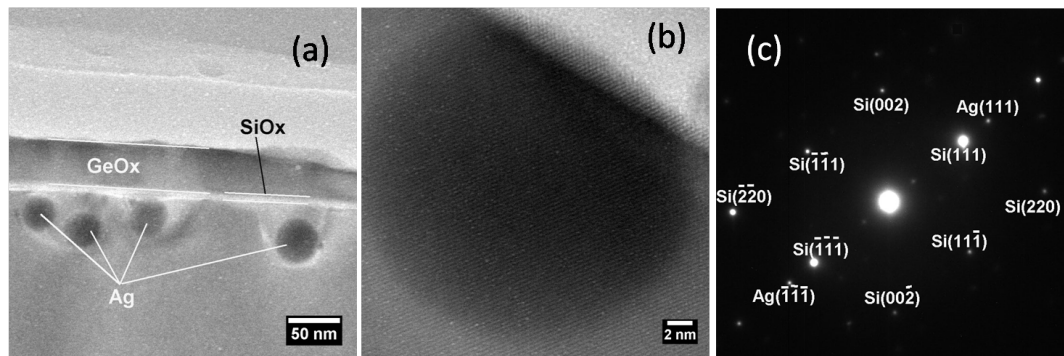


Figure 6.2: X-TEM Micrographs of 2 nm Ag/17 nm $\text{GeO}_x/\text{SiO}_x/\text{Si}(100)$ annealed up to 700 °C in air (a) Low Mag (b) HR-X-TEM depicts silver nanostructures and (c) Diffraction pattern from a single structure

case the thickness of the GeO_x layer is measured as ≈ 23 nm and SiO_x layer thickness is measured as ≈ 20 nm. Increment of SiO_x layer thickness was observed and reduction in the GeO_x layer thickness was also observed for this case compared to 700 °C case. Figure 6.3 (b) is the HR-X-TEM micrograph of top of the embedded silver nanostructure in silicon substrate revealing the Ag(111) facet on the particle. Figure 6.3 (c) is the SAED pattern taken on the single structure showing the dominant Ag(111) single crystalline reflection and no other reflections were found. In this case some endotaxial structures were found but those are not prominent and they are mixed with some spherical silver nanoparticles. But this annealing temperatures is also not suitable to get well oriented substrate symmetric silver endotaxial nanostructures.

Figure 6.1(c) depicts a SEM micrograph of 2 nm Ag/17 nm $\text{GeO}_x/\text{SiO}_x/\text{Si}(100)$ annealed up to 800 °C in air revealing the substrate symmetric silver nanostructures formation with a coverage of 9.3 %. Figure 6.4 (a) is the low magnification cross-sectional TEM micrograph revealing the embedding of silver into silicon. From this figure 6.4 (a), thickness of the top oxide layers were measured as 70 nm for GeO_x layer and 25 nm for SiO_x layer. Figure 6.4 (b) is the HR-X-TEM micrograph of top of the embedded silver nanostructure in silicon substrate revealing the Ag(111) planes on the nanostructure which are parallel to the Si(111) planes of the substrate and revealing the formation of endotaxial nanostructures. Figure 6.4 (c) is the SAED pattern taken on the single structure showing the diffraction spots of the nanostructure are

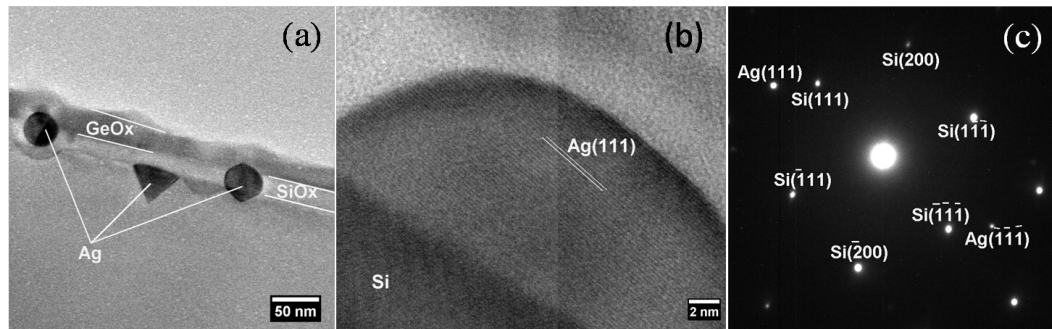


Figure 6.3: X-TEM Micrographs of 2 nm Ag/17 nm $\text{GeO}_x/\text{SiO}_x/\text{Si}(100)$ annealed up to 750 °C in air (a) Low Mag (b) HR-X-TEM depicts silver nanostructures and (c) Diffraction pattern from a single structure

following the symmetry of the Si substrate and the orientation of the nanostructure interface is exactly parallel with the substrate. For this sample, most of the embedded Ag structures have been found to be of endotaxial type.

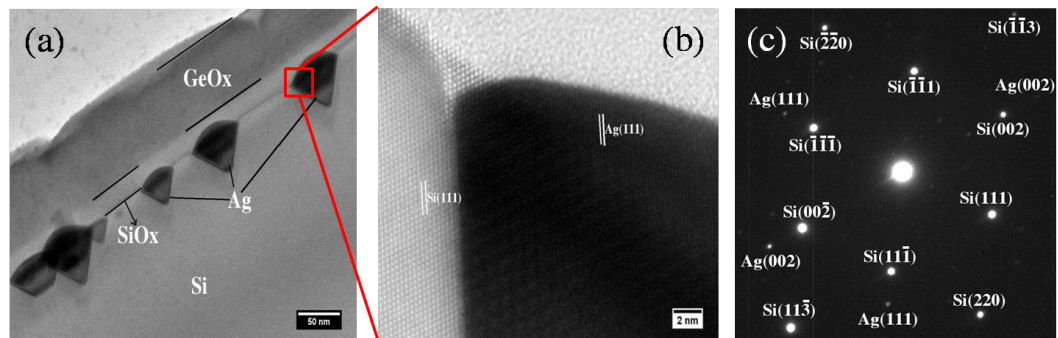


Figure 6.4: X-TEM Micrographs of 2 nm Ag/17 nm $\text{GeO}_x/\text{SiO}_x/\text{Si}(100)$ at 800 °C annealed in air (a) Low Mag (b) HR-X-TEM depicts endotaxial structures (with Moiré fringes) and (c) Diffraction pattern from a single structure

Rutherford backscattering spectrometry (RBS) has been performed on these samples to understand the diffusion of silver into the silicon substrate to complement the TEM results. Figure 6.5 (a) is the image showing a comparative plot of the RBS spectra of as deposited, 700 °C, 750 °C and 800 °C annealed in air spectra. Figure 6.5 (b) is the plot of Ge, Ag peaks obtained in the RBS to understand the diffusion of Ag and Ge. For the case of 2 nm Ag/17 nm $\text{GeO}_x/\text{SiO}_x/\text{Si}(100)$ as deposited sample, Ge peak

was observed at 2414 keV and Ag peak was observed at 2590 keV. For 2 nm Ag/17 nm $GeO_x/SiO_x/Si(100)$ annealed at 700 °C in air case the Ge peak was observed at an energy of 2414 keV which is similar to as deposited case but the silver peak was observed at 2535 keV with a shift of 55 keV towards low energy side indicating the silver inter diffusion in to the substrate compared to as deposited case which is complementing with X-TEM results as silver was observed within the Si substrate. 2 nm Ag/17 nm $GeO_x/SiO_x/Si(100)$ annealed at 750 °C in air case the Ge peak was observed at an energy of 2416 keV which is shifted towards higher energy side as compared to as deposited sample. The silver peak was observed at an energy of 2551 keV which is 39 keV lesser to as deposited case. From the figure 6.5, reduction in the intensity of Ge peak can be observed for the sample annealed at 750 °C case, which is complementing with X-TEM result (figure 6.3) where the thickness of the GeO_x layer comes as 23 nm. Whereas in the case of 2 nm Ag/17 nm $GeO_x/SiO_x/Si(100)$ at 800 °C annealed in air, the peaks of germanium and silver have overlapped with each other and the peak positions were calculated by deconvolution of the peaks which are at 2416 keV and 2526 keV, for Ge and Ag, respectively.

The shift in the silver peak can be used to determine the inter diffusion length of silver as compared to its as-deposited case by using the energy loss of He^+ ions through the oxide layers or material. When He^+ ion penetrate through the GeO_2 layer (we used the density of GeO_2 , exact composition of GeO_x is not known) they lose some energy which is denoted by $\frac{dE}{dx}$. The value of $\frac{dE}{dx} = 284$ eV/nm, for 3 MeV Helium ions in GeO_2 with density of 4.25 gm/cm³ ($\frac{dE}{dx}$ value for SiO_2 is also approximately equal to GeO_2 value) which is calculated by using SRIM software [133]. The shift in the Ge peak position for the case of the sample annealed at 750 °C, 800 °C is ± 2 keV which corresponds to ≈ 4 nm thickness change in GeO_2 layer with respect to as-deposited case. The shift in the silver peak can be converted into distance by using $\frac{dE}{dx}$ value and the values are as follows for 700 °C, 750 °C and 800 °C are ≈ 96 nm, ≈ 69 nm and ≈ 110 nm respectively revealing the highest inter diffusion is for 800 °C which is also confirmed from X-TEM results.

Figure 6.5 (c) is the comparative HRXRD spectrum of Ag (002) reflection of 2 nm Ag/17 nm $GeO_x/SiO_x/Si(100)$ annealed at 700 °C, 750 °C and 800 °C in air. From the chapter-5, it can be noted that the intensity of Ag(002) peak is stabilized (fig

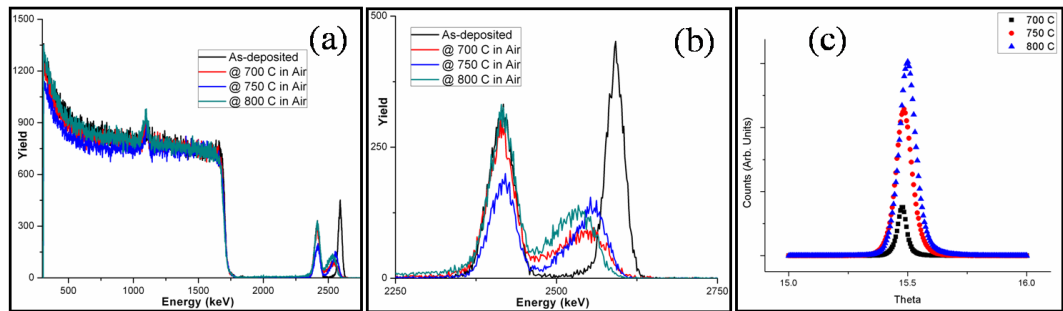


Figure 6.5: (a) Comparative RBS spectrum (b) Ge and Ag edges and (c) comparative HRXRD Ag (002) reflection of 2 nm Ag/17 nm $\text{GeO}_x/\text{SiO}_x/\text{Si}(100)$ annealed at 700 °C, 750 °C and 800 °C in air .

5.4 (b)) after 1500 second which is 25 minutes. Assuming that complete formation of the endotaxial structures is happened within this time, we have calculated the intensity ratio of Ag(002) peak is calculated to find the % of endotaxial nanostructures formation at 700 °C, 750 °C with respect to 800 °C annealing temperature. 14% of the endotaxial nanostructures formation was yielded for 700 °C annealed sample and 50% the silver nanostructures are endotaxial or aligned along (002) direction for 750 °C annealing temperature compared to 800 °C annealing temperature. These results were checked with the intensity ratio of the Ag(002) peak of 4 nm Ag/17 nm $\text{GeO}_x/\text{SiO}_x/\text{Si}(100)$ annealed at 800 °C *in-situ* case, at 700 °C temperature the ratio is same *i.e.* 14% but at 750 °C the ratio is not same and the value is lesser than the *ex-situ* value *i.e.* 32%.

6.3.2 Thickness Dependent Study

Silver Case

In the thickness dependent study, how the initial thickness of the GeO_x layer plays a role in the formation, size of the endotaxial nanostructures and their height above the interface and depth into the substrate will be discussed. Initial thicknesses of 2 nm Ag /5 nm $\text{GeO}_x/\text{SiO}_x/\text{Si}(100)$, 2nm Ag /17 nm $\text{GeO}_x/\text{SiO}_x/\text{Si}(100)$ and 2 nm Ag /60 nm $\text{GeO}_x/\text{SiO}_x/\text{Si}(100)$ are considered for this study and all the samples were annealed under same conditions up to 800 °C in air for 30 minutes. The results of 5

nm GeO_x , 60 nm GeO_x samples were compared with 17 nm GeO_x sample to understand the results. Figure 6.6 is the SEM micrograph of all the above three samples annealed in air up to 800 °C for 30 minutes. Figure 6.6 (a) is the SEM micrograph of 2 nm Ag /5 nm GeO_x /SiO_x/Si(100) annealed in air up to 800 °C for 30 minutes revealing the formation of silver nanostructures. Figure 6.7 (a) is the corresponding low magnification X-TEM micrograph of the sample showing the embedding of silver into the substrate and a thickness of 20 nm was measured for GeO_x layer and 43 nm thickness was measured for SiO_x layer. The depth of penetration of these nanostructures with in the Si substrate is ≈ 15 nm from the interface. Figure 6.7 (b) is the HR-X-TEM micrograph taken on one the inverted triangular island. A lattice spacing of 0.236 nm was measured on the triangular structure and 0.316 nm was measured on the substrate and these lattice spacings are correspond to Ag(111) and Si(111) planes respectively and these lattice planes are parallel to each other. A translational Moire fringes were observed on the structures and the periodicity of these fringes was measured as 0.961 nm which is well matched with the calculated translational Moire fringe formula $d_m = \frac{d_2}{1 - \frac{d_2}{d_1}}$ [111]. Where d_m is the translational Moire fringe spacing and d_1 , d_2 are the constituent lattice spacings. Figure 6.7 (c) is the SAED pattern taken on some of the nanostructures revealing the single crystalline nature of the nanostructures and all the spots of silver are exactly following the symmetry of substrate silicon indicating the formation of the endotaxial silver nanostructures.

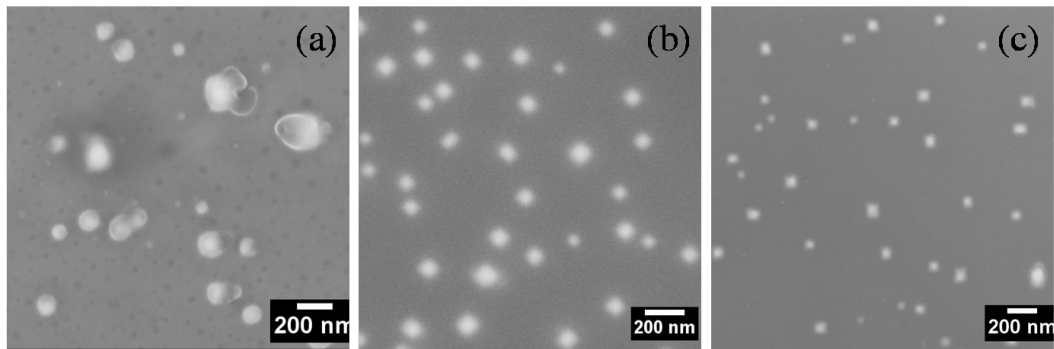


Figure 6.6: SEM Micrographs of 2 nm Ag on (a) 5 nm GeO_x (b) 17 nm GeO_x (c) 60 nm GeO_x on SiO_x/Si(100) annealed at 800 °C in air for 30 minutes.

Figure 6.4 (a) is the low magnification cross-sectional TEM micrograph of 2 nm Ag /17 nm GeO_x /SiO_x/Si(100) at 800 °C annealed in air revealing the embedding of

silver into silicon. From this figure, thickness of the top oxide layers were measured as 70 nm for GeO_x layer and 25 nm for SiO_x layer. The depth of penetration of these nanostructures within the Si substrate is ≈ 36 nm from the interface and the height of these nanostructures from the Si interface is ≈ 10 nm. The ratio between height and depth was calculated which yields 0.3. The height of the silver endotaxial nanostructures is arose here compared to 2 nm Ag /5 nm $\text{GeO}_x/\text{SiO}_x/\text{Si}(100)$ at 800°C case due to the high availability of Ge atoms and the depth of these nanostructures is increased by ~ 2 times. The SiO_x layer thickness for this case is ≈ 1.7 times lesser compared to 5 nm GeO_x initial thickness case.

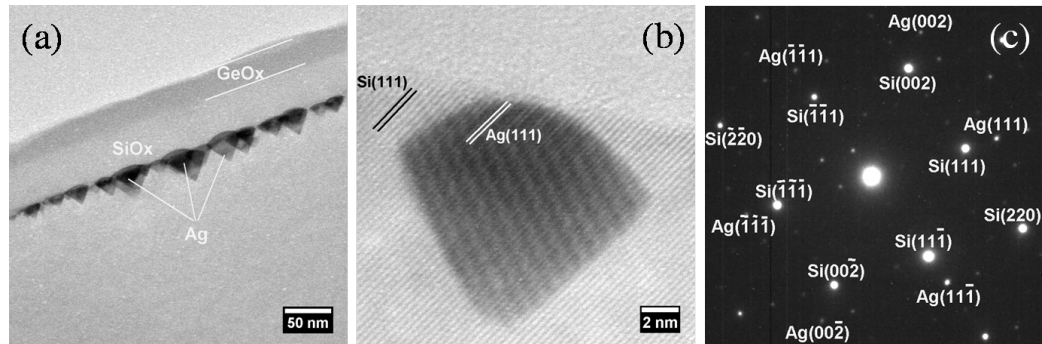


Figure 6.7: X-TEM Micrographs of 2 nm Ag /5 nm $\text{GeO}_x/\text{SiO}_x/\text{Si}(100)$ @ 800°C annealed in air (a) Low Mag (b) HR-X-TEM depicts endotaxial structures (with Moire fringes) and (c) Diffraction pattern from a single nanostructure.

Figure 6.8 (a) is the corresponding low magnification X-TEM micrograph of the sample showing the embedding of silver into the substrate. From this figure, a thickness of 70 nm was measured for GeO_x layer and 13 nm thickness was measured for SiO_x layer. The depth of penetration of these nanostructures within the Si substrate is ≈ 53 nm from the interface and the height of these nanostructures from the Si interface is ≈ 32 nm. The ratio between height and depth was calculated which yields 0.6 which is almost double than the 2nm Ag /17 nm $\text{GeO}_x/\text{SiO}_x/\text{Si}(100)$ @ 800°C case. It is to be noted that thickness of the SiO_x layer is also decreased and the decrement is by a factor of ≈ 3 . The reason for the decrement in the SiO_x layer thickness is due to the high availability of Ge atoms. The height and depth are also increased with increase in the initial GeO_x layer thickness. Figure 6.8 (b) is the SAED pattern taken on some of the nanostructures revealing the single crystalline nature of the nanostructures and

for lesser thickness requirement [154, 155]. Higher chemisorption of oxygen leads to decrement in the free Ge, Si atoms which are crucial for the enhanced desorption of native oxide layer at atmospheric conditions.

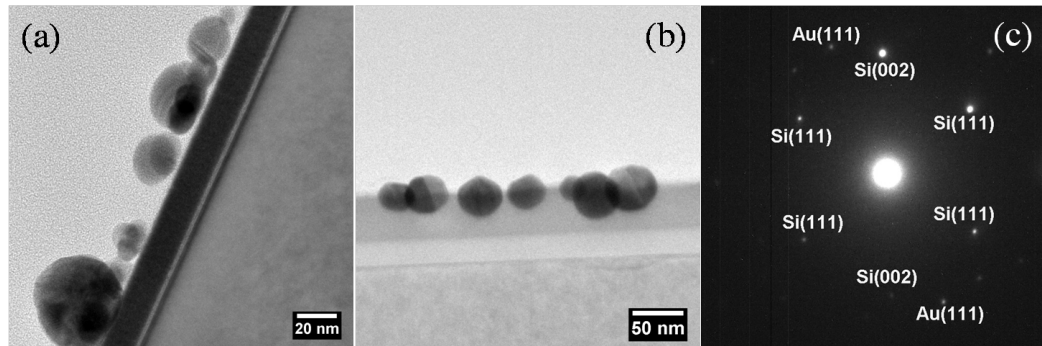


Figure 6.10: X-TEM Micrographs of 2 nm Au / 17 nm $\text{GeO}_x/\text{SiO}_x/\text{Si}(100)$ (a) as deposited (b) Low Mag of sample annealed at 800 °C in air for 30 minutes and (c) Diffraction pattern on nanostructures.

6.4 Chapter Summary

We reported the growth of silver endotaxial nanostructures and the optimal conditions for synthesizing these structures. Role of GeO_x thickness is discussed for both silver and gold cases. For 17 nm GeO_x case silver yields substrate symmetric endotaxial nanostructures at 800 °C where as for gold case the thickness of GeO_x is much lesser i.e. 5 nm GeO_x yields endotaxial nanostructures. For silver case, we have investigated 5nm GeO_x thickness and 60 nm GeO_x thickness, for all the cases substrate symmetric endotaxial nanostructures were formed. Up to now we have discussed about the silver endotaxial nanostructures growth by depositing silver on GeO_x coated silicon substrate by PVD method. In the next chapter, we will discuss the deposition of silver by chemical vapor deposition method by using a silver wire as source to deposit Ag on GeO_x coated silicon substrate.

Chapter 7

Substrate Symmetry Driven Endotaxial Silver Nanostructures by Chemical Vapor Deposition

7.1 Introduction

In the previous chapters, we have discussed the growth of endotaxial silver nanostructures on silicon substrate and the role of GeO_x layer in the formation of substrate symmetric structures is discussed. The effect of annealing ambience on the size and dielectric media around the nanostructures was discussed. Role of energetics in the formation of these nanostructures and effect of annealing temperature is also discussed. Effect of the initial GeO_x layer thickness on the size of these endotaxial nanostructures was discussed in the previous chapter along with the possibility of endotaxial gold nanostructures. Does the presence of metal on top of the GeO_x layer has any role in the formation of these nanostructures or can we supply the metal vapors separately to form these structures? Chemical vapor deposition (CVD) is one of the methods to answer the above questions where the metal vapors can be supplied to the substrate through a precursor. Besides supplying of metal vapor, CVD has many advantages like controlling the deposition time and deposition temperature to obtain the control over coverage and size of the structures during synthesis. This chapter deals with the growth of endotaxial silver nanostructures on Si and GeO_x/Si substrates by using CVD technique. The effect of deposition time on coverage and the effect of growth temperature on the size of these nanostructures were discussed.

On earlier occasions, a solution phase polyol synthesis had been used to grow various shapes, such as, pentagonal nanowires, cuboctahedra, nanocubes, nanobars, etc [110]. In this chapter, we discuss on the thermal etching of native oxide using GeO_x layer as an etchant to remove the native oxide at 800 °C in atmospheric conditions. Following this step, various shapes of Ag nanostructure were obtained on silicon substrates for orientations (100), (110) and (111) where Ag vapors are supplied through CVD method. Planar transmission electron bright field micrograph depicts the various shapes as square, rectangular/rod and triangular Ag nanostructures for the substrate orientations of (100), (110) and (111) respectively. It should be noted that the TEM micrographs are the projection images and the actual shapes of these structures inside the silicon structures would be governed by the interfacial energetics. It is established that the surface of the single crystalline silicon get oxidized by saturating its dangling bonds with oxygen and this results in the formation of a nanometer thick native oxide (SiO_x). There are several methods to etch the native oxide, such as, chemical etching with hydro fluoric (HF) acid [68], thermal etching at high temperatures that is commonly used in study of surface structures on silicon [156], and by ion beam sputtering process [156], etc. Russel et. al., reported the vacuum thermal etching of silicon and germanium surfaces in the temperature regime of 900°C-1300°C. [70]. Hopper et. al., reported the removal of oxide layer by flashing at 1200 °C and ion bombardment to get an optically flat silicon substrate under ultra high vacuum conditions [156]. Futagami et. al., reported the thermal etching of Si(100) at 1200 °C in argon atmosphere [71]. Here, we report on low temperature etching of silicon substrate using GeO_x as an intermediate layer and thus helping in the growth of endotaxial silver nanostructures. To best of our knowledge, no reports of thermal etching of silicon oxide under atmospheric CVD conditions have been reported yet. Chemical vapor deposition is one of the well known experimental methods to grow materials and is sensitive to temperature, rate of gas flow, distance between precursor and source [77]. In the present work, a simple low cost CVD system was used to carry out the growth of Ag nanostructures.

7.2 Experimental Methods

Silicon wafers were cleaned by standard procedure of rinsing with alcohol and de-ionized water. Deposition of germanium was done by physical vapor deposition (PVD) system. Under the growth condition (PVD), it was found that a GeO_x has been formed. Confirmation of the presence of GeO_x has been done with the help x-ray photoelectron spectroscopy (XPS) measurements (data not shown here). For all these systems, at first, a 17 nm GeO_x was deposited on Si(100), Si(110) and Si(111). The synthesis of Ag nano structures were done by an indigenous CVD system with a side entry furnace and a quartz boat of 80 cm length and 5 cm diameter, the source used was silver wire. Silver has been deposited in the CVD chamber on two different substrates i.e. on (i) 17 nm GeO_x /2 nm SiO_x / Si with (100), (110) and (111) orientations and (ii) silicon with (100), (110) orientations (without GeO_x interfacial layer). Distance between the source and sample was kept constant (2 mm) and heated upto 800 °C, kept for 30 minutes at 800 °C for deposition on the samples. CVD deposition time and temperatures were varied to understand the dependency of coverage and shape on these parameters. Deposition times for the growth are 30 minutes and 60 minutes and deposition temperatures are 800 °C, 850 °C and 900 °C.

The post growth characterizations were carried out ex-situ using field emission gun based scanning electron microscope (FEG-SEM, Neon-40 Carl Zeiss GmbH). Planar and Cross-sectional TEM samples were prepared by mechanical polishing followed by low energy Ar^+ ion milling to achieve the electron transparency. Transmission Electron Microscope (TEM) micrographs were carried out with 200keV JEOL JEM-2010.

7.3 Results and discussions

In our work, GeO_x intermediate layer is found to be important for the growth of symmetric endotaxial silver nanostructure. To elucidate the use of GeO_x layer, first we discuss the growth of silver nanostructures without the intermediate GeO_x layer. The silver wire has been kept in the heating zone of a tube furnace, on the side of a silicon substrate with different substrate surface orientations (the substrate is always covered with a 2 nm native oxide). Figure 7.1 (a) and (b) are the scanning electron microscope (SEM) micrographs of silver nanostructures that are deposited

using Ag-wire as a source for Si(100), and Si(110) at 800 °C in air for 30 minutes, respectively. These images reveal that no regular shapes are formed. It is to be noted that, only a native oxide (SiO_x) of 2.0 nm thick is present at on the silicon substrate. No substrate symmetry driven Ag nanostructures were formed for this case (i.e, when there no GeO_x layer on the silicon substrate).

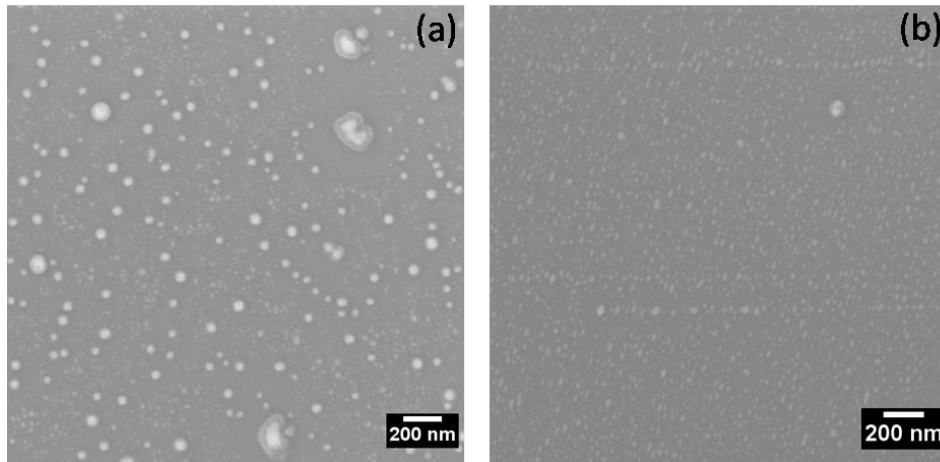


Figure 7.1: SEM Micrographs of Silver nanostructures deposited using Ag-wire as a source on (a) SiO_x/Si (100) (b) SiO_x/Si (110) at 800° C in air for 30 minutes.

Corresponding to the Ag structures grown on Si(100), Figure 7.2(a) depicts a low magnification cross-sectional transmission electron microscope (X-TEM) micrograph of silver nanostructures and Figure 7.2(b) is depicts a high resolution (HR) X-TEM micrograph, confirming the growth of endotaxial structures grown in Si(100). From the HR-X-TEM image inter-planar distance of 0.238 ± 0.005 nm corresponding to Ag(111) and an inter-planar spacing of 0.315 ± 0.005 nm corresponding to Si(111) were found. Though the substrate is (100) oriented, a cross-section view allow to image (111) planes in the system, as shown in Figure 7.2. Selected area electron diffraction (SAED) pattern taken from a single Ag nanostructure is shown in Figure 7.2(c), and this confirms the presence of single crystalline nature of Ag nanostructures.

Figure 7.3 (a) is a planar TEM micrograph depicting the as deposited 17 nm GeO_x/Si (100) substrate. Figure 7.3 (b) is the HRTEM micrograph of the small area marked on figure 7.3 (a) which is revealing the small crystalline region with a lattice spacing of

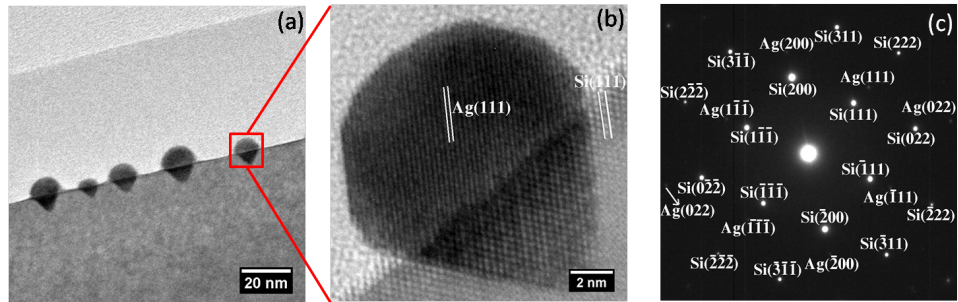


Figure 7.2: X-TEM Micrographs of Silver nanostructures deposited using Ag-wire as a source on $\text{SiO}_x/\text{Si}(100)$ at 800°C in air for 30 minutes (a) Low mag X-TEM (b) HR-X-TEM (c) SAED showing pure single crystalline silver.

0.249 nm which corresponds to (110) plane of hexagonal phase GeO_2 . Figure 7.3 (c) is the SAED pattern taken on the as deposited 17 nm $\text{GeO}_x/\text{Si}(100)$ substrate revealing that the overall GeO_x deposition is amorphous in nature and the radii of diffused rings are 0.189 nm and 0.34 nm belongs to (003), (101) planes of hexagonal phase GeO_2 .

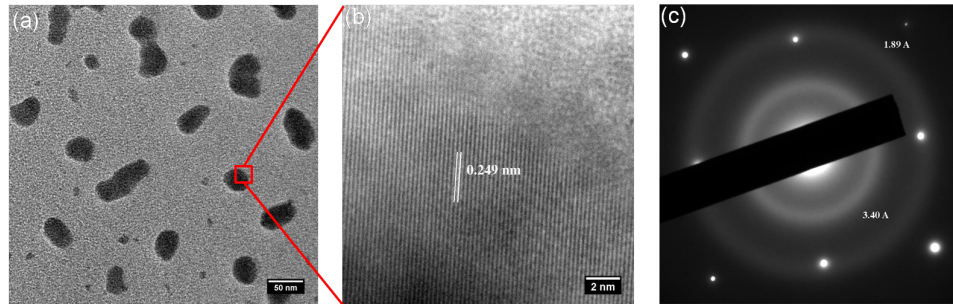


Figure 7.3: TEM Micrographs of as deposited GeO_x on $\text{Si}(100)$ using PVD method (a) Low mag (b) HRTEM (c) SAED showing amorphous GeO_x layer.

Now, we show formation of well-defined shapes of Ag structures on Silicon substrate by introducing a 17 nm thick GeO_x on the native oxide covered silicon substrates with various orientations. Figure 7.4 depicts the SEM images of Ag nanostructures grown by CVD method on GeO_x/Si substrates at 800°C . As shown in Figure 7.4(a), 7.4(b) and 7.4(c), the SEM micrographs depicts square/rectangular, rod and triangular structures grown on $\text{Si}(100)$, $\text{Si}(110)$ and $\text{Si}(111)$ substrates, respectively. It is

to be noted that the shapes of surface-unit-cell of Si(100), Si(110) and Si(111) are square, rectangular and triangular shapes corresponding to four, two and three fold symmetry. SEM micrograph shown in Figure 7.4(a) depicts the nano square shaped structures on Si(100) with a coverage area of 2.3% with an average length $90 \text{ nm} \pm 9 \text{ nm}$, breadth of $85 \text{ nm} \pm 9 \text{ nm}$ and with an aspect ratio of ≈ 1.0 . The SEM micrograph shown in Figure 7.4(b) depicts the presence of ordered nanorods on Si(110) substrate, following its 2-fold symmetry of the surface unit cell of the substrate with the dimensions of the structures are $650 \text{ nm} \pm 63 \text{ nm}$ length, $45 \text{ nm} \pm 6 \text{ nm}$ diameter with an aspect ratio of ≈ 14.3 . Similarly, the SEM micrograph shown in Figure 7.4 (c) reveals the formation of triangular nanostructures formed by following the 3-fold symmetry of Si(111) substrate with a coverage area of $\approx 0.5\%$. The error bars are the standard deviations obtained from averaging many frames, involving many particles. Though the shapes follow the corresponding unit-cell symmetry, the size is distribution is not mono-disperse.

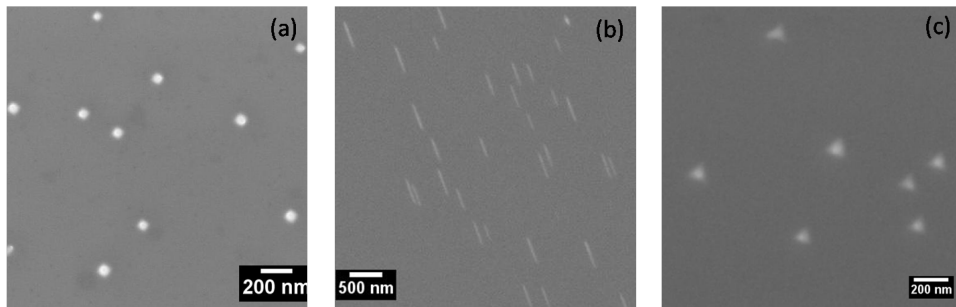


Figure 7.4: SEM Micrographs of Silver nanostructures deposited using Ag wire as a source on 17 nm GeO_x deposited (a) Si(100), (b) Si(110), (c) Si(111) substrates at 800° C in air for 30 minutes. .

We now discuss more on the nature of the silver nanostructures that are grown on Si(100) using aforementioned method (with GeO_x interfacial layer). Figure 7.5 (a) and (b) show planar and X-TEM images (low magnification bright field conditions) of silver nano structures grown using a 17 nm $\text{GeO}_x/\text{Si}(100)$ by using silver wire as a source material in the atmospheric CVD process; Many frames like the one shown in Figure 7.5(a) have been taken to determine the error bars in the sizes. The figure 7.5(c) shows a high-resolution (HR) X-TEM micrograph of the nano square structures. From the HR-X-TEM micrograph, inter planar distance of 0.238 nm corresponding to

Ag(111) planes can be seen along with a spacing of 0.315 ± 0.005 nm corresponding to substrate silicon (111) reflection. It is to be noted that the substrate surface is (100) direction but when the XTEM measurements are carried out from this specimen, Si(111) structures can be observed. The lattice image depicts the presence of Moire fringes in the structures, which confirms the presence of endotaxial nature of silver nanostructures in silicon. The coherent inclusion of Ag nanostructures inside the silicon has been confirmed by analyzing the Moire fringes. We deduce this relationship between the substrate lattice planes of both Ag and Si, by further using the observed Moire fringes that are observed in Figure 7.5(c). The Moire fringe spacing (d_m) is determined by the formula

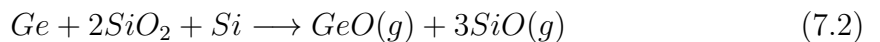
$$d_m = \frac{d_1 d_2}{\sqrt{(d_1 - d_2)^2 + d_1 d_2 \beta^2}}$$

where d_1, d_2 are lattice spacing of the planes which are constituents of Moire fringes and β is the angle between the planes [111]. The Moire fringe spacing of 0.96 nm was calculated between Ag (111) and Si (111) planes with $\beta=0$. This matches well with the measured fringe spacing 0.95 ± 0.01 nm confirming the coherence (endotaxy) of silver nanostructures. Figure 4(d) is the selected area electron diffraction (SAED) pattern taken on a single structure and indexed by following the symmetries of the diffraction spots. The SAED pattern confirms the single crystalline nature of the nanostructures as pure silver. For all three substrate orientations of silicon i.e. for Si(100), Si(110) and Si(111), with GeO_x on Si, substrate symmetric endotaxial Ag nanostructures have been obtained.

A plausible mechanism for the formation of such endotaxial nano structures discussed below. In obtaining the endotaxial structures, a 17 nm $\text{GeO}_x/2$ nm $\text{SiO}_x/$ Si sample was annealed along with Ag wire separated by a distance of 2 mm in the furnace up to 800 °C in air. On annealing of Ge oxides, it is known that the GeO_2 transform to GeO and desorbs for temperatures ≥ 420 °C [157]. Wang et al. [116], reported the disproportionation of GeO into GeO_2 and Ge as per the following equation



Ge thus formed in the disproportionation of GeO would react with native SiO_x to form volatile SiO around 750°C, as shown by Yun et al. [117],



It is interesting to note that reaction between GeO_x and SiO_x is expected to be cyclic in nature and as this helps in creating clean surface for the deposition of Ag vapors. During the above process, silver vapors adsorbed on the silicon surface and the substrate allows it to grow the substrate symmetric silver nanostructures [77]. Silver diffusion through the interstitial - substitution mechanism [118, 119]. This inter-diffusion might be one of the reasons to form endotaxial nanostructures.

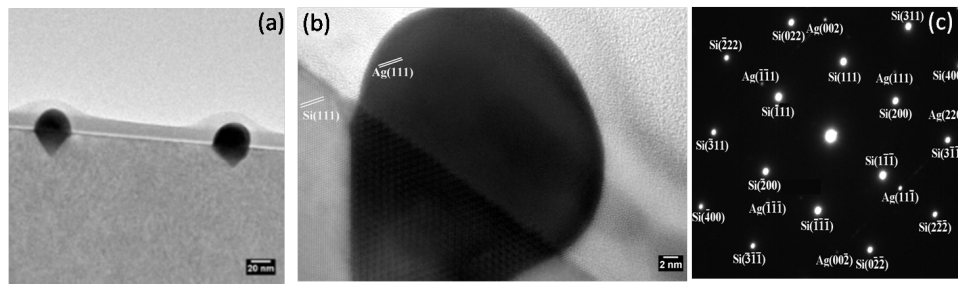


Figure 7.5: TEM Micrographs of Ag nanostructure on $\text{Ge}/\text{SiO}_2/\text{Si}(100)$ at $800\text{ }^\circ\text{C}$ for 30 minutes (a) Planar TEM image (b) Low magnification X-TEM image (c) HR-X-TEM image and (d) SAED on single structure.

We also found that the time duration during the CVD process can be used as a parameter to increase the coverage area. Figure 7.6(a) depicts an SEM micrograph of silver nano structures deposited on $17\text{ nm GeO}_x/2\text{ nm SiO}_x/\text{Si}(110)$ using Ag wire as a source for 60 minutes. Coverage of silver nanorods is increased from 2.3% to 9.6%. Similarly, an increase in the coverage from 0.5% to 7.0% is observed for $17\text{ nm GeO}_x/2\text{ nm SiO}_x/\text{Si}(111)$ with 60 minutes deposition time. Figure 7.6(b) depicts an SEM micrograph. Controlled growth of substrate symmetric silver nano structures with desired coverage and size can be obtained by varying the parameters of CVD [77].

We also found that the temperature during the CVD process can be used as a parameter to increase the size of the nanostructures and as well as to alter the oxide layers thickness around these nanostructures. Figure 7.7 depicts an SEM micrograph of silver nanostructures deposited on $17\text{ nm GeO}_x/2\text{ nm SiO}_x/\text{Si}(100)$ using Ag wire as a source for 30 minutes at different deposition temperatures ranging from $800\text{ }^\circ\text{C}$ to $900\text{ }^\circ\text{C}$. Figure 7.7 (a), (b) and (c) depicts an SEM micrograph of silver nano structures deposited on $17\text{ nm GeO}_x/2\text{ nm SiO}_x/\text{Si}(100)$ using Ag wire as a source

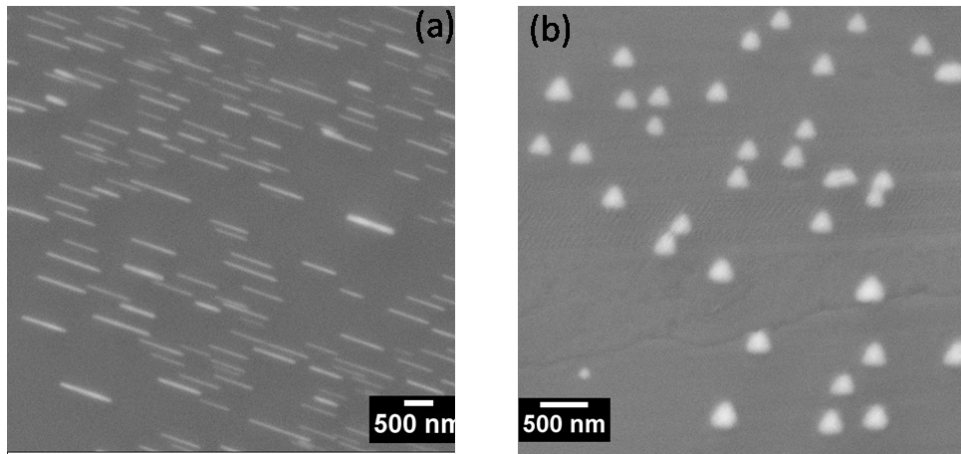


Figure 7.6: SEM Micrographs of Silver nanostructures deposited using Ag wire as a source on 17 nm GeO_x deposited (a) Si(110) (b) Si(111) substrates at 800 °C in air for 60 minutes.

for 30 minutes at temperature of 800 °C, 850 °C and 900 °C respectively.

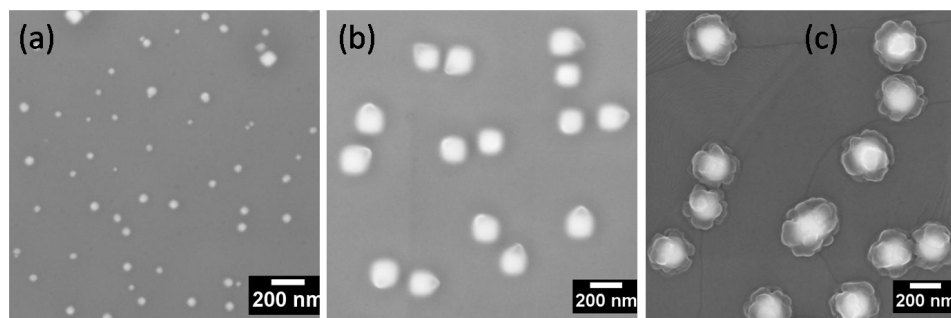


Figure 7.7: SEM Micrographs of Silver nanostructures deposited using Ag wire as a source on 17 nm GeO_x deposited Si(100) at (a) 800 °C (b) 850 °C and (c) 900 °C in air for 30 minutes.

Figure 7.8(a), (b) and (c) are the X-TEM micrograph of the nanostructures deposited on 17 nm $\text{GeO}_x/2$ nm $\text{SiO}_x/\text{Si}(100)$ using Ag wire as a source for 30 minutes at temperatures of 800 °C, 850 °C and 900 °C respectively revealing the incremental diffusion of silver into silicon substrate with increasing temperature. The height and depth of these nanostructures at each temperature are 23.5 nm, 23 nm with a height to depth ratio of ≈ 1 for 800 °C, 38.9 nm, 58.1 nm with a height to depth ratio of ≈ 1.3 for 850

Table 7.1: Details related to depth, height, oxide thickness, ratio for endotaxial Silver nanostructures for different deposition temperatures.

	800 °C	850 °C	900 °C
Height	23.1 nm	50.1 nm	147.4 nm
Depth	23.5nm	38.9 nm	97.8nm
GeO _x thickness	12.6 nm	27.6 nm	32 nm
SiO _x thickness	2 nm	42.7 nm	57.1nm
$\frac{Height}{Depth}$	1	1.3	1.6

°C and 97.8 nm, 147.4 nm with a height to depth ratio of 1.6 for 900 °C respectively. It is clear from the above data that with increment in the deposition temperature height of these silver endotaxial nanostructures is increasing. Complete details of height, depth and their ratio along with top oxide layer thicknesses were shown in the table-7.1.

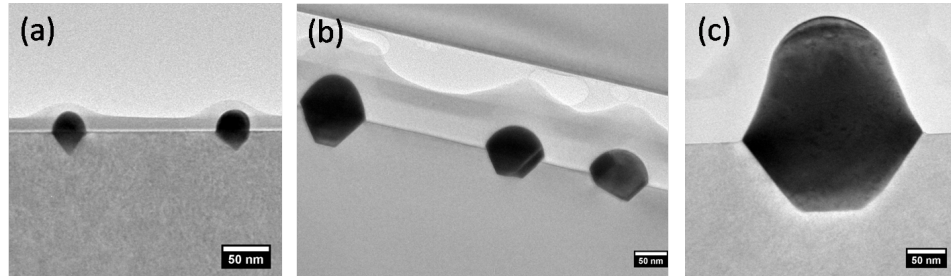


Figure 7.8: X-TEM Micrographs of Silver nanostructures deposited using Ag wire as a source on 17 nm GeO_x deposited Si(100) at (a) 800 °C (b) 850 °C and (c) 900 ° C in air for 30 minutes.

Figure 7.9 (a) is comparative XRD spectra of Ag(002) peak of Ag wire as a source on 17 nm GeO_x deposited Si(100) at 800° C, 850 °C and 900 ° C in air for 30 minutes. From the figure, it can be observed that the Ag(002) peak has asymmetric broadening for 850 °C and 900 ° C deposition temperatures. This asymmetric broadening might be due to the merge of two different peaks. The peaks were deconvoluted to find the peak positions and shown in figure 7.9 (b), (c) for 850 °C and 900 ° C deposition temperatures, respectively. For the case of 850 °C deposition temperature, the peak positions are at 15.423° and 15.473° respectively. The corresponding lattice

constants were calculated using Bragg's law yielded 2.047 \AA and 2.041 \AA respectively. The bulk Ag(002) interplanar spacing is 2.043 \AA . We have observed the change of lattice spacing from the bulk value is observed and the increment is $+0.004 \text{ \AA}$ and -0.002 \AA respectively. The intensity ratio of these two peaks is 0.21. For the case of $900 \text{ }^\circ\text{C}$ deposition temperature, the peak positions are at 15.423° and 15.483° respectively and the corresponding lattice constants are 2.047 \AA and 2.04 \AA respectively with the intensity ratio of 0.64. This is revealing that the more amount of silver is going towards the higher lattice constant side or experiencing a tensile stress. From figure 7.8, it can be noted that more amount of silver is intruded into the silicon and the inter diffusion of silver is through substitutional mechanism. So more and more silver is substituting the Si atoms there will be a tensile stress acts on the Ag atoms to form an epitaxial relationship with the substrate leads to increment in the inter-planar spacing of Ag(002) plane. Due to the different thermal expansion coefficients of Ag, Si there might be a lattice contraction in these cases. Above $700 \text{ }^\circ\text{C}$ temperature, the strain crosses the critical value to introduce dislocations and the Ag structures are relaxed. The relaxed Ag lattice is pinned at the interfacial plane with the Si lattice might be the reason for tensile strain [158]. For the case of 800°C deposition temperature, the amount of Ag material is lesser compared to higher deposition temperatures might be a reason where this type of asymmetry was not observed.

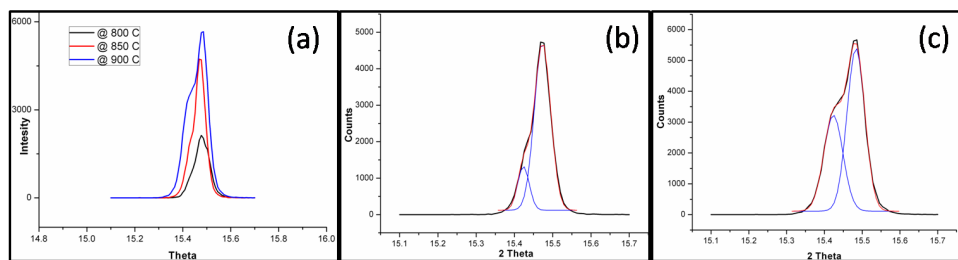


Figure 7.9: (a)Comparative XRD spectra of Ag(002) of CVD deposited Ag on $17 \text{ nm GeO}_x/\text{SiO}_x/\text{Si}(100)$ at deposition temperature of $800 \text{ }^\circ\text{C}$, $850 \text{ }^\circ\text{C}$ and $900 \text{ }^\circ\text{C}$ in air, deconvoluted plots of asymmetric Ag(002) peak for (b) $850 \text{ }^\circ\text{C}$ (c) $900 \text{ }^\circ\text{C}$ deposition temperatures.

7.4 Chapter Summary

Substrate symmetry driven silver nanostructures are grown on silicon substrates using CVD method with silver as a source and GeO_x layer as the interfacial layer. Endotaxial nanosquares/rectangles are formed in the case of Si (100), nanorods are formed on Si (110) and endotaxial nano triangles are formed for Si(111) substrate according to surface unit cell symmetries, respectively. Control over coverage can be obtained by varying the deposition time. Change of size is observed for different deposition temperatures. Height of these endotaxial structures, thickness of top oxide layers were increased with increasing deposition temperature. Application of these nanostructures as SERS substrates will be discussed in the next chapter.

Chapter 8

Applications of Endotaxial Silver Nanostructures as SERS Substrates

8.1 Introduction

In the previous chapters, a novel method of etching native oxide in presence of GeO_x layer has been made to grow Ag and Au endotaxial structures and their detailed characterization using various types of experimental methods. To best of our knowledge, the thesis work is probably the first such report on formation of endotaxial Ag and Au nanostructures. In this chapter, applications of these nanostructures as SERS substrates will be discussed.

The discovery of Surface Enhanced Raman Scattering (SERS) lead to the solutions for many challenges due to its power as an analytical tool for the sensitive and selective detection of molecules adsorbed on noble metal nanostructures [109,159–162]. In SERS, enormous field enhancement occurs at the noble metal junctions due to electromagnetic field localization coupling resonantly with the surface plasmon [163–166]. One of the major challenges in the field of SERS is to have an appropriate and effective substrate to take care of low signal enhancement, poor selectivity, unstable and irreproducible signals. Highly reproducible and stable substrates can efficiently be used as SERS based sensors for label free immunoassays [166], biosensing [167] and other applications [109]. The success and the usefulness of the SERS method depends on

the optimization of the interaction between adsorbed molecules and the surface plasmonic structures [109]. To maximize the enhancement factors for the SERS signal, various shapes and size combinations of gold and silver nanostructures, such as SiO₂-encapsulated gold particles [168], nanorods of Ag deposited using oblique angle vapor deposition [169], 2D Au nano-mushroom arrays [170], polyhedral Ag mesocages [171], and film over nanospheres (FONs) [172] have been tried out and obtained better stability and reproducibility in some cases.

8.2 Experimental details

Synthesis of the samples was done using both PVD and CVD methods and obtained different shapes depend upon the substrate orientations. Details of endotaxial Ag nanostructures growth and their characterization is discussed in previous chapters 3-7. These samples were cleaned using Piranha solution (1:1 H₂SO₄:H₂O₂ solution) for 30 minutes to remove the organic contaminates on the surface of the substrates and then dipped in 5% Hydrofluoric acid (HF) for 90 minutes to remove the top oxide layers such as, GeO_x and SiO_x. After removing from the HF solution, samples were allowed to dry in air for 30 minutes and then crystal violet (CV) solution with various concentrations was drop casted on top of the substrate. For the comparison purpose, CV solution was drop casted on plain silicon as well as on as deposited 2 nm Ag/17 nm GeO_x/SiO_x/Si(100) substrate. SERS spectra were recorded using micro-Raman spectrometer (LABRAM-HR) using laser excitation line of 514.5 nm at room temperature. Majority of SERS measurements were done at School of Physics, University of Hyderabad, Hyderabad using micro Raman spectrometer. For few samples, SERS measurements were done at Institute of Minerals and Materials Technology, Bhubaneswar. The reason for recording SERS spectra with this excitation wave length was to study resonance of adsorbate on Ag nanostructures. All the measurements were made in a backscattering geometry, using a 50× microscope objective lens with a numerical aperture of 0.7. Typical laser power at the sample surface was 1.0 mW with a spot size of 2 μm. A 20 μl of the CV solution (5×10⁻¹⁰ M) was dropped onto the SERS substrate and allowed it to dry naturally. A fixed volume micro-pipette with disposable tips was used to prevent contamination. In our tests, the dropped solution soon spread over the whole SERS substrate but confined

to the substrate.

8.3 Results and discussion

8.3.1 PVD based Ag endotaxial structures

For the samples that were deposited using PVD method, initially, we discuss the SERS results of crystal violet (CV) molecules of 5×10^{-10} M dropcasted on square/rectangular silver nanostructures grown on 2nm Ag/17 nm GeO_x/ SiO_x/ Si(100) at 800° C in air. CV is a commonly used molecule for SERS study because of its high Raman scattering cross-section and it chemisorb on the silver surfaces due to the amino group [173,174]. The SERS spectra reveal the characteristic peaks of CV at 1172 cm⁻¹, 1371 cm⁻¹, and 1619 cm⁻¹ [175]. Figure 8.1 (a) depicts the SEM micrograph of 2 nm Ag/17 nm GeO_x/ SiO_x/ Si(100) at 800° C annealed in air, and figure 8.1 (b) is the SEM micrograph of 2 nm Ag/17 nm GeO_x/ SiO_x/ Si(100) at 800° C annealed in air after treated with HF for 90 minutes to remove the top oxide layers and expose the Ag nanoparticles in order to use it for SERS. Figure 8.1 (c) is the corresponding SERS spectra of CV with 5×10^{-10} M concentration drop casted on this HF treated 2 nm Ag/17 nm GeO_x/ SiO_x/ Si(100) at 800° C, the same concentration of CV was drop casted on plain silicon so as to enable comparison with the endotaxial square nanostructures. Analytical enhancement factors (AEF) were calculated for the characteristic peaks of crystal violet using the following equation

$$A.E.F = \frac{\left(\frac{I_{SERS}}{C_{SERS}}\right)}{\left(\frac{I_{RS}}{C_{RS}}\right)}$$

The analytical enhancement factors for the CV at peak positions of 913 cm⁻¹, 1172 cm⁻¹ and 1371 cm⁻¹ are 1.7×10^7 , 1.8×10^7 and 1.8×10^7 respectively, for nanosquare/rectangular structured sample i.e. for 2 nm Ag/ 17 nm GeO_x/ SiO_x/ Si(100) at 800 °C annealed in air. For as-deposited case the A.E.F.s are as follows: 2.9×10^4 , 3.0×10^4 and 2.9×10^4 respectively. Figure 8.1(d) SERS spectrum of Crystal Violet on HF treated 2nm Ag/ 17nm GeO_x/ SiO_x/ Si(100) at 800 °C at different points depicting the consistency of the substrate with uniform enhancement. A SERS substrate can be readily obtained as and when required by etching out the oxide layer with HF. The silicon substrate with endotaxial Ag nanstructures are very stable and robust as these

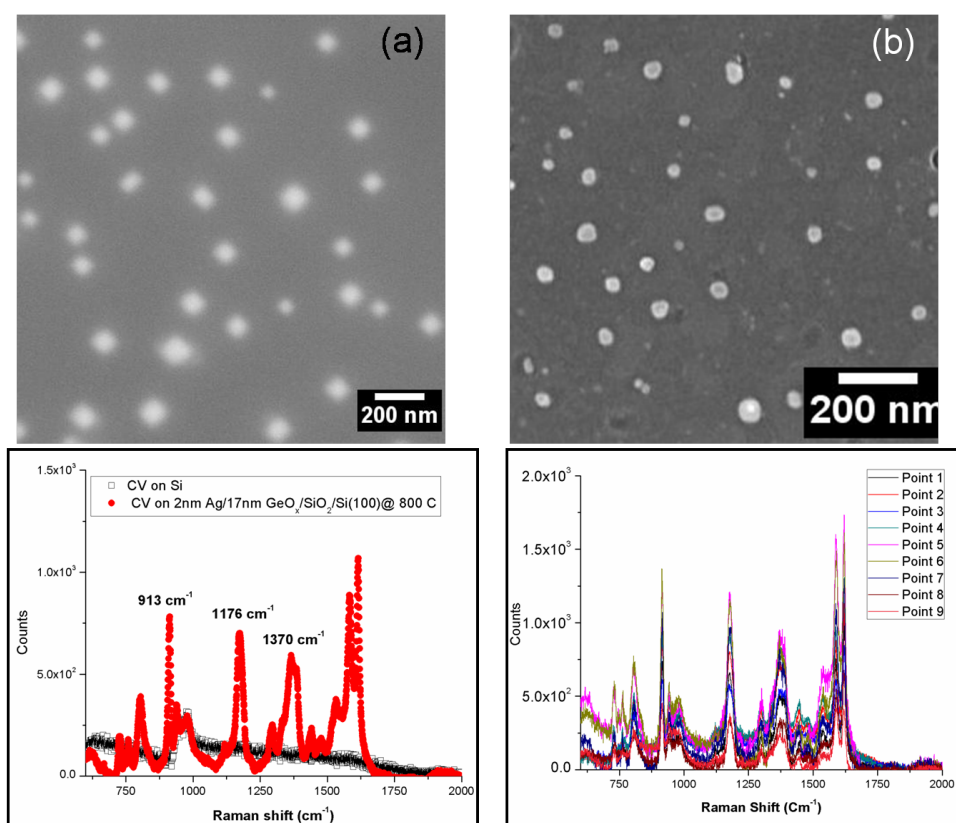


Figure 8.1: (a) SEM Micrographs of 2 nm Ag/17 nm GeO_x/ SiO_x/ Si(100) at 800 °C in air (b) after etched with Hydro fluoric acid for 90 minutes (c) SERS spectrum of Crystal Violet (CV) with a concentration of 5×10^{-10} M drop casted on 2 nm Ag/17 nm GeO_x/ SiO_x/ Si(100) at 800 °C in air etched with HF for 90 min and (d) SERS spectrum of Crystal Violet (CV) of above the sample at different points denoted by different colors showing the consistency of the substrate with uniform enhancement.

structures are embedded in silicon substrate and covered with SiO_x and GeO_x layers. The other major advantage is that, this technique provides the nanostructures that have sharp ordered edges that be obtained for high filed enhancements. The third advantage is that these structures are easy for manufacturing and would be cheaper.

Figure 8.2 (a), (b) are the SEM micrographs of the 2 nm Ag/ 17 nm GeO_x / SiO_x / Si(100) at 800 °C in low vacuum and UHV ambiances after etching with HF solution revealing the silver nanostructures presence on the surface of the sample. Figure 8.2 (c) shows the comparative SERS spectra of the 2 nm Ag/ 17 nm GeO_x / SiO_x / Si(100) at 800 °C in low vacuum and UHV ambiances. The enhancement factors for the case of low vacuum annealed sample were calculated for the characteristic peaks of CV and the values are 2.9×10^5 , 9.7×10^5 , 5.3×10^5 for 1176 cm^{-1} , 1378 cm^{-1} , 1620 cm^{-1} respectively [135, 176]. But the 915 cm^{-1} peak is mixed with the secondary silicon peak which is also a characteristic peak of crystal vioelet. These enhancement factors are lesser for low vacuum annealed case compared to SERS results with 2 nm Ag/ 17 nm GeO_x / SiO_x / Si(100) at 800 °C annealed in air annealing case (fig 8.1). This is possible as the coverage of the square shaped silver endotaxial nanostructures is less and the size of the nanostructures is more compared to the air annealed case. We have calculated effective enhancement factor and a detailed enhancement factors each for electromagnetic coupling and chemical effects are not discussed. The main focus of the thesis is on the growth aspects. The surface plasmons are dependent on shape, size, coverage and dielectric media around the nanoparticles [42]. In the UHV annealed sample case, we observed the signature of the CV molecules but the enhancements are not in the detectable order.

8.3.2 CVD based Ag endotaxial structures

In the CVD case, the study can be divided into two parts: (a) shape dependence study, (b) deposition time dependence

(a) Shape Dependent Study:

In the shape dependent study, three shapes are mainly considered which are square/rectangles, rods and triangles. These shapes are synthesized using CVD method with silver wire

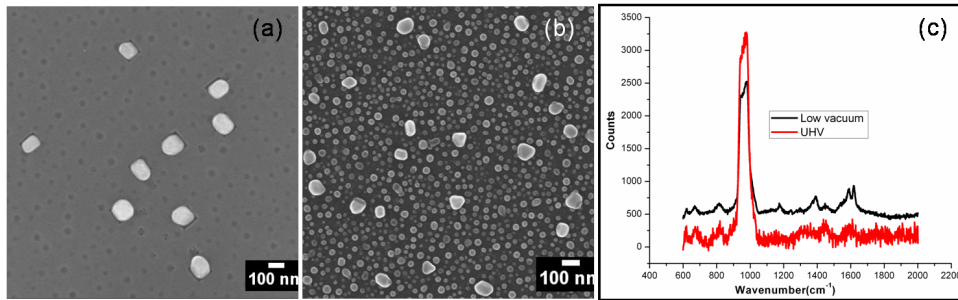


Figure 8.2: SEM micrographs of 2 nm Ag/ 17nm GeO_x/ SiO_x/ Si(100) at 800 °C in (a) low vacuum (b) UHV ambiances and (c) comparative SERS spectra of CV (5×10^{-10} M) on (a), (b)

as a source on GeO_x coated silicon substrates with (100), (110) and (111) orientations, respectively, at a deposition temperature of 800 °C for 30 minutes. Figure 7.1 is the SEM micrograph of the CVD prepared samples revealing the formation of nanosquares/rectangles, nanorods and nanotriangles on 17 nm GeO_x coated silicon substrate with (100), (110) and (111) orientations, respectively. The coverage of the nanostructures on these samples is 2.7%, 2.3% and 0.5% for nanosquares/rectangles, nanorods and nanotriangles, respectively. Figure 8.3 (a) shows the SERS spectra of CV molecules with 5×10^{-10} M concentration on the samples (as shown in fig 7.1). From the figure 8.3(a), one can conclude that the enhancement of the signals is very less for the nanotriangles and for nanorods, nanosquares/rectangles the enhancement factors are approximately equal. The numerical values of the enhancement factors were tabulated in the table 8.1. From the table 8.1, it can be observed that triangles have lowest enhancement factors due to the lowest coverage and rods have the highest enhancement factor and also high coverage squares have enhancement factors in between rods and triangles. In this case, the enhancement factors depends on two parameters: shape and coverage. In order to understand the effect of coverage, we have studied the particles of same shape with different coverages by changing the deposition time in the growth process.

(b) Coverage Dependent Study:

In the coverage dependent study we consider mainly two shapes i.e. rods and triangles of endotaxially grown Ag nanostructures. Figure 8.4 (a) is the SEM micrograph

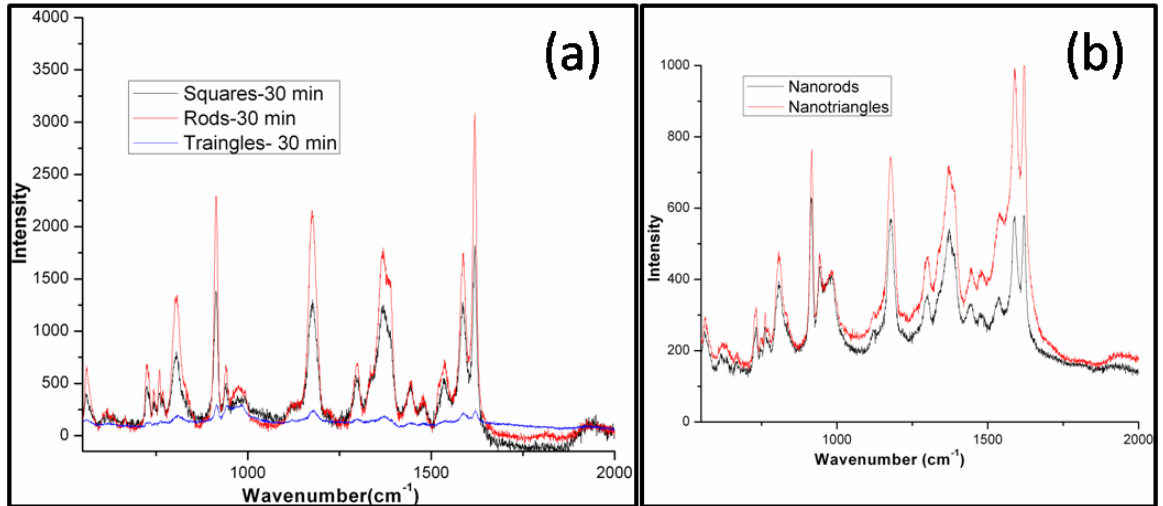


Figure 8.3: (a) comparative SERS spectrum of CV of 5×10^{-10} M on Ag/17 nm $\text{GeO}_x/\text{SiO}_x/\text{Si}(100)$, Ag/17 nm $\text{GeO}_x/\text{SiO}_x/\text{Si}(110)$, Ag/17 nm $\text{GeO}_x/\text{SiO}_x/\text{Si}(111)$ substrate at 800 °C in air for deposition time of 30 minutes (b) comparative SERS spectrum of CV of 0.5 nM on Ag/17 nm $\text{GeO}_x/\text{Si}(110)$, Ag/17 nm $\text{GeO}_x/\text{SiO}_x/\text{Si}(111)$ substrate at 800 °C in air for deposition time of 60 minutes.

Table 8.1: Enhancement factors of CV (0.5 nM) molecules for various CVD prepared samples.

Shape	AEF for 913	AEF for 1176	AEF for 1370
Squares-30 min	9×10^6	9.1×10^6	6.8×10^6
Rods-30 min	1.7×10^7	1.6×10^7	1.9×10^7
Rods-60 min	3.2×10^6	2.7×10^6	2×10^6
Triangles-30 min	1.1×10^6	7.6×10^5	2.6×10^5
Triangles-60 min	4×10^6	3.8×10^6	2.7×10^6

of Ag/17 nm $\text{GeO}_x/\text{SiO}_x/\text{Si}(110)$ substrate at 800 °C in air for 30 minutes deposition time revealing the substrate symmetric silver nanostructures formation with a coverage of 2.29%. When the deposition time is increased from 30 minutes to 60 minutes the coverage has changed to 9.62 % for Ag/17 nm $\text{GeO}_x/\text{SiO}_x/\text{Si}(110)$ substrate at 800 °C in air (figure 8.4 (b)). Figure 8.4 (c) is the SERS spectrum of 0.5 nM concentration CV molecules drop casted on both the samples revealing that the enhancement factor for 30 minutes growth is one order higher compared to 60 minutes growth.

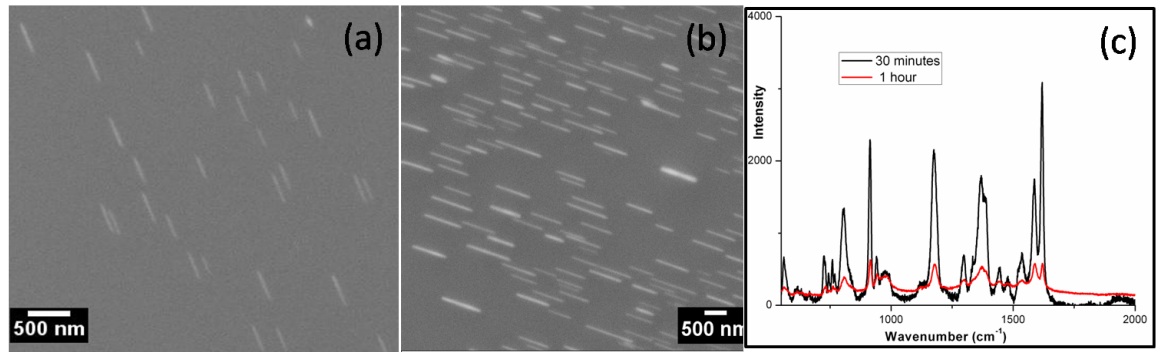


Figure 8.4: SEM Micrographs of Silver nanostructures deposited using Ag wire as a source on 17 nm $\text{GeO}_x/\text{SiO}_x/\text{Si}(110)$ substrate at 800 °C in air for (a) 30 minutes (b) 60 minutes and (c) SERS spectrum of 0.5 nM CV on (a) and (b)

Figure 8.5 (a) is the SEM micrograph of Ag/17 nm $\text{GeO}_x/\text{SiO}_x/\text{Si}(111)$ substrate at 800 °C in air for 30 minutes deposition time revealing the triangular shaped nanostructures formation which are following the three fold symmetry of the substrate and figure 8.5 (b) is the SEM micrograph of Ag/17 nm $\text{GeO}_x/\text{SiO}_x/\text{Si}(111)$ substrate at 800 °C in air for 60 minutes deposition time is revealing the increment in the coverage of triangular structures and the coverage was increased from 0.5 % to 7% for this case. Figure 8.5(c) is the SERS spectra recorded on both 30 minutes and 60 minutes deposition time case where 60 minutes deposition time case has better enhancement factor compared to 30 minutes growth revealing that increment in coverage can increase the enhancement. From these two cases, one can conclude that both shape and coverage can be used for enhancement but the optimal combination of these two can yield a better enhancement factors.

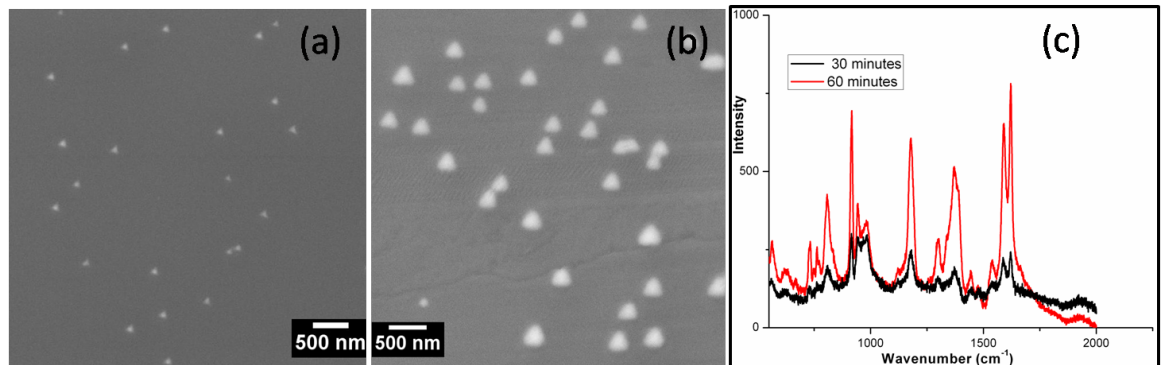


Figure 8.5: SEM Micrographs of Silver nanostructures deposited using Ag wire as a source on 17 nm $\text{GeO}_x/\text{SiO}_x/\text{Si}(111)$ substrate at 800 °C in air for (a) 30 minutes (b) 60 minutes and (c) SERS spectrum of 0.5 nM CV on (a) and (b)

In order to check the re-usability of these samples, we have considered the nanorod 30 minutes sample which has highest enhancement factor for CV molecule. This sample was cleaned with piranha solution by dipping it in the solution for 30 minutes to remove the CV molecules which were already drop casted on the substrate. After that the sample was etched with 5% HF solution for 1 minute to remove for any oxide layer present. R6G is a strong fluorescent Xanthene derivative which shows a molecular resonance Raman effect when excited into its visible absorption band [177] and it is biologically important [178–182]. The treated sample was used to drop cast the R6G dye molecule to check the re-usability of the sample. Figure 8.6(a) shows the SERS spectrum of the R6G molecules on nanorods 30 minute sample. Figure 8.6(b) revealing the consistency of the nanorods sample with almost uniform enhancement factors at different points of the sample. From this result we can conclude that these samples can be re-usable with proper cleaning.

In order to check the bio-compatibility of these samples, we have considered the nanosquares sample and whether these substrates can be used to detect biomolecules like creatinine. Creatinine is a product of muscle and is measured to check the health of kidneys. The sample was cleaned with piranha solution by dipping it in the solution for 30 minutes to removed the CV molecules which were already drop casted on the substrate. After that the sample was etched with 5% HF solution for 1 minute to remove if any oxide layer present. The treated sample was used to drop cast the creatinine molecules to check the re-usability of the sample. Figure 8.7(a) shows the

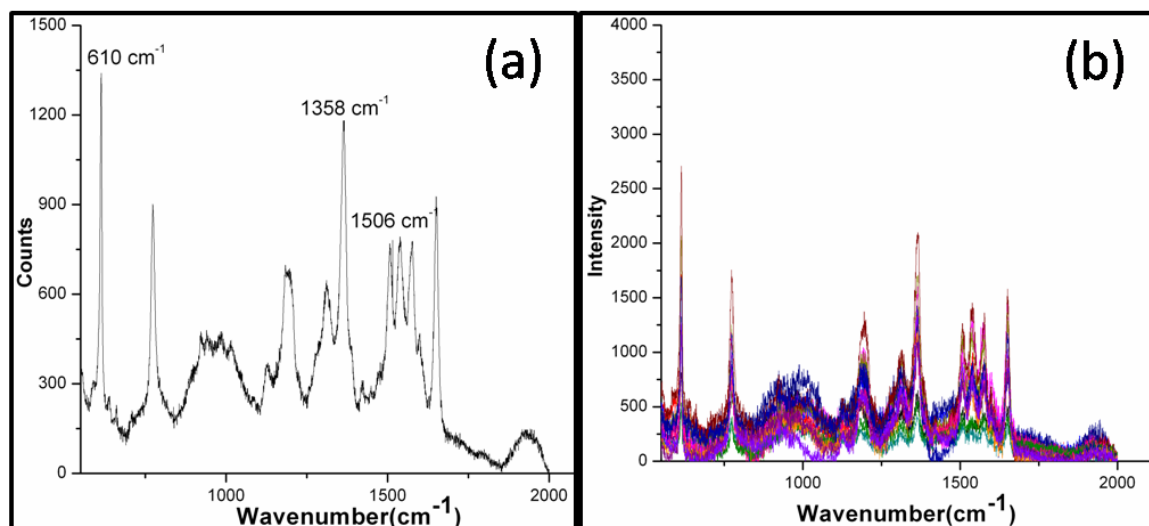


Figure 8.6: (a) SERS spectrum of 0.5 nM R6G on Silver nanostructures deposited using Ag wire as a source on 17 nm GeO_x/SiO_x/Si(110) substrate at 800 °C in air for 30 minutes (b) SERS spectra of R6G of above sample at different points denoted by different colors showing the consistency of the substrate with uniform enhancement.

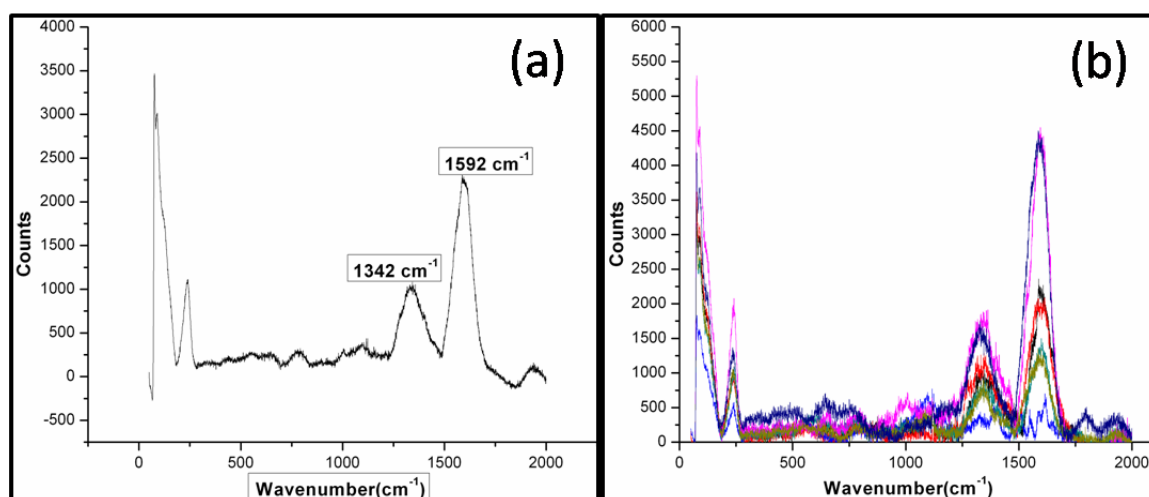


Figure 8.7: (a) SERS spectrum of Creatinine on Silver nanostructures deposited using Ag wire as a source on 17 nm GeO_x/SiO_x/Si(100) substrate at 800 °C in air for 30 minutes (b) SERS spectra of Creatinine of above sample at different points denoted by different colors showing the consistency of the substrate with uniform detection.

SERS spectrum of the creatinine molecules on nanosquares sample. Figure 8.7(b) revealing the consistency of the nanorods sample with almost uniform detection at different points of the sample. From this result we can conclude that these samples can be re-usable with proper cleaning.

8.4 Chapter Summary

SERS enhancement factors were calculated for endotaxial silver nanostructures with different shapes and different coverages using CV molecules. These enhancement factors were compared with the as-deposited case to understand the enhancement due to the presence of Ag endotaxial structures of different shapes and sizes. Different shape nanostructures synthesized using CVD method were used to study the effect of shape in SERS enhancement along with the effect of coverage of these nanostructures. Reusability of these samples were checked with CV, R6G and Creatinine molecules. Positive results were found for the samples that were properly treated with piranha followed by 1 minute HF etching. The endotaxial structures grown on Si substrates are found to be reliable and reusable SERS substrates to detect bio-molecules.

Chapter 9

Summary

A novel and a simple method has been developed to grow endotaxial silver nanostructures inside a silicon single crystal. A clever use of the interfacial layer, GeO_x deposited on Si (with native oxide) when annealed under air or low vacuum or even under argon flow around 800 °C, the silver vapors generated either through a PVD of silver films or through CVD process diffuse through to form endotaxial structures. The thesis lays out a detailed study on the formation of Ag-Si nanostructures under different thermal annealing conditions achieved by varying parameters such as, pressure, film thickness, substrate, presence or absence of GeO_x layer on the substrate, temperature *etc.* The emphasis is on the use of self-assembly techniques to synthesize well tuned Ag, Au, Ag-Si nanostructures and to study the reaction between them at different ambient conditions. Transmission electron microscopy (TEM), scanning TEM (STEM)-combined with HAADF, EDS, 3D tomography, scanning electron microscopy (SEM), focused ion beam (FIB), Rutherford backscattering spectrometry (RBS) and X-ray diffraction (XRD) experimental methods have been employed to understand the composition, true shape and growth kinetics. RBS method was used for the study of composition as a function of depth. Physical vapor deposition method and chemical vapor deposition method were employed to deposit thin films.

Formation of coherently embedded silver nanostructures in the silicon substrate depending up on the substrate orientation was studied on 2 nm Ag/ 17 nm $\text{GeO}_x/\text{SiO}_x/\text{Si}$ substrate with (100), (110) and (111) orientations. In the case of (100) substrate orientation, nanosquares/rectangles were observed, in the case of (110) substrate orientation, nanorods were found and for (111) substrate orientation nanotriangles were

formed according to their 4-fold, 2-fold and 3-fold substrate unit cell symmetries, respectively. The chemical analysis of the sample was studied in the case of 2 nm Ag/17 nm $\text{GeO}_x/\text{SiO}_x/\text{Si}(100)$ using STEM along with 3-dimensional (3D) information of these embedded nanostructures. A plausible mechanism was discussed and the role of GeO_x layer presence and the position of this layer in between Si and Ag were also studied. This explanation was extended to other two orientations to generalize the mechanism of these nanostructures formation.

In ambience dependent study, the influence of annealing ambience on the formation of the endotaxial nanostructures for 2 nm Ag/17 nm $\text{GeO}_x/\text{SiO}_x/\text{Si}(100)$ sample. The sample was annealed in different ambient conditions *viz* air, oxygen, low vacuum, argon and ultra high vacuum up to 800 °C for 30 minutes. Spherical nanostructures embedded in SiO_x layer was observed in the case of the sample which was annealed in oxygen ambience. For ultra high vacuum ambient annealed sample, spherical silver nanostructures were observed on top of polycrystalline germanium layer. Endotaxial nanostructures with square/rectangular shape were observed for remaining three cases like air, argon and low vacuum cases. Size, depth, height and the top oxide layer thicknesses were different for these endotaxial nanostructures. Oxygen partial pressure plays a key role in the formation of these endotaxial nanostructures *i.e.* very high or very low oxygen availability is not suitable for these endotaxial nanostructures growth.

Presence of silver on top of the substrate is not a critical condition to grow the endotaxial structures, because these structures was grown by CVD method where the supply silver was carried through silver vapors from a silver wire. The advantage of the CVD method is one can control the amount of material to deposit on the substrate by varying the deposition time and the deposition temperature and also the distance between the precursor and the substrate. The effect of deposition temperature and deposition time on size and coverage of these nanostructures was studied along with the effect of GeO_x presence. Presence of GeO_x is responsible for substrate symmetric silver endotaxial nanostructures shows a path to synthesize other metal nanostructures if one can pass those metal vapors on to the GeO_x coated substrate. With the increment in the deposition time increase of coverage was observed where

as with increase in the deposition temperatures yields much bigger and deeper nanostructures with compressive stress in the structures.

The use of these as-grown nanostructures by both PVD and CVD methods in SERS measurements found to be robust SERS substrates. These substrates are cost effective and easy to produce with less effort, makes them a potential candidate for SERS substrates. The control of the shape of the nanostructures by substrate orientation, results in shape control. The enhancement factors obtained using this substrate for crystal violet molecules is very encouraging. Detection of rhodamine 6G, creatinine proves that these substrates have a capability to detect not only CV molecules but also other dyes and bio-molecules which is positive fact in terms of wide applications of these samples as SERS substrates. Reusability of these samples reduces the labour in the preparation and saves the time and money.

Numerous interesting aspects of these endotaxial nanostructures formation can still be studied. For instance, it would be both fascinating and beneficial to study the generalization of this mechanism to other metals to form endotaxial nanostructures. The effect of silver thickness on these endotaxial structures and the effect of ambience in the other thicknesses of GeO_x layer and effect of replacing GeO_x with Ge. Controlling the inter diffusion of metal into silicon to form epitaxial structures instead of endotaxial structures.

In conclusion, the thesis emphasizes on three aspects that are relevant in the emerging area of nanoscience and nanotechnology: (i) growth of coherently embedded silver nanostructures in silicon substrate at ambient conditions with the help of GeO_x layer, (ii) systematic studies on the role of GeO_x layer and effect of annealing ambience on the shape and size of these nanostructures, and (iii) use of these nanostructures as potential SERS substrates to detect low concentration dye molecules.

Bibliography

- [1] M. S. Gudiksen, L. J. Lauhon, J. Wang, D. C. Smith and C. M. Lieber, *Nature* **415**, 617 (2002).
- [2] L. J. Lauhon, M. S. Gudikson, D. Wang and C. M. Lieber, *Nature* **420**, 57 (2002).
- [3] U. Srinivasan, M. A. Helmbrecht, R. S. Muller and R. T. Howe, *Optics Photonics News* **13**, 20 (2002).
- [4] K. F. Bohringer, *J. Micromech. Microeng.* **13**, S1-S10 (2003) .
- [5] C. N. R. Rao, P. J. Thomas and G. U. Kulkarni, *Nanocrystals: Synthesis, Properties and Applications* (Springer, 2007).
- [6] S. Link and M. A. El-Sayed, *J. Phys. Chem. B* **103**, 8410 (1999).
- [7] W. P. Halperin, *Rev. Mod. Phys.* **58**, 583 (1986).
- [8] S. J. Tans, A. R. M. Verschueren and C. Dekker, *Nature* **393**, 49 (1998).
- [9] M. Grundmann, F. Heinrichsdorff and N. N. Ledentsov, *Jpn. J. Appl. Phys* **39**, 2341 (2000).
- [10] G. A. Somorjai and Y. G. Borodko, *Catalysis Letter* **76**, 1 (2001)
- [11] N. K. Mal, M. Fujiwara and Y. Tanaka, *Nature* **421**, 350 (2003).
- [12] M. Taneike, F. Abe and K. Sawada, *Nature* **424**, 294 (2003).
- [13] H. Gleiter, *ActaMaterial* **48**, 1 (2000).
- [14] S. Nafis, Z. X. Tang and B. Dale, *J. Appl. Phys.* **64**, 5835 (1988).

- [15] A. E. Berkowitz, J. R. Mitchell and M. J. Carey, *Phys. Rev. Lett.* **68**, 3745 (1992).
- [16] A. S. Eldenstein, J. S. Murday and B. B. Rath, *Progress in Materials science* **42**, 5 (1997).
- [17] J. P. Borel, *Surf. Sci.* **106**, 1 (1981).
- [18] Y. D. Glinka, S. H. Lin, L. P. Hwang, Y. T. Chen and N. H. Tolk, *Phys. Rev. B* **64**, 085421 (2001).
- [19] C. Burda, X. Chen, R. Narayanan and M. A. El-Sayed, *Chem. Rev.* **105**, 1025 (2005).
- [20] S. Chen, R. S. Ingram, M. J. Hostetler, J. J. Pietron, R. W. Murray, T. G. Schaaff, J. T. Khoury, M. M. Alvarez and R. L. Whetten, *Science* **280**, 2098 (1998).
- [21] N. L. Swanson and B. D. Billard, *Nanotechnology* **14**, 353 (2003).
- [22] H. Xu, E. J. Bjerneld, M. Kall and L. Borjesson, *Phys. Rev. Lett.* **83**, 4357 (1999).
- [23] P. Alvisato *Science* **271**, 933 (1996).
- [24] C. J. Murphy, T. K. Sau, A. M. Gole, C. J. Orendorff, J. Gao, L. Gou, S. E. Hunyadi and T. Li, *J. Phys. Chem. B* **109**, 13857 (2005).
- [25] E. Piscopiello, L. Tapfer, M. V. Antisari, P. Paiano and P. Prete, *Phys. Rev. B* **78**, 035305 (2008).
- [26] M. G. Warner and J. E. Hutchison, *Nature Materials* **2**, 272 (2003).
- [27] Y. Xiao, F. Patolsky, E. Katz, J. F. Hainfeld and I. Willner, *Science* **299**, 1877 (2003).
- [28] A. T. Bell, *Science* **299**, 1688 (2003).
- [29] Y. Li and G. Shi, *J. Phys. Chem. B*, **109**, 23787 (2005).
- [30] L. Qian and X. Yang, *J. Phys. Chem. B*, **110**, 16672 (2005).
- [31] Y. Li, G. Lu and G. Shi, *J. Phys. Chem. B*, **110**, 24585 (2006).

- [32] Y. He, X. Yu and B. Yang, *Mater. Chem. Phys.* **99**, 295 (2006).
- [33] H. H. Park, X. Zhang, Y. J. Choi, H. H. Park and R. H. Hill, *J. Nanomaterials* **2011**, 265287 (2011).
- [34] H. Adhikari, A. F. Marshall, C. E. D. Chidsey and P. C. McIntyre, *Nano Lett.* **6**, 318(2006).
- [35] R. J. Chimentao, I. Kirm, F. Median, X. Rodriguez, Y. Cesteros, P. Salagre and J. E. Sueiras, *Chem. Comm.* **2004**, 846 (2004).
- [36] Y. Sun, B. Gates, B. Mayers and Y. Xia, *Nano Lett.* **2**, 165 (2002).
- [37] P. B. Johnson, R. W. Christy *Phys. Rev. B* **6**, 4370 (1972)
- [38] V.P. Darchev, U. K. Chettiar, A. V. Kildishev, H. K. Yuan, W. Cai and V. M. Shalev, *Optics Exp.* **16**, 1186 (2008).
- [39] B. J. Wiley, S. H. Im, Z. Y. Li, J. McLellan, A. Siekkinen and Y. Xia, *J. Phys. Chem. B* **110**, 15666 (2006).
- [40] S. Pillai, K. R. Catchpole, T. Trupke and M. A. Green, *J. Appl. Phys.* **101**, 093105 (2007).
- [41] P. Spinelli, M. Hebbink, R. De Waele, L. Black, F. Lenzmann and A. Polman, *Nano Lett.* **11**, 1760 (2011).
- [42] E. Thouti, N. Chander, V. Datta and V. K. Komarala, *J. Optics* **15**, 35005 (2013).
- [43] H. R. Stuart and D. G. Hall, *Appl. phys. Lett.* **73**, 3815 (1998).
- [44] S. K. Kim, C. H. Chao, B. H. Kim, Y. S. Choi, S. J. Park, K. Lee and S. Im, *Appl. Phys. Lett.* **94**, 183108 (2009).
- [45] K. R. Catchpole and S. Pillai, *J. Lumin* **121**, 315 (2006).
- [46] T. Watanabe and B. Pettinger, *Chem. Phys. Lett* **89**, 501 (1982).
- [47] D. W. Brett, *Ostonomy Wound Manage* **52**, 34 (2006).
- [48] A. B. Lansdown, *Prof. Nurse.* **20**, 41-3 (2005).

- [49] S. Pal, Y. K. Tak and J. M. Song, *Appl. Environ. Microbiol.* **73**, 1712 (2007).
- [50] Y. J. Lu, J. Kim, H. Y. Chen, C. Wu, N Dabidian et. al, *Science* **337**, 450 (2012).
- [51] J. C. Frank and J. H. van der Merwe, *Proc. Roy. Soc. London* **A198**, 205 (1949).
- [52] M. Volmer and A. Weber, *J. Phys. Chem* **119**, 277 (1926).
- [53] I. N. Stranski and Von L. Krastanov, *Akad. Lit. Mainz Math -Natur. Kl. Iib* **146**, 797 (1939).
- [54] J. H. van der Merwe, *CRC. Crit. Rev. Solid State Mattr. Sci.* **17**, 187 (1991).
- [55] I. Bonev, *Acta. Cryst. A* **28**, 508 (1972).
- [56] S. Mantl, *J. Phys. D: Appl. Phys.* **31**, 1 (1998).
- [57] A. Y. Cho and J. R. Arthur, *Prog. in Solid State Chem.* **10**, 157 (1975).
- [58] M. Leskel and M. Ritala, *Thin Solid Films* **409**, 138 (2002).
- [59] P. A. Bennett, Z. He, D. J. Smith and F. M. Ross, *Thin Solid Films* **519**, 8434 (2011).
- [60] P. A. Bennett, B. Ashcroft, Z. He and R. M. Tromp, *J. Vac. Sci. Tech. B* **20**, 2500 (2002).
- [61] J. C. Mahatao, D. Das, R. R. Juluri, R. Batabyal, A. Roy, P. V. Satyam and B. N. Dev, *Appl. Phys. Lett.* **100**, 263117 (2012).
- [62] K. L. Kavanagh, M. C. Reuter and R. M. Tromp, *J. Cryst. Growth* **173**, 393 (1997).
- [63] J. F. Lin, J. P. Bird, Z. He, P. A. Bennett and D. J. Smith, *Appl. Phys. Lett.* **85**, 281 (2004).
- [64] D. Sakellari, N. Frangis and E. K. Polychroniadis, *Phys. E: Low dimensional syst. and Nanostructures* **42**, 1777 (2010)
- [65] T. George and R. W. Fathauer, *Appl. Phys. Lett.* **59**, 3249 (1991).

- [66] T. P. Hogan, A. Downey, J. Short, J. D'Angelo, C. I. Wu, E. Quarez, J. Andoulakis, P.F. P. Poudeu, J. R. Sootsman, D. Y. Chung, M. G. Kanatzidis, S. D. Mahanti, E. J. Timm, H. Schock, F. Ren, J. Johnson and E. D. case, *J. Electron Mater.* **36**, 704 (2002).
- [67] D. Dijkkamp, E. J. van Leonen, A. J. Hoeven and J. Dieleman, *J. Vac. Sci. and Tech. A* **8**, 218 (1990).
- [68] B. R. Weinberger, G. G. Peterson, T. C. Eschrich and H. A. Krasinski, *J. Appl. Phys.* **60**, 3232 (1986).
- [69] A. Reisman, S. T. Edwards and P. L. Smith, *J. Electrochem. Soc: Solid-state Sci. Tech.* **135**, 2849 (1988).
- [70] G. J. Russel and D. Haneman, *J. Electrochem. Soc: Solid-state Sci. Tech.* **114**, 398 (1967).
- [71] M. Futagami and M. Hamazaki *Jpn. J. Appl. Phys.* **21**, 1782 (1982).
- [72] M. A. Hooper, R. A. Clarke and L. Young, *Surf. Sci.* **56**, 472 (1976).
- [73] Krishna Seshan (Ed.), *Handbook of thin-film deposition processes and techniques* (Noyes Publications, New York, 2002). Second Ed.
- [74] R. Glang, "Vacuum evaporation" Ch I in *Thin film technology* (McGraw-Hill Book Co., 1970).
- [75] Donald M. Mattox and William Andrew, Vacuum Evaporation and Vacuum Deposition Ch V in *Hand book of PVD processing* (Noyes Publications, New York, 1998).
- [76] M. Ohring *Materials Science of Thin films. Deposition and Structure* (Academic Press, 2002).
- [77] A. C. Jones and M. L. Hitchman, *Chemical Vapor Deposition: Precursors, Processe and Applications* (RSC Publishing, Cambridge 2009).
- [78] D. B. Williams and C. Barry Carter, *Transmission Electron Microscopy* Vol. I-IV (Plenum Press, New York, 1996).

- [79] John C. H. Spence, *High-resolution Electron Microscopy* (Oxford University Press 2003), 3rd Ed.
- [80] Brent Fultz and James Howe, *Transmission Electron Microscopy and Diffractometry of Materials* (Springer, 2005), 2nd Ed.
- [81] M. Knoll and E. Ruska, *Z. Physik.* **78**, 318 (1932).
- [82] J. M. Cowley, A.F. Moodie, *Acta Crystallogr.* **10**, 609 (1957).
- [83] J. Ackermann, *Manual for the SUPRA (VP) and ULTRA Scanning Electron Microscopes. Smart SEM V. 05.00. 2005. Carl Zeiss SMT Ltd.*
- [84] H. Seiler, *J. Appl. Phys.* **54**, R1 (1983).
- [85] J. Goldstein, et al., *Scanning Electron Microscopy and X-ray Microanalysis* (Kluwer Academic/Plenum Publishers, 2003), third edn.
- [86] Robert J. Keyse, Anthony J. Garrett-Reed, Peter J. Goodhew and Gordon W. Lorimer, *Introduction to scanning transmission electron microscopy* (Bios Scientific Publishers, 1998).
- [87] Peter W. Hawkes, John C. H. Spence, *Science of microscopy*, vol **1**, (Springer-2008)
- [88] J. Liu, *J. Ele. Microscopy*, **54**, 251 (2005).
- [89] P. Hartel, H. Rose and C. Dinges, *Ultramicroscopy* **63**, 93 (1996).
- [90] C. Kubel, A. Voigt, R. Schoenmakers, M. Otten, D. Su, T. C. Lee, A. Carlsson and J. Bradley, *Microscopy and Microanal.* **11**, 378 (2005).
- [91] J. Frank *Electron Tomography: Three-dimesnional imaging with the Transmission Electron Microscope*(Plenum Press, New York)
- [92] E. Rutherford, *Phil. Mag.* **21**, 669 (1911).
- [93] W. K. Chu, J. W. Mayer, M. A. Nicolet, *Backscattering spectrometry* (Academic Press, New York, 1978).
- [94] K. Sekhar, G. Kuri, P. V. Satyam, B. Sundaravel, D. P. Mahapatra and B. N. Dev, *Indian J. Phys.* **684**, 1 (1994).

- [95] M. Mayer, *Proc. of the 15th International Conference on the Application of Accelerators in Research and Industry*, J. L. Duggan and I.L. Morgan (eds.), American Institute of Physics Conference Proceedings, Denton, USA, **475**, 541 (1999).
- [96] C. V. Raman and K. S. Krishna, *Nature* **121**, 501 (1928).
- [97] R. L. Mc Creery, *Raman Spectroscopy for Chemical Analysis* (John Wiley & Sons, New York, 2000)
- [98] M. Fleischman, P. J. Hendra and A. J. McQuillan, *Chem. Phys. Lett.* **26**, 163 (1974).
- [99] D. L. Jeanmaire and R. P. Van Duyne, *J. Electroanal. Chem.* **84**, 1 (1977).
- [100] S. Nie and S. R. Emory, *Science* **275**, 1102 (1997).
- [101] J. Kneipp, H. Kneipp and K. Kneipp, *Proc. Natl. Aca. Sci., USA* **103**, 17149 (2006).
- [102] M. Moskovits *Surface-Enhanced Raman Spectroscopy: a Brief Perspective* (Springer, 2006, pp:1-18)
- [103] A. Campion and P. Kambhampati *Chem. Soc. reviews* **27**, 241(1998).
- [104] J. R. Lombardi, R. L. Brike, T. Lu and J. Xu *The J. Chem. Phys.* **84**, 4174 (1986).
- [105] J. R. Lombardi and R. L. Brike *J. Phys. Chem. C* **112**, 5605 (2008).
- [106] W. L. Barnes, A. Dereux, T. W. Ebbesen, *Nature* **424**, 824 (2003).
- [107] X. Hu, C. T. Chan *Appl. phys. lett.* **85**, 1520 (2004).
- [108] Y. T. Pang, G. W. Meng, Q. Fang and L. D. Zhang *Nanotechnology***14**, 20 (2003).
- [109] B. Sharma, R. R. Frontiera, A. I. Henry, E. Ringe and R.P. Van Duyne *Mat. Today* **15**, 16 (2012).
- [110] B. Wiley, Y. Sun and Y. Xia *Acc. Chem. Res.* **40** 1067 (2007).

- [111] D. B. Williams, C. B. Carter *Transmission Electron Microscopy: A Textbook for Materials Science* (Springer, 1996).
- [112] R. R. Juluri, A. Rath, A. Ghosh and P. V. Satyam, *J. Phys. Chem. C* **117**, 13245 (2013).
- [113] Y. Oniki, H. Koumo, Y. Iwazaki and T. Ueno *J. Appl. Phys.* **107**, 124113-1 (2010).
- [114] Y. Kamata, A. Takashima and T. Tsutomu *Mat. Res. Soc. Symp. Proc.* **1155**, C02 (2009).
- [115] R. B. Bernstein and D. Cubicciotti *J. Am. Chem. Soc.* **73**, 4112 (1951).
- [116] S. K. Wang, H. G. Liu and A. Toriumi *Appl. Phys. Lett.* **101**, 061907-1 (2012).
- [117] S. J. Yun, S. C. Lee, B. Kim and S. W. Kang *J. Vac. Sci. Technol. B* **12**, 1167 (1994).
- [118] T. C. Nason, G. R. Yang, K. H., Park and T. M. Lu *J. Appl. Phys.* **70**, 1392 (1991).
- [119] F. Rollert, N. A. Stolwijk and H. Mehrer *J. phys. D: Appl. Phys.* **20**, 1148 (1987).
- [120] H. Xin, J. M. Zhang, X.-M., Wei and K. W. Xu *Surf. and Inter. Anal.* **37**, 608 (2005).
- [121] G. Wulff *Zeitschrift fr Krystallographie und Mineralogie* **34**, 449 (1901).
- [122] M. V. Laue, *Zeitschrift fr Kristallographie* **105**, 124 (1943).
- [123] J. D. Mc Brayer, R. M. Swanson, T. W. Sigmon and J. Bravman *Appl. Phys. Lett.* **43**, 653 (1983).
- [124] S. Link, and M. A. El-Sayed *Int. Rev. in Phy. Chem.* **19** 409 (2000).
- [125] H. Hvel, S. Fritz, A. Hilger, U. Kreibig, and M. Vollmer *Phys. Rev. B* **48**, 18178 (1993).
- [126] A. Hilger, M. Tenfelde and U. Kreibig *Appl. Phys. B* **73**, 361 (2001).

- [127] B. N. J. Persson *Phys. Rev. B* **44**, 3277 (1991).
- [128] B. N. J. Persson, *Surf. Sci.* **281**, 153 (1993).
- [129] K. Charl, F. Frank and W. Schulze Ber. Bunsenges. *Phys. Chem.* **88**, 350 (1984).
- [130] A. V. Pinchuk, U. Kreibig, and A. Hilger, *Surf. Sci.* **557**, 269 (2004).
- [131] P. Spinelli, A. Polman *Optics Exp.* **20**, A641 (2012).
- [132] S. Surnev *Surf. Sci.* **282**, 10 (1993).
- [133] SRIM software: <http://www.srim.org/>
- [134] T. Ogino, H. Hibino and K. Prabhakaran, *J. Vac. Sci. Tech. B* **14**, 4134 (1996).
- [135] R. R. Juluri et. al., *Nature Sci. Rep.* **4**, 4633 (2014).
- [136] H. J. Freund, *Surf. Sci.* **500**, 271 (2002).
- [137] S. W. Boettcher, N. C. Strandwitz, M. Schierhorn, N. Lock, M. C. Lonergan, and G. D. Stucky, *Nat. Mater.* **6**, 592 (2007).
- [138] I. Berbezier, A. Ronda, A. Portavoce and N. Motta, *Appl. Phys. Lett.* **83**, 4833 (2003).
- [139] D. J. Eaglesham, F. C. Unterwald and D. C. Jacobson, *Phys. Rev. Lett.* **70**, 966 (1993).
- [140] http://www.engineeringtoolbox.com/linear-expansion-coefficients-d_95.html
- [141] Y. N. Wen and J. M. Zhang, *Solid State Comm.* **144**, 163 (2007).
- [142] Y. Y. Yu, S. S. Chang, C. L. Lee and C. R. C. Wang, *J. Phys. Chem. B* **101**, 1588 (1997).
- [143] N. R. Jana, L. Gearheart and C. J. Murphy, *J. Chem. Comm.* **2001**, 617 (2001).
- [144] M. Millarld, S. Giorgio and M. P. Pileni, *J. Phys. Chem. B* **107**, 2466 (2003).
- [145] H. A. Atwater and A. Ploman, *Nature Mat.* **9**, 205 (2010).
- [146] H. R. Stuart and D. G. Hall, *Phys. Rev. Lett.* **80**, 5663 (1998).

- [147] Y. Yang, S. Matsubara, L. Xiong, T. Hayakawa and M. Nogami, *J. Phys. Chem. C* **111**, 9095 (2007).
- [148] L. Han, P. Wang, C. Zhu, Y. Zhai and S. Dong, *Nanoscale* **3**, 2931 (2011).
- [149] M. J. Rosemary and T. Pradeep, *J. Colloid and Inter. Sci.* **268**,81 (2003).
- [150] W. Lu, F. Liao, Y. Luo, G. Chang and X. Sun, *Electrochimica Acta* **56**, 2295 (2011).
- [151] P. K. Khanna, N. Singh, S. Charan and A. K. Viswanath, *Mat. Chem. Phys.* **92**, 214 (2005).
- [152] A. Rath, J. K. Dash, R. R. Juluri, A. Rosenauer and P. V. Satyam, *J. Phys. D: Appl. Phys.* **44**, 115301 (2011).
- [153] A. Rath, J. K. Dash, R. R. Juluri, A. Rosenauer, m. Schoewalter and P. V. Satyam, *J. Appl. Phys.* **111**, 064322 (2012).
- [154] G. Rovida, F. Pratesi, M. Maglietta and E. Ferroni, *J. Vac. Sci. Tech.* **9**, 796 (1972).
- [155] B. R. Ford and J. Pritchard, *Chem. Comm.* **1968**, 362 (1968).
- [156] M. A. Hopper, R. A. Clarke and L. Young *Sur. Sci.* **56**, 472 (1976).
- [157] K. Prabhakaran, F. Maeda, Y. Watanabe and T. Ogino, *Appl. Phys. Lett.* **76**, 2244 (2000).
- [158] D. K. Goswami, K. Bhattacharjee, B. Satpati, S. Roy, G. Kuri, P. V. Styam and B. N. Dev, *Appl. Surf. Sci.* **253**, 9142 (2007).
- [159] J. Kneipp, H. Kneipp, B. Wittig, K. Kneipp *Nanomed.: Nanotech. Bio. Med.* **6**, 214 (2010).
- [160] P. L. Stiles, J. A. Dieringer, N. C. Shah, R. P. Van Duyne *Annu. Rev. Anal. Chem.* **1**, 601 (2008).
- [161] E. C. Le Ru, E. Blackie, M. Meyer and P. G. Etchegoin, *J. Phys. Chem. C* **111**, 13794 (2007).
- [162] X. M. Qian and S.M. Nie *Chem. Soc. Rev.* **37**, 912 (2008).

- [163] A. Otto *J. Raman Spectroscopy* **33**, 593 (2002).
- [164] J. P. Camaden, J. A. Dieringer, Y. Wang, D.J. Masiello, Marks. et al. *J. Am. Chem. Soc.* **130**, 12616 (2008).
- [165] A. S. Stender, K. Marchuk, C. Liu, S. Sander, Meyer. et al., *Chem. Rev.* **113**, 2469 (2013).
- [166] S. Schultz, D. Smith, J. J. Mock and D. A. Schultz *Proc. Natl. Acad. Sci., USA* **97**, 996 (2000).
- [167] J. N. Anker, W.P. Hall, O. Lyandres, N. C. Shah, Zhao. et al. *Nat. Mater.* **7**, 442 (2008).
- [168] K. L. Wustholz, A. I. Henry, J. M. McMahon, R. G. Freeman, N. Valley et al. *J Am Chem. Soc.* **132**, 10903 (2010).
- [169] P. Negri and R. A. Dluhy *J. Biophotonics* **6**, 20 (2013).
- [170] M. Naya, T. Tani, Y. Tomaru and J. Li, N. Murakami, *Proc SPIE* **7032**, 70321Q/1 (2008).
- [171] J. Fang, S. Liu and Z. Li *Biomaterials* **32**, 4877 (2011).
- [172] K. B. Biggs, J. P., Camden, J. F., Anker and R. P. Van Duyne *J. Phys. Chem. A* **113**, 4581 (2009).
- [173] N. Leopold and B. Lendl *J. Phys. Chem. B* **107**, 5723 (2003).
- [174] K. Kneipp, Y. Wang, H. Kneipp, L. T. Perelman, I. Itzkan et al. *Phys. Rev. Lett.* **78**, 1667 (1997).
- [175] W. J. Cho, Y. Kim and J. K. Kim, *ACS Nano* **6**, 249 (2012).
- [176] A. Kudelski, *Chem. Phys. Lett.* **414**, 271 (2005).
- [177] P. Hildebrandt and M. Stockburger, *J. Phys. Chem* **88**, 5935 (1984).
- [178] T. M. Cotton, S. G. Schultz and R. P. Van Duyne, *J. Am. Chem. Soc.* **102**, 7960 (1980)
- [179] T. M. Cotton, R. Timkovich and M. S. Cork, *FEBS Lett.* **133** 39 (1981).

- [180] T. M. Cotton, S. G. Schultz and R. P. Van Duyne, *J. Am. Chem. Soc.* **104**, 6528 (1982)
- [181] T. M. Cotton and R. P. Van Duyne, *FEBS Lett.* **147**, 81 (1982).
- [182] M. Itabashi, K. Kato and K. Itoh, *Chem. Phys. Lett.* **97**, 528 (1983).